POLITECNICO DI TORINO

Corso di Laurea Magistrale in Ingegneria Biomedica

Tesi di Laurea Magistrale

Heartbeat Sequence Extraction from Cerebral NIRS Measures

A NIRS Study of the Cerebrovascular Hemodynamics on Patients Suffering from Atrial Fibrillation

Relatori
Prof. Luca Ridolfi
Prof.ssa Stefania Scarsoglio

Correlatori
Prof. Matteo Anselmino
Dott.ssa Daniela Canova
Dott. Andrea Saglietto

Candidato
Ivan Ferrandino

A.A. 2018-2019

Acknowledgements

Contents

Introduction

In the Western countries atrial fibrillation (AF) is one of the most common forms of arrhythmia, especially involving patients who are ≥ 60 of age, and it is often associated with co-occurring chronic conditions. AF is a supraventricular tachyarrhythmia concerning the atrial chambers which stop contracting effectively, leading to a cascade of side effects on the whole cardiovascular system. Its triggering and sustaining mechanisms are various and complex, making this condition very difficult to manage for clinicians. AF can be investigated through an electrocardiogram (ECG) and trhough additional techniques such as the transesophageal echocardiography (TEE) which is specifically used to detect the presence of thrombi due to this condition. Patients affected by AF are generally pharmacologically treated and undergo clinical cardioversions and catheter ablation procedures. Beside being related to high levels of morbidity and risk of mortality, it is classified in different forms and it can be either asymptomatic or strongly symptomatic, involving symptoms such as fatigue, palpitations and syncope. Stroke and heart failure particularly stand out among the main consequences of AF [1].

Moreover, AF has also been linked to the development of dementia [2][3][4], meaning that it has repercussions on the cognitive functions as well. In this context, a reliable method to investigate the impact of the anomalous atrial contraction on the cerebral hemodynamics is needed.

Previous works by Scarsoglio et al. [5][6][7] showed the impact of AF on hemodynamic components, such as pressure and flow rate, at different levels of a cerebral cardiovascular structure model. In this work, real data coming from real subjects have been used with the same purpose. The real data chosen for this study consist in near infrared spectroscopy (NIRS) signals detected on six healthy subjects and six patients affected by AF and undergoing a cardioversion procedure. The main focus of this work consists in the extraction of the heartbeat information contained in the NIRS signals reflecting the hemodynamic of the cerebrovascular system at a cortical level. This was possible thanks to the particular characteristics of this technique, which is absolutely non-invasive and it is nevertheless able to reach the first layers of the cerebral cortex, detecting the presence of oxygenated and deoxygenated hemoglobin. For this reason, NIRS has always been mainly used in the cerebral oxymetry field. However, in this work NIRS signals have been sampled at a higher rate than usual (20 Hz) making this study different from other studies, which also focused on patients affected by arrhythmias or AF but mainly using NIRS at low sampling frequencies, hence excluding the potential beat-to-beat information that could be extracted from these signals [8][9][10]. The following step, which is not taken in this work, may consist in a study of the extracted heartbeat in terms of complex networks as

it has been done in [5] with the modeled signals of hemodynamic pressure and flow rate. In fact, complex networks proved to be a valuable tool able to expand the understanding of a complex condition such as the effects of AF on the cerebral circulation, as already demonstrated in [5].

The work presented here is structured as follows: after a first introduction of the NIRS scenario, from the birth of the technique to its last main uses, showing both its relevant potentials and physical drawbacks, the measurements and the methods adopted in the carried out experiments will be described, a preliminary signal processing involving the detected NIRS signals will be shown, followed by a statistical analysis on the collected signals dataset and lastly describing the main processing leading to the heartbeat information extraction accompanied by all the relevant obtained results.

All the experiments carried out on patients suffering from AF could be possible thanks to the collaboration with the cardiology day-hospital unit of *Città della Salute e della Scienza* hospital of Turin and particularly thanks to the precious contribution of the physiological and medical counterpart of this work including Prof. Matteo Anselmino, Dr. Daniela Canova and Dr. Andrea Saglietto.

Chapter 1

Near Infrared Spectroscopy (NIRS)

Near infrared (NIR) energy extends in the wavelength interval between 780-2500 nm and it was firstly discovered by Fredrick W. Herschel in the XIX century. Herschel used a prism to project a rainbow on a bench and then he measured the relative heating effect of different parts of it. Moving from the blue to the red, he found that the heating effect increased and it kept increasing even when he came to the end of the spectrum, indicating the presence of remarkable energy even outside the visible spectrum. In fact, he measured the maximum heating effect in the black area beyond the red end of the visible spectrum, demonstrating that the energy of the sun is not limited to what can be seen [11].

Beginning to be used in the 1950's as a simple add-on unit in spectrometers which also adopted other wavelengths, NIRS finally appeared as an industrially acknowledged technique. Originally applied in chemical analysis and astronomy, it became an important medical tool only after 1977, thanks to Frans F. Jobsis' experiment of monitoring animals' brain oxygenation by using light transmission through their tissues [12]. This technique basically consists in placing two probes (an emitter of the NIR radiation and a detector) on the investigated volume of tissue and in detecting the intensity of the traversing radiation, which is then converted into an electric signal by the detector.

Since visible light (400-700 nm) can penetrate biological tissues only up to approximately 1 cm because of the strong scattering effect determined by the tissue constituents, near infrared light represents a suitable alternative to illuminate deeper structures like the cerebral cortex, since photons can penetrate further in this range of wavelength [13].

1.1 Physical Principle

The human brain represents a tight connection between a functional component (its cells and their vascularization) and a logistic component (its cellular metabolism). In this neurovascular connection there must be a balance between a sensorial component (responsible for the detection of external inputs) and an executive component (responsible for the generation of the outputs in response to the inputs). While the neuronal component functioning is generally measured using electroencephalographic (EEG) signals (i.e. it is approached

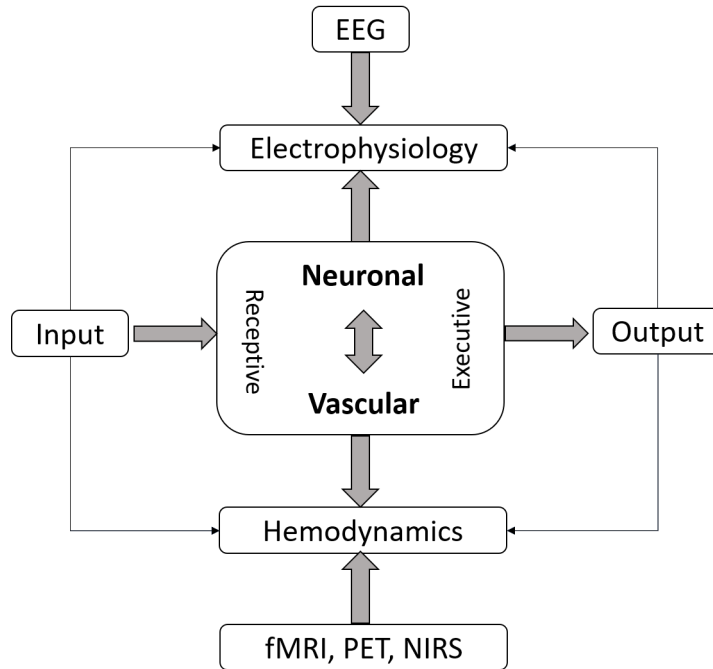by electrophysiology), the vascular component is related to hemodynamics, as recapped by figure 1.1.1.

Figure 1.1.1: Cerebral functioning components and related measurement techniques

Moreover, the measures related to the vascular component are not meant to be simply flow measurements, but they are measurements of various changes occurring in a certain cerebral area and required by the cellular metabolism of that area. In this scenario, although other techniques to evaluate the hemodynamics of the cerebral vascular system are available (such as fMRI and PET), NIRS might be favored because it allows to have a higher time resolution, which is more coherent with the resolution provided by EEG signals, and it is less invasive. This is accomplished by NIRS not by measuring directly cerebral blood flow (CBF) quantities, but by measuring quantities which are *related* to the blood flow.

The main physical features making NIRS a popular and working technique are:

1. *non-invasiveness*;

2. use of *non-ionizing radiations*;

3. *transparency of human tissues* in the near infrared wavelength interval;

4. *the absorption of the radiation depends on the tissue* and its instantaneous characteristics.

According to these features, NIRS is used to detect the presence of hemoglobin in the blood, which can absorb the radiation and consequently allows to determine how it

is treated by the tissues. By quantifying the presence of oxyhemoglobin (O$_2$Hb) and deoxyhemoglobin (HHb), it is then possible to evaluate the level of brain perfusion in some areas of the cerebrovascular system.

NIRS is therefore based on the simple physical principle consisting in the absorption of near infrared light by some substances having different absorption spectra (figure 1.1.2). This phenomenon is quantified by the Lambert-Beer law (LBL), proposed by August Beer and Heinrich Lambert in the XIX century [12], which relates the absorption of light to the properties of the traversed material. According to this law, the absorbance A of the emitted radiation through a solution of a single chromophore is calculated as

$$A = \log\left(\frac{I_0}{I}\right) = \alpha \cdot c \cdot d = \mu_a \cdot d \tag{1.1.1}$$

where I_0 is the intensity of the incident light, I is the intensity of the transmitted light, α is the extinction coefficient for the solute at the given wavelength, c is the chromophore concentration, d is the pathlength followed by the light through the solution and the term $\mu_a = \alpha \cdot c$ represents the linear attenuation coefficient of the medium (figure 1.1.3)[14].
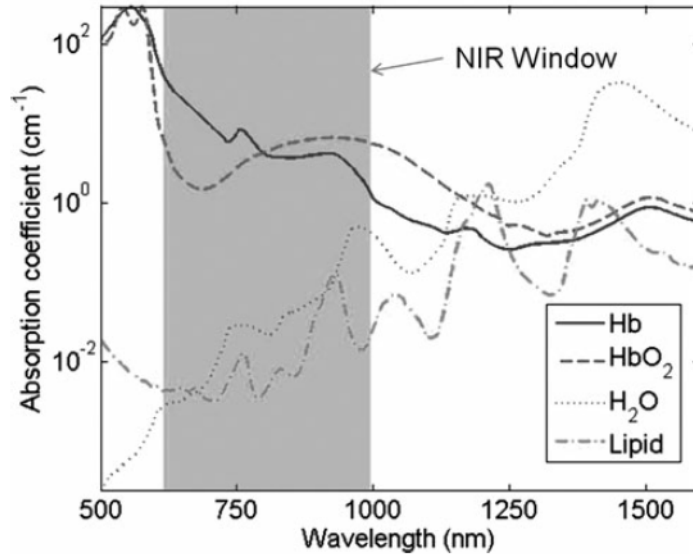

Figure 1.1.2: Absorption coefficients of O$_2$Hb, HHb and other biological substances
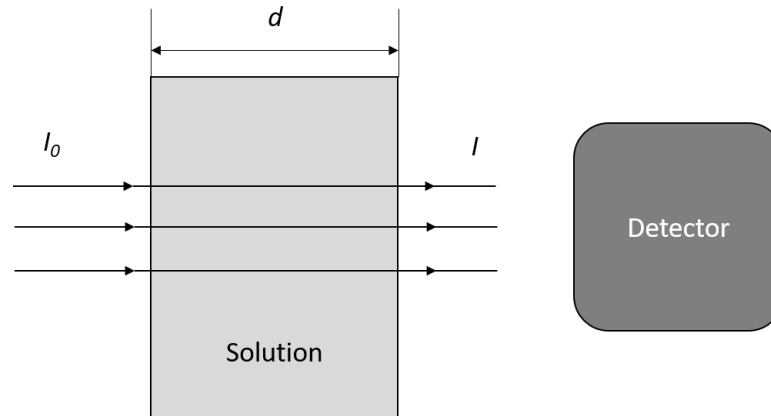
Figure 1.1.3: Scheme of the physical principle described by the Lambert-Beer law

Therefore, it is possible to quantify the concentration c of multiple chromophores in a solution by adapting the equation (1.1.1) to each of them and solving the resulting system.

With reference to NIRS in medical applications, the two solutes of interest are O_2Hb and HHb, hence it is possible to determine the type of hemoglobin concentration to measure simply by using two different incident wavelengths according to their absorption spectra.

It is also noteworthy that, as 70-80% of the blood in the brain is in the venous compartment, NIRS mainly offers iformation about venous blood [15][13].

1.2   Physical Issues

As indicated by Wahr et al. [12], the application of the Lambert-Beer law to quantify the concentration of multiple substances through NIRS has the following requirements.

1. Every substance concentration must be measured using a separate wavelength.

2. The light intensity change detected must be large enough.

3. The pathlength of light must be measured precisely.

Addressing the wavelengths requirement, even if there are other chromophores in the tissues which are able to alter their absorption of light due to their oxygenation state, they have basically no absorbance in the NIR range, where hemoglobin instead represents the strongest absorber [12]. As a result, no relevant issue is faced in meeting this requirement.

The real problems concern the intensity of measurable light and the determination of the pathlength. For reflected light, the pathlenght is linearly related to the space between the source and the detector so that many NIRS instruments focus on the measurement of *reflected* light instead of *transmitted* light. As a result, emitter and receiver are usually placed some centimeters distant from each other on the patients' head affecting the volume of investigated tissue and the depth of light penetration. In addition, the pathlength depends on the optical characteristics of the tissue, the measurement geometry and the concentration of the chromophore. In fact, for more concentrated solutions, the likelihood

10

of photons to be absorbed will be higher than in less concentrated solutions, leading to a shorter pathlength for the detected photons. The issue of the pathlength measurement has been addressed by multiplying the source-detector distance term d by a corrective term called differential pathlength factor (DPF), which depends on the optical characteristics of the tissue. However, some problems concern the DPF term since its value is affected by a certain intersubject variability and since the light penetrating the head of a subject goes through different kinds of tissue and substances (i.e. skin, bone, cerebrospinal liquid etc.) with different optical characteristics contributing to the pathlength value (and to the DPF) in various ways. This means that at least the contribution to pathlength given by each traversed tissue should be known. For instance, using some mathematical models it has been estimated that the contribution of cerebral tissue to the total pathlength followed by light through an adult head is about 20-40% [12].

Additionally, one of the main drawbacks of NIRS is light scattering (figure 1.2.1), affecting the intensity of measurable light. When the emitted photons reach the skull of the subject, they are partially absorbed, partially transmitted and partially deflected randomly because of the different refractive indexes of the cranial structures and tissues they meet on their way. It has been estimated by computer modeling that in a typical volume of tissue interrogated by NIRS about 30% is made of brain and the rest 70% is scalp and skull [13]. Therefore, the contribution to the scattering effect given by the extracerebral tissues is relevant in NIRS measurements. Because of scattering, some photons are lost and some others lose energy but are detected anyway, thus affecting the quality of the measure.
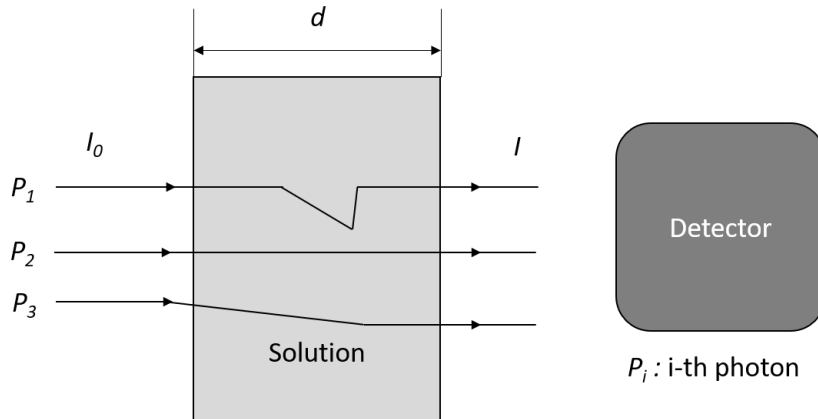

Figure 1.2.1: Scheme of scattering of photons traversing a chromophore solution

A loss of light intensity of approximately one order of magnitude per centimeter of traversed tissue is considered to occur because of both scattering and absorption [12]. Consequently, neglecting the scattering effect could result in an overestimation of the chromophore concentration.

Usually photons penetrating the brain travel along an approximate banana-shaped path (figure 1.2.2)[14] with its middle portion reaching the deepest side and the depth of the followed path depending on the distance between source and detector. In fact, increasing the source-detector separation can enhance the reached depth but it affects the spatial resolution because of a more spread distribution of photons [16].
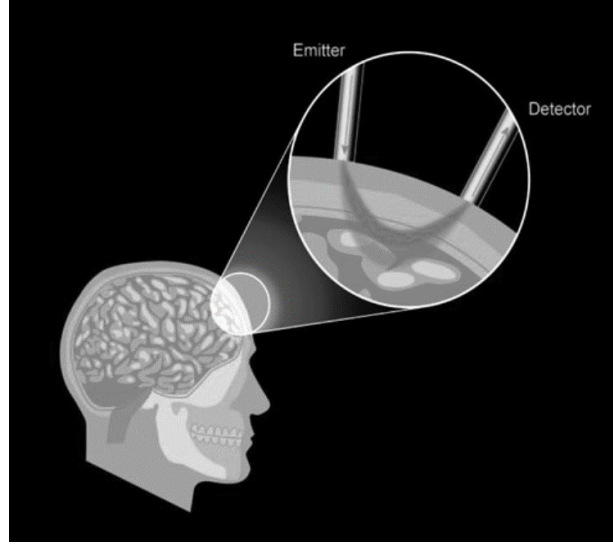
Figure 1.2.2: Banana-shaped path followed by photons between emitter and detector

However, although NIR light can penetrate human tissues up to a depth of several centimeters, the scattering factor is about ten times more probable than absorption. Besides, apart from O_2Hb and HHb, other substancies like water, fat and proteins contribute to absorption [15].

Since only a fraction of the scattered radiation is detected, the total light loss is unknown, meaning that the absolute value of the chromophores concentration is very difficult to quantify.

It must be noticed that the original Lambert-Beer law (equation 1.1.1) assumes a complete transmission of light through the medium without accounting the scattering effect [14]. In addition, the equation (1.1.1) lacks the DPF coefficient which accounts the correct pathlength quantification issue. For this reason, a modified version of the original Lambert-Beer law (MLBL) was introduced [17].

$$A = \alpha \cdot c \cdot d \cdot B + G \qquad (1.2.1)$$

where B and G are new corrective terms.

B represents the DPF, which is the above-mentioned non-dimensional coefficient adopted to consider the increased absorption of light due to the longer path followed by the scattered photons: it determines the average elongated path followed by a photon. In other words, it describes the *actual* distance traveled by light and it is wavelength dependent [13]. The product $B \cdot d$ is called differential pathlength. The term *differential* is related to the fact that B allows a modification of the equation (1.1.1) to quantify the *differences* in absorber concentration c derived from the *differences* in absorbance A [12]. B is estimated through proper mathematical models of the geometry of various body districts and therefore it can be found in literature.

G is a non-dimensional term with the aim of balancing the effect of the lost scattered photons. It considers the kind of tissue, its geometry and other parameters. G depends on the position of the probes on the head of the subject and on the specific conformation

of the skull of the individual. As a consequence, G cannot be obtained and it remains unknown.

However, assuming that the change in scattering is small compared to the change in absorption, the hypothesis behind the detection of NIRS signals is that G is time-invariant during the time of measurement [18]. Hence, since the level of scattering is considered constant, the variation of absorbance A can be calculated, although the baseline value is still unknown. As a result, the equation (1.2.1) becomes

$$\Delta A = \alpha \cdot \Delta c \cdot d \cdot B \qquad (1.2.2)$$

which is used to calculate the relative concentrations of chromophores. Therefore, NIRS instruments which simply adopt algorithms based on the modified Lambert-Beer law (MLBL) (equation 1.2.2) can only monitor a *trend* in the concentration changes of chromophores, while no actual information about the absolute values can be achieved.

Adopting the equation (1.2.2) it is then possible to solve the following system of equations used to calculate the relative concentrations of both O_2Hb and HHb.

$$\begin{aligned}
\Delta A_{\lambda_1} &= \alpha_{\lambda_1}^{HHb} \cdot \Delta c^{HHb} \cdot d \cdot B + \alpha_{\lambda_1}^{O_2Hb} \cdot \Delta c^{O_2Hb} \cdot d \cdot B \\
\Delta A_{\lambda_2} &= \alpha_{\lambda_2}^{HHb} \cdot \Delta c^{HHb} \cdot d \cdot B + \alpha_{\lambda_2}^{O_2Hb} \cdot \Delta c^{O_2Hb} \cdot d \cdot B
\end{aligned} \qquad (1.2.3)$$

where λ_1 and λ_2 are the two different wavelengths used to detect O_2Hb and HHb. For each equation, both the contribution of absorption by O_2Hb and HHb are considered since they both absorb light every time a wavelength is emitted.

The MLBL is valid under the hypothesis of homogeneous change in hemoglobin concentrations and of homogeneous tissue, but this approximation leads to an underestimation of the changes in the concentrations. As a consequence, while this may not be a relevant issue in brain research, where it is sufficient to detect the *presence* of brain activation and where it occurs [18], it can be an obstacle in medical applications [14].

1.3   NIRS Signal Detection

The source of radiation used in NIRS instruments is often LED light, while the detector probe consists in a photodiode converting the incoming light into electric current (figure 1.3.1). Thus, the electric signal generated by light attenuation is then converted into chromophore concentration changes by a computer. The measured variables (i. e. O_2Hb and HHb concentrations) are monitored in real-time. To reduce the noise signal related to the external environmental light, the detection probe is generally isolated by a black plastic covering and both probes are placed as tight as possible on the patients' skin (typically on their forehead).
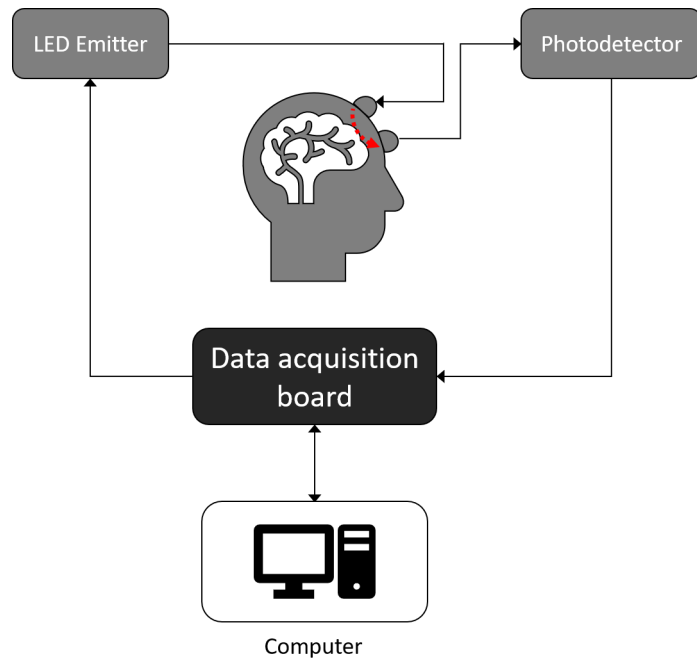
Figure 1.3.1: NIRS detection scheme

An example of NIRS signal showing the changes in cerebral hemoglobin concentration is reported in figure 1.3.2.
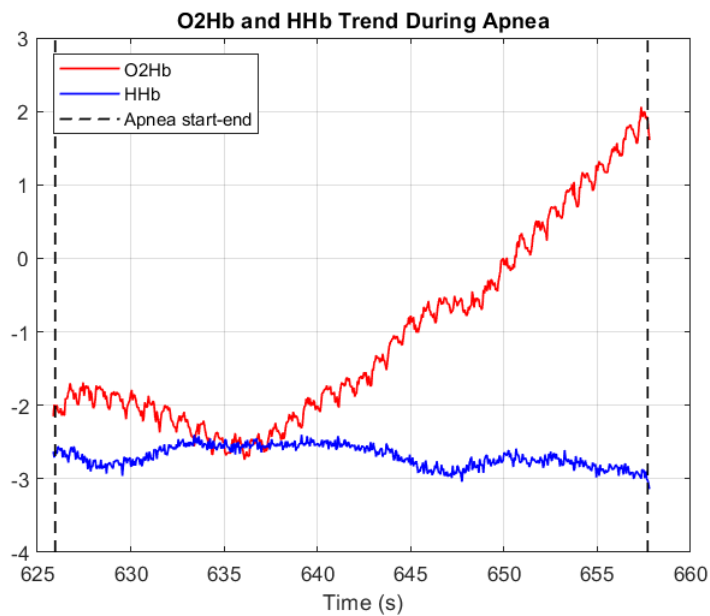

Figure 1.3.2: Example of NIRS signal showing changes in O_2Hb and HHb concentrations during voluntary apnea

Three different detection modes are commonly used in NIRS (figure 1.3.3)[18][14]:

1. *continuous wave (CW)*;

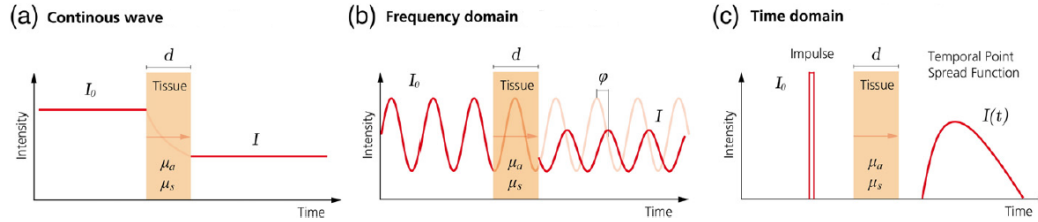2. *time domain (TD)*;

3. *frequency domain (FD)*.

Figure 1.3.3: Functioning of the three NIRS detection modes

1.3.1 Continuous Wave (CW)

The CW-based NIRS instruments emit the input light at constant intensity through the tissue and then measure the re-emerging diffusely reflected light [18].

These instruments are the least expensive available but this kind of measurement has some important drawbacks. The main disadvantage of this method is that the absolute values of O_2Hb and HHb concentrations are not measurable. However, with the assumptions used in the MLBL (equation 1.2.2) it is possible to quantify changes in these variables so that CW-based NIRS monitors at least can work as trend monitors [18].

1.3.2 Time Domain (TD)

The TD-based NIRS instruments emit a very short impulse of light through the tissue and then measure the time of flight of the emerging photons [18].

The measured time of flight is related to the pathlength followed by the light through the head. The main advantage of this method is therefore the availability of information about the scattering and absorption properties of the medium, based on the measurement of the photons time of flight through the head, so that it is then possible to provide the absolute values of hemoglobin concentration. The main drawback of this technology is its high cost compared to the more simple CW method [14].

1.3.3 Frequency Domain (FD)

The FD-based NIRS instruments modulate the emitted light intensity, then they measure the intensity of the detected light and its phase shift [18].

The measured phase shift is proportional to the actual pathlength followed by the light through the head and is wavelength specific [13]. Therefore, this technology allows to calculate the pathlength followed by the photons by using the obtained phase data [14]. Thus, it is possible to quantify absorption and scattering by the tissues and finally the absolute values of O_2Hb and HHb concentrations [13].

15

1.4   NIR Spatially Resolved Spectroscopy (SRS)

As already discussed aboove, various types of methods have been adopted during the years in NIRS instruments and they can be recapped as follows [19].

1. Methods based on CW technology:

   (a) MLBL method;
   (b) spatially resolved spectroscopy (SRS);

2. methods based on TD technology:

   (a) time resolved spectroscopy (TRS);

3. methods based on FD technology:

   (a) phase resolved spectroscopy (PRS).

Suzuki et al. [19] have developed a NIRS oxygenation monitor machine called NIRO 300 (Hamamatsu Photonics, Hamamatsu, Japan), which is able to determine a tissue oxygenation index (TOI) and a tissue hemoglobin index (THI) by using SRS and to measure hemoglobin concentration changes[1] by using MLBL.

According to the theory of photon diffusion approximation in a highly scattering medium, in their instrument Suzuki et al. [19] use the calculated intensity of reflected light $R(\rho, t)$ to determine the light attenuation $A(\rho)$ as

$$A(\rho) = -\log \int_0^\infty R(\rho, t)\, dt \qquad (1.4.1)$$

where ρ and t are the distance and the time from the input respectively.

Indicating with L the differential pathlength in the MLBL (equation 1.2.2), which is the product of the DPF B and the pathlength d, the attenuation change ΔA can be defined as follows.

$$\Delta A = \alpha \cdot \Delta c \cdot L \qquad (1.4.2)$$

The differential pathlength L analytically coincides with the product between the light velocity v and its mean time of flight T through the medium:

$$L = v \cdot T \qquad (1.4.3)$$

where T is defined as

$$T = \frac{\displaystyle\int_0^\infty t R(\rho, t)\, dt}{\displaystyle\int_0^\infty R(\rho, t)\, dt} \qquad (1.4.4)$$

---

[1]In this section the simplified notation $\Delta c^{O_2Hb} = \Delta O_2Hb$ and $\Delta c^{HHb} = \Delta HHb$ will be used to indicate concentration changes

Hence, by measuring $R(\rho, t)$, T is calculated as the temporal mean of the measured $R(\rho, t)$ (see equation 1.4.4) and the differential pathlength L is finally known.

As previously described, through the MLBL it is possible to detect different chromophores concentration changes by using different wavelengths and then solving a proper system of equations (see equations 1.2.3). NIRO 300 uses four different wavelengths, which are 775 nm, 810 nm, 850 nm and 905 nm, to measure three components concentration changes: ΔO_2Hb, ΔHHb and $\Delta CtOx$. The latter is the concentration change of cytochrome oxidase, which is another absorber often detected in NIRS oximetry along with O_2Hb and HHb. Thus, the concentration changes are calculated by solving the following matrix equation.

$$\begin{bmatrix} \Delta O_2Hb \\ \Delta HHb \\ \Delta CtOx \end{bmatrix} = \frac{1}{L} \cdot [\alpha_{i,j}]^{-1} \cdot \begin{bmatrix} \Delta A(\lambda_1) \\ \Delta A(\lambda_2) \\ \Delta A(\lambda_3) \\ \Delta A(\lambda_4) \end{bmatrix} \tag{1.4.5}$$

where $i = O_2Hb, HHb, CtOx$ and $j = \lambda_1, \lambda_2, \lambda_3, \lambda_4$, which are the four wavelengths employed.

The principle of the SRS method consists in calculating the derivative of $A(\rho)$ with respect to ρ, which is a function of the attenuation (μ_a) and reduced scattering (μ'_s) coefficients, as indicated by the equation (1.4.6).

$$\frac{\partial A}{\partial \rho} = \frac{1}{\ln 10} \left(\sqrt{3 \mu_a \mu'_s} + \frac{2}{\rho} \right) \tag{1.4.6}$$

Hence, by measuring $\dfrac{\partial A}{\partial \rho}$ at several wavelengths thanks to the multiple segments on the photodetector (see figure 1.4.1), it is possible to determine μ_a and μ'_s. The latter depends on the wavelength λ and it is expressed as

$$\mu'_s(\lambda) = k \cdot (1 - h \cdot \lambda) \tag{1.4.7}$$

where h is the normalized slope of μ'_s along λ and k is the constant scattering contribution. Finally the relative attenuation coefficient $k\mu_a$ can be calculated from the equation (1.4.6) as

$$k\mu_a(\lambda) = \frac{1}{3(1 - h\lambda)} \left(\ln 10 \cdot \frac{\partial A}{\partial \rho} - \frac{2}{\rho} \right)^2 \tag{1.4.8}$$

As a result, the relative concentrations kO_2Hb and $kHHb$ can be calculated by using three wavelengths and then solving the following matrix equation.

$$\begin{bmatrix} kO_2Hb \\ kHHb \end{bmatrix} = [\alpha_{i,j}]^{-1} \cdot \begin{bmatrix} k\mu_a(\lambda_1) \\ k\mu_a(\lambda_2) \\ k\mu_a(\lambda_3) \end{bmatrix} \tag{1.4.9}$$

where $i = O_2Hb, HHb$ and $j = \lambda_1, \lambda_2, \lambda_3$.

Lastly, the TOI and the THI can be determined as

$$TOI = \frac{kO_2Hb}{kO_2Hb + kHHb} \tag{1.4.10}$$

$$THI = kO_2Hb + kHHb \tag{1.4.11}$$

According to the definitions in equations (1.4.10) and (1.4.11), TOI can be interpreted as a measure of the relative changes in tissue oxygenation, while THI represents the tissue blood volume. In fact, according to the definition (1.4.11), THI indicates the total hemoglobin concentration detected and, as a consequence, it can be associated to the total blood volume, as hemoglobin is a large blood component.

Anyway, a major issue concerning NIRS signals is the way they are affected by the extracranial circulation, which is not of interest in cerebral oximetry, whose main focus is on the cortical tissue oxygenation at different levels. Some authors in the past already pointed out the disadvantageous effects of extracranial circulation on NIRS recordings, which may lead to misinterpretations of these signals [20], [21], [22]. This is the reason why the algorithm series described in section 1.3 and in this section describing the SRS have been developed. As reported by Canova et al. [23], under some circumstances, the quantities estimated through the MLBL (ΔO_2Hb and ΔHHb) are more affected by the extracranial circulation than those estimated through the SRS algorithm (TOI and THI). For this reason, to obtain the heartbeat (HBI) information, the TOI and THI data will draw the main focus of this work.

NIRO 300 by Hamamatsu Photonics uses pulsed laser emitter diodes and a detector probe with a sensitivity able to maintain an emitter-detector distance equal to 5 cm in most cases, allowing a measuring volume of several cubic centimeters. The detector is made of three sensors placed at different distances from the light source (figure 1.4.1).
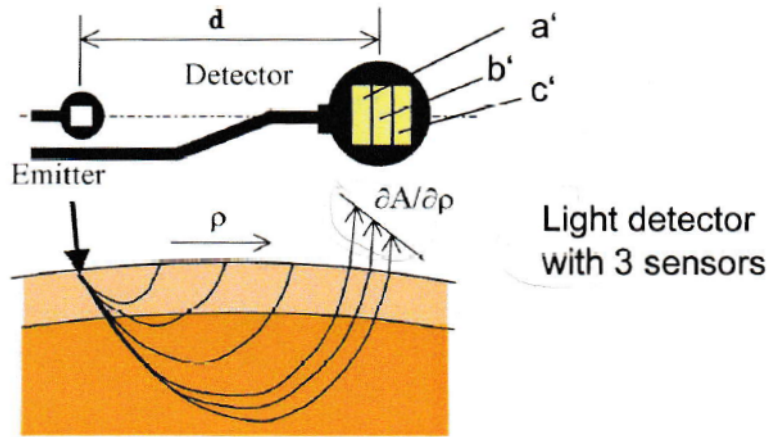
Figure 1.4.1: NIRO 300 detection scheme

For large enough values of distance ρ from the emitter, the scatter distribution is so homogeneous that the scatter loss in a' and b' is basically the same. Hence, any difference in the intensity value of the detected light between a' and b' can be interpreted as a difference in absorption at these locations and the local absorption change can be considered as a function of ρ.

1.5 NIRO-200NX by Hamamatsu Photonics

The version of the monitor used in this work is the NIRO-200NX by Hamamatsu Photonics (figure 1.5.1) and its main features are:

- five signal outputs

    - TOI (%);
    - nTHI (arbitrary unit);
    - O_2Hb (μM);
    - ΔHHb (μM);
    - total hemoglobin change ΔcHb (μM);

- maximum sampling frequency equal to 20 Hz;

- LED light source using three wavelengths (735 nm, 810 nm and 850 nm);

- two segments photodiode detector.

Figure 1.5.1: NIRO-200NX (Hamamatsu Photonics)

According to the indications provided by the producer, if L is known, $\Delta O_2 Hb$ and $\Delta H H b$ are measured as absolute concentration changes $\Delta \mu M$. When $d > 3$ cm, L and

19

d are related through the DPF as $L = DPF \cdot d$. Hence, if DPF is known, L can be accordingly estimated. As discussed above, DPF values can be found in literature and for the human adult head a common DPF value is 5.93. Hamamatsu Photonics provides some DPF common values to use during the acquisition with NIRO-200NX. Alternatively, when L is unspecified, the unit adopted for $\Delta O_2 Hb$ and ΔHHb can be set as $\Delta \mu M \cdot cm$. Furthermore, the unit of TOI is %, while THI has no unit of measure. Lastly, nTHI is a normalized version of THI being generally displayed by the monitor and it is defined as:

$$nTHI(t) = \frac{THI(t)}{THI(0)} \qquad (1.5.1)$$

which is basically the ratio between the THI at a generic instant t during the acquisition and the THI calculated at the beginning of the acquisition ($t = 0$). In the diagrams reported in this work the explicit units of O_2Hb and TOI are omitted.

1.6   NIRS Applications

After its initial spread, NIRS started to be used to obtain the average oxygen saturation in the arteriolar, capillary and venous districts of many tissues and it settled together with other technologies which use pulsed signals to measure peripheral oxygen saturation (like pulse oximetry) [14]. However, when compared to pulse oximetry, NIRS stands out for its greater tissue penetration, the ability to provide global information about oxygenation in *all* the vascular compartments and the possibility of characterizing more chromophores than pulse oximetry by adopting more wavelengths [13].

Hence, NIRS became very popular in cerebral oximetry, which is a vital mean for monitoring patients in intensive care units. In fact, this technique is suitable for long-term applications since it provides continuous real-time information, it does not interfere with other instruments, it is non-invasive and it can be done at the patients' bedside [15]. In addition to that, its ease of use and minimal interoperator variability in detection are other notable features [14]. Besides, its introduction as an oximetry tool outdid jugular venous bulb oxygen saturation technique, which is invasive and inclined to artefacts [13].

Nevertheless, NIRS is also employed in neonatology, in short-term applications, such as monitoring patients undergoing surgery, and it has also been studied in the context of traumatic brain injury [14].

This technique represents a valuable tool for monitoring brain oxygenation, especially considering the relevance of the cerebral autoregulation mechanism. According to this physiological phenomenon, when the cerebral perfusion pressure (CPP) increases or decreases (within some limits), the CBF is maintained constant to prevent any cellular damage, hence a hemodynamic change in the organ occurs. Besides, autoregulation works by sectors on the cerebral cortex, depending on the specific metabolic need of every area. It is noteworthy that NIRS has been also employed to obtain an index of autoregulatory vasoreactivity to create a clinical tool able to determine the quality of the patients' cerebral autoregulation [24].

Along with the CPP, other pressures play an important role in the cerebral autoregulation, such as the arterial blood pressure and the intracranial pressure, and all of them are

controlled by the shrinking and contracting motion of the blood vessels, thus protecting the tissues against diminished or excessive blood flow.

With reference to conditions like hypocapnia and hypercapnia, which are due to hyperventilation and hypoventilation respectively, clearly they affect the blood flow reaching the cerebral cortex since the amount of O_2 and CO_2 exchanged by the cerebral cells must always be regulated carefully and therefore the blood flow to those tissues must be properly adjusted.

As a result, monitoring the perfusion level of the brain means achieving important information related to the hemodynamic in the vessels of that region. In fact, NIRS-based methods have been developed to achieve the absolute quantification of CBF and cerebral blood volume (CBV) [13].

Chapter 2

Signals Acquisition Procedure

The NIRS signals used in this work have been obtained by two different groups of subjects:

- six healthy subjects (HS);

- six patients (PT) suffering from atrial fibrillation (AF).

The patients participating to the experiment were previously asked to give their written formal consent to undergo this experiment, which has been approved by the Local Ethical Committee. These subjects were patients of the cardiology day-hospital unit of *Città della Salute e della Scienza di Torino* hospital, in Turin, where they received a scheduled cardioversion (CV) as part of their therapy.

All the signals obtained in these experiment sessions were processed through appropriate codes implemented in MATLAB software and by using the two included apps Signal Analyzer and Curve Fitting.

2.1 Signals Acquisition on the Healthy Subjects

The HS have been tested under five different conditions in the following order:

1. baseline recording;

2. voluntary apnea;

3. hyperventilation;

4. Valsalva maneuver;

5. head down.

Table 2.1.1 contains the details about the participants.

Table 2.1.1: Participating healthy subjects characteristics

Subject	Sex	Age
1	F	25
2	F	51
3	M	24
4	M	24
5	F	24
6	F	37

2.1.1 Tests Description

Table 2.1.2 recaps the testing conditions with the corresponding duration and the number of participating subjects to each of them.

Table 2.1.2: Conditions summary (in alphabetical order)

Conditions	Performing Subjects	Duration
Apnea (AP)	6	30 s
Baseline (BL)	6	4 min
Head Down (HD)	5	15 s
Hyperventilation (HV)	6	15 s
Valsalva Maneuver (VM)	6	15 s

All the subjects under each condition were tested in supine position with closed eyes and were asked to stay as much still as possible to reduce motion artifacts.

For each subject all the listed tests were performed in the same order within the same recording session and using time markers on the registering signals to distinguish the beginning and the ending of each testing condition as shown by the scheme in figure 2.1.1. After every testing condition, some minutes of break were taken to restore the baseline condition before a new test started.
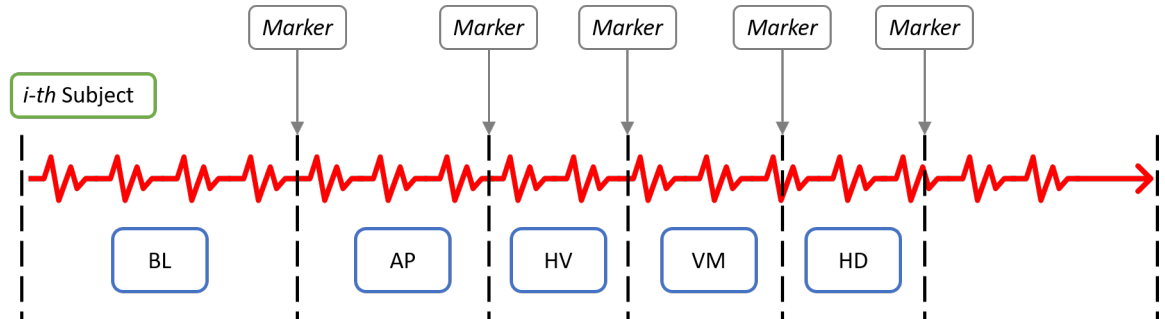
Figure 2.1.1: Recording scheme

The Baseline (BL) condition in table 2.1.2 refers to the recording of 4 min of normal breathing at normal heart sinus rhythm (NSR).

During the Apnea (AP) condition the subjects were asked to hold their breath for about 30 s.

In the Hyperventilation (HV) test the subjects were asked to increase their respiratory frequency, trying to keep the reached rhythm steady over 15 s without dropping it.

In the Valsalva Maneuver (VM) test the subjects were asked to perform this maneuver for 15 s. The Valsalva maneuver consists in contracting the abdominal muscles as much as possible while holding the breath by pinching the nose shut and with the mouth closed.

The Head Down (HD) test consisted in making the subjects passively tilt their head and keep it down over the upper extremity of the table for 15 s. To guarantee the passiveness of the movement, an operator would hold their head to make it move, while the subjects were asked to completely relax their neck muscles. As reported in table 2.1.2, this test was performed only by five subjects over six, since subject 2 was not tested under this condition.

2.1.2 Signals Acquisition Setup

The NIRS signals acquisition system adopted in this work is the NIRO-200NX monitor (Hamamatsu Photonics), which acquired, sampled (20 Hz), digitally converted and transferred the signals to a PC station where they were visualized in real time, as shown in the scheme in figure 2.1.2.
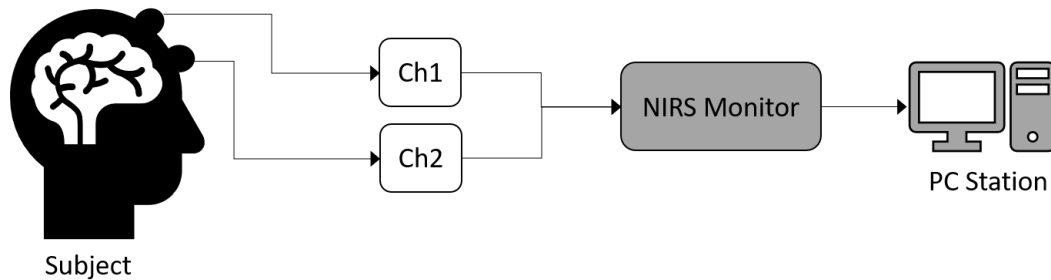
Figure 2.1.2: Acquisition scheme (for HS)

As described in chapter 1 section 1.5, the NIRO-200NX monitor is able to output up to five types of signals:

- three directly measured quantities (O_2Hb, ΔHHb and ΔcHb);

- two quantities obtained from the application of the Spatially Resolved Spectroscopy (SRS) algorithm (TOI and nTHI).

Two acquisition channels have been used for each subject under each condition. The first attempt was to use two channels with different source-detector (SD) distances for all subjects, but this was not possible for subjects 3 and 4 because of technical issues. Besides, subject 4 encountered technical issues concerning channel 2, making the signals

coming from this source scarcely reliable. Table 2.1.3 reports the channel configurations adopted for each subject with the corresponding SD distance. For each subject a DPF = 5.93 has been set.

Table 2.1.3: Channel configurations adopted

Channel Configurations for Each Subject (SD Separation Values)								
Subject 1	Ch1	4 cm	Subject 3	Ch1	3 cm	Subject 5	Ch1	4 cm
	Ch2	3 cm		Ch2	3 cm		Ch2	3 cm
Subject 2	Ch1	4 cm	Subject 4	Ch1	4 cm	Subject 6	Ch1	4 cm
	Ch2	3 cm		Ch2	4 cm		Ch2	3 cm

As already discussed in chapter 1 section 1.2, different SD distances reflect different investigation volumes on the subject's head. Specifically, shorter SD separations lead to smaller investigation volumes, while longer distances lead to bigger volumes.

The optodes where placed on the right and the left side of the subject's forehead avoiding contact with the hair and were properly fixed and covered in a black rubber covering to reduce the environmental light noise.

2.1.3   Output Signals

Overall, every channel yielded four output signals:

- O_2Hb;

- ΔHHb;

- TOI;

- nTHI;

All the signals were visualized by using the NIRO-200NX Display Software (Hamamatsu Photonics) during the acquisition procedure and the recorded data have been imported into MATLAB software environment for post-processing purpose.

Among the signals listed above, only O_2Hb, TOI and nTHI were considered. Thus, for each subject six signals were available in total. After the measurements, the available time series from each subject have been segmented according to the time intervals when the different testing conditions took place (see figure 2.1.1). This led to a total number of available time series equal to $(6 \times 6 \times 5) - 6 = 174$ (since the HD condition lacks one subject). The scheme in figure 2.1.3 shows how the available data have been organized to be further processed.
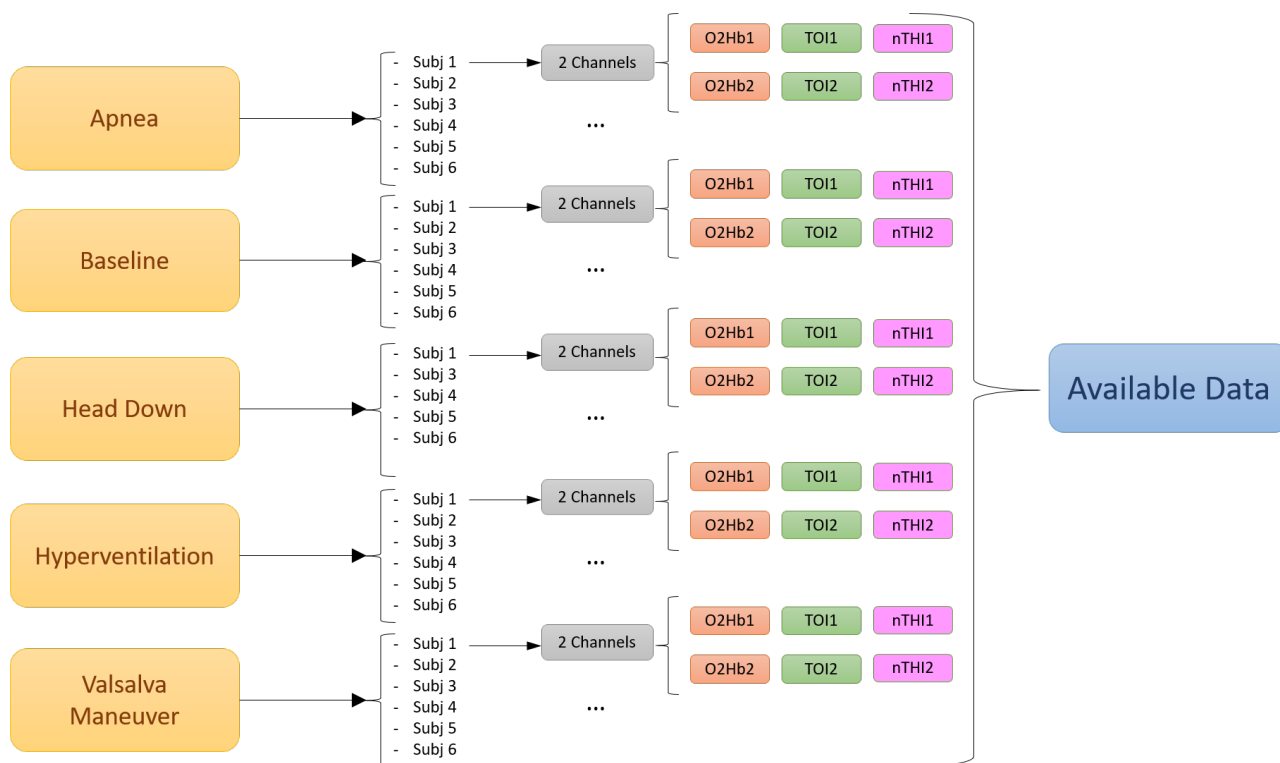
Figure 2.1.3: Data organization scheme

2.2 Signals Acquisition on the Patients

The PT tested suffer from AF and underwent a clinical cardioversion (CV) to restore the normal sinus rhythm (NSR).

The aim of the NIRS recording on these subjects is the evaluation of the change in the HBI information extracted from the recorded NIRS signals *before* and *after* the CV, hence only subjects whose NSR was successfully restored after the CV have been accounted. As a consequence, only two testing conditions are considered in this case:

1. pre-CV condition (Pre-CV);

2. post-CV condition (Post-CV);

Table 2.2.1 contains the relevant details of the patients participating to the experiment.

Table 2.2.1: Participating patients characteristics

Subject	Sex	Age	Drugs	Prev. TEE	ECG
1	F	62	Midazolam	Yes	No
2	M	82	Midazolam	Yes	No
3	F	75	Coumadin	No	Yes
4	M	19	Midazolam	Yes	Yes
5	M	79	Xarelto - Midazolam	Yes	Yes
6	M	55	Coumadin	No	Yes

Some patients underwent a trans-esophagus echography (TEE) before the CV took place and were administered Midazolam as anesthetic during that procedure. For this reason, some of the patients undergoing TEE were possibly still under the anesthetic effect before the CV procedure started, hence this condition was taken into account.

Lastly, the ECG column in table 2.2.1 refers to the availability of ECG data for that specific patient.

2.2.1   Signals Acquisition Setup

Overall, in the experimental session involving the PT, three different monitoring systems were adopted and the signals coming from these systems were simultaneously obtained:

- NIRO-200NX (Hamamatsu Photonics) as NIRS monitor;

- Capnostream20p (Medtronic) as oxygen saturation (SpO2) monitor (figure 2.2.1);

- Dynascope Monitor DS-7100 (Fukuda Denshi Co.) as ECG monitor (figure 2.2.2).

Figure 2.2.1: Capnostream20p (Medtronic)

Figure 2.2.2: Dynascope Monitor DS-7100 (Fukuda Denshi Co.). Here the DS-7200 version is displayed as an example.

During the acquisition, the analog signals coming from the SpO2 and the ECG monitors were synchronized, sampled and transferred to a PC station by a multichannel acquisition system (CED Micro1401-3)(figure 2.2.3), while the NIRS signals coming from the NIRS monitor were independently sampled, digitally converted and transferred to the same PC station by the NIRS monitor, as shown in the scheme in figure 2.2.4.

Figure 2.2.3: CED Micro1401-3
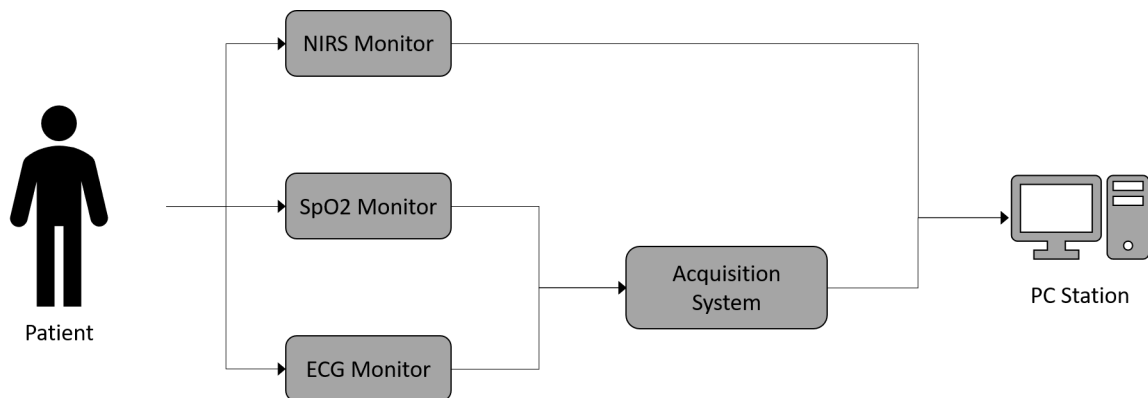
Figure 2.2.4: Acquisition scheme (for PT)

Table 2.2.2 recaps the sampling frequencies adopted for each kind of recorded signal.

Table 2.2.2: Instruments and sampling frequencies adopted

Instrument	Signals of Interest	Sampling Frequency
NIRO-200NX	O_2Hb, TOI and nTHI	20 Hz
Capnostream20p	SpO2	400 Hz
Dynascope Monitor DS-7100	ECG	400 Hz

The synchronization between the NIRS signals and those acquired by the acquisition system was obtained by setting event markers at the beginning and the ending of each acquisition.

Furthermore, as the NIRO-200NX monitor lacks electrical isolation against CV, this

monitor had to be disconnected immediately before the CV and reconnected only afterwards to avoid electrical issues and damages. Hence, two other markers were set correspondingly to the beginning and the ending of the CV, during which no NIRS signal could be acquired. Meanwhile, the acquisition system kept collecting the SpO2 and the ECG signals also during the CV.

For NIRS signals acquisition, similarly to the HS tests, two acquisition channels were used on the PT as well, but in this case the SD separation adopted was the same for both channels and equal to 4 cm (with a DPF set equal to 5.93).

Also in this case, the NIRS probes were placed on the right and on the left side of the patient's forehead, avoiding contact with the hair and were properly fixed and covered in a black rubber covering to reduce the environmental light noise.

The SpO2 was monitored by using a pulse oximeter sensor placed on a finger of the patient. Two different SpO2 signals were obtained:

- SpO2 waveform;

- SpO2 square wave.

The ECG was monitored using twelve leads but only the second lead (II) could be exported as analog signal to the acquisition system.

The ECG and SpO2 signals were not available for *all* the tested patients as indicated by table 2.2.1. In fact, for some patients, at the time of the acquisition the complete setup including the multichannel acquisition system was not available yet.

2.2.2 Experimental Session Description

During the acquisition, the patients were laying in supine position on a hospital bed and were asked to stay as much still as possible to reduce motion artifacts while keeping their eyes closed. Hence, most of the acquisition time, the patients laid calm, with closed eyes and sometimes fell asleep. The acquisitions generally lasted from 2 to up to 3 hours, comprehensive of the CV procedure. Thus, sudden events like movements, speaking or cough were inevitable and the operators tried to catch them by setting proper event markers on the recording signals as much as possible to be further deleted in the signal processing. The recorded signals were then visually inspected and only the pieces where the patients seemed to be mostly calm and where movement artifacts were mostly absent for both the Pre-CV and Post-CV conditions were considered.

With reference to the NIRS signals, generally 20-30 min of recording before the CV and 20-30 min of recording after the CV were considered for the signals analysis. Hence a total number of NIRS time series equal to $(6 \times 6 \times 2) = 72$ is available.

The indicative global post-recording signals subdivision based on the markers placed during the acquisition is reported in the scheme in figure 2.2.5.
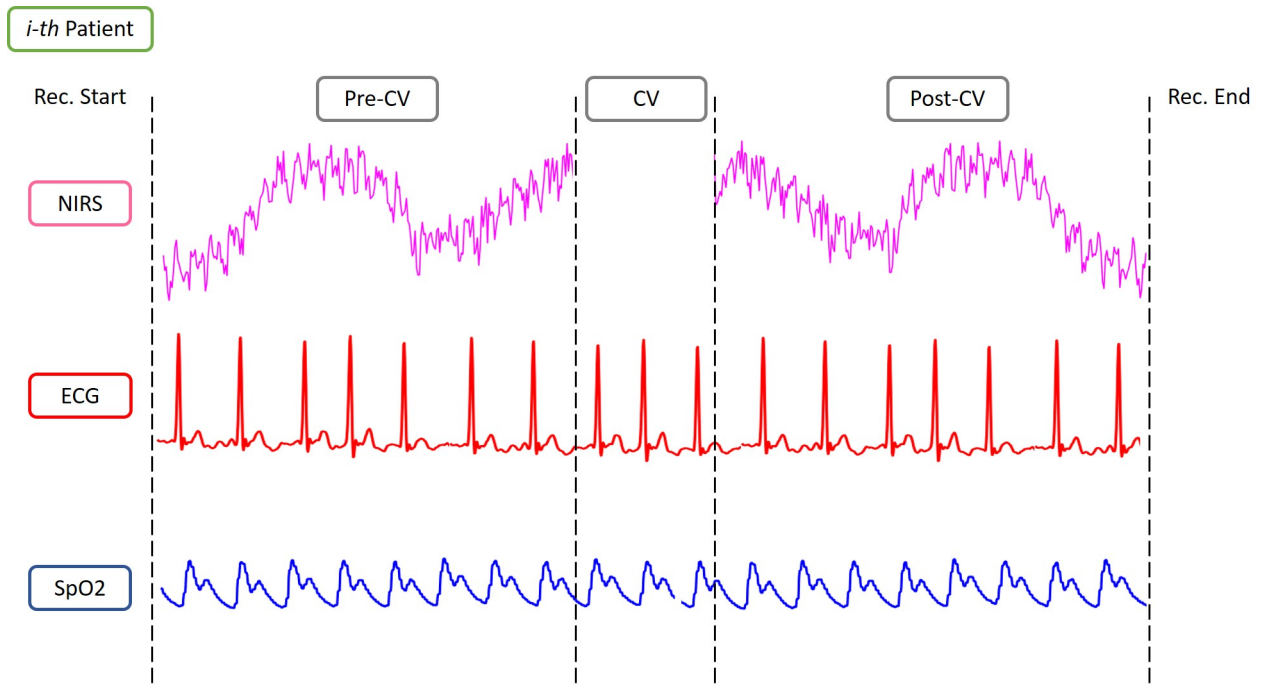
Figure 2.2.5: Recording scheme (signals inserted here only as visual example)

Lastly, the scheme in figure 2.2.6 recaps the organization of the available data belonging to the experimental sessions on the PT.
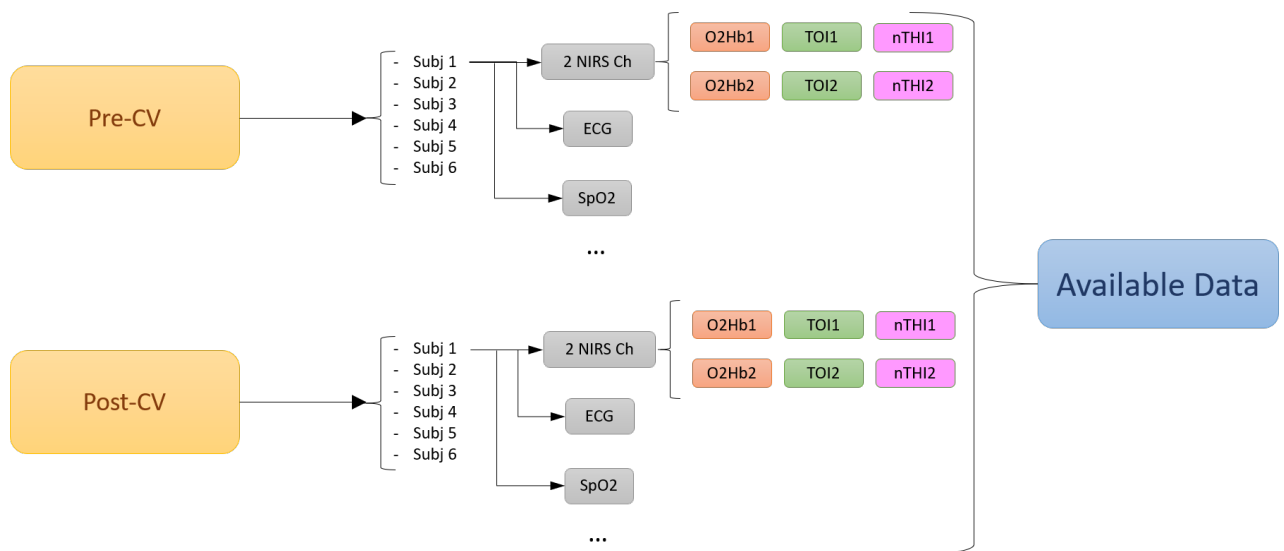
Figure 2.2.6: Data organization scheme

2.3 Examples of Output Signals

Figures 2.3.1 and 2.3.2 show an example of the detected signals from PT3 including the NIRS signals and the ECG and SpO2 signals acquired in sync.
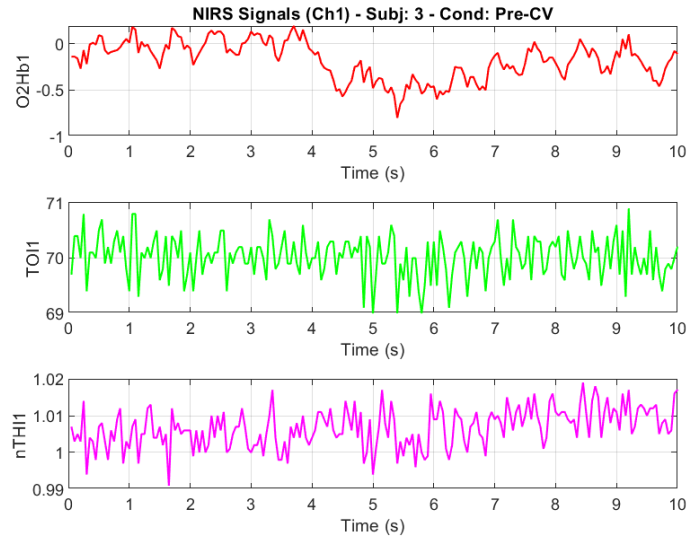
Figure 2.3.1: Example: NIRS signals from channel 1 of PT3 during Pre-CV condition (only 10 s displayed)
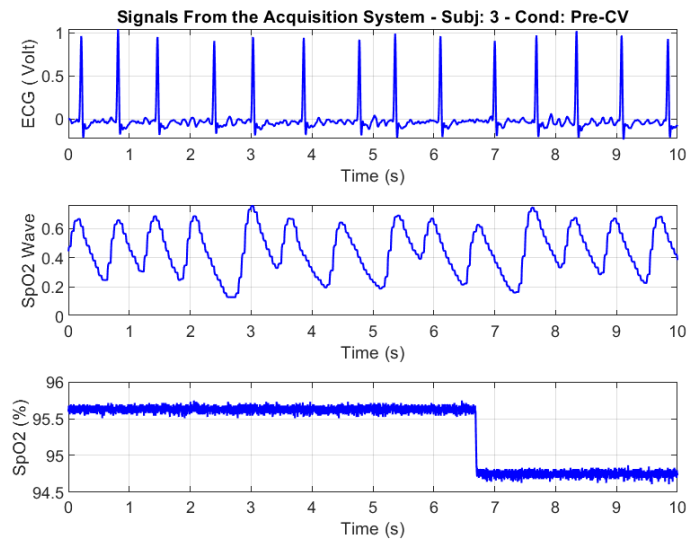
Figure 2.3.2: Example: ECG and SpO2 signals from PT3 during Pre-CV condition (only 10 s displayed)

As discussed in chapter 1 section 1.4, under some circumstances TOI and nTHI may represent information about blood circulation at a deeper location within the investigation volume, while O2Hb is more affected by the extra-cranial circulation. For the purpose of this work, hence only the TOI and nTHI signals will be considered as the main source of the heartbeat interval (HBI) information, which can be extracted by measuring the peak-to-peak time distance.

However, this choice comes with a problem concerning the time morphology of these signals. In fact, TOI and nTHI appear mostly random-like signals and, except some encountered cases during their recording, they are not likely to show a clear HBI information over time, meaning that the HBI values extraction from these signals can be very difficult. Besides, TOI and nTHI signals show more inter-subjects variability when compared to O2Hb. This issue will be faced in chapter 5.

Another problem needing to be addressed and related to all the detected NIRS signals is the slow trend at low frequency, which is visible in the examples in figure 2.3.1. The slow trend is not of interest for the purpose of this work and thus it should be removed. The signals detrending issue will be dealt in chapter 3.

Chapter 3

Signals Detrending

The dataset of NIRS signals described in chapter 2 underwent a detrending process consisting in different trials to determine the most suitable detrending approach. Detrending these signals is essential to remove the low frequency components responsible for their slow trend, which is not of interest for the purpose of this work. The original signals detected from channel 1 of HS1 under BL condition are shown as an example in figure 3.0.1. The low frequency slow trend is clearly visible in all the three signals.
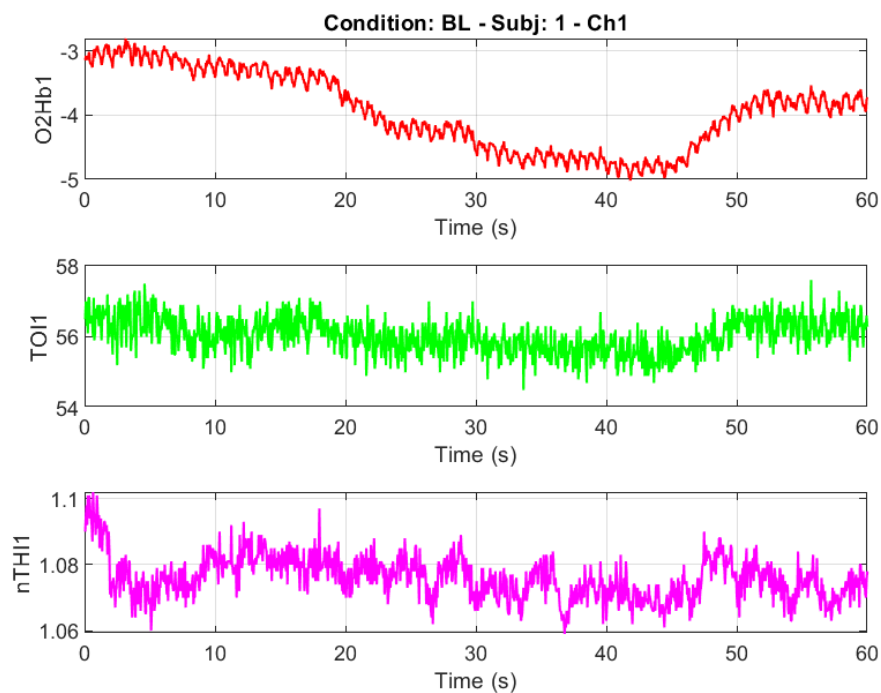
Figure 3.0.1: Example: 60 s of original signals before detrending (channel 1, HS1 under BL condition)

The performed detrending trials may be grouped in two main approaches:

- *filtering approach*;

- *curve fitting approach.*

The two approaches mainly differ for their domain of application. In fact, the filtering approach aims to detrend the signal in the frequency domain, while the curve fitting approach is directly applied to the signal in the time domain.

In this chapter, as an example, only the results belonging to HS1 (healthy subject 1) under BL condition will be presented.

A list of the trials performed is summarized by the scheme in figure 3.0.2.
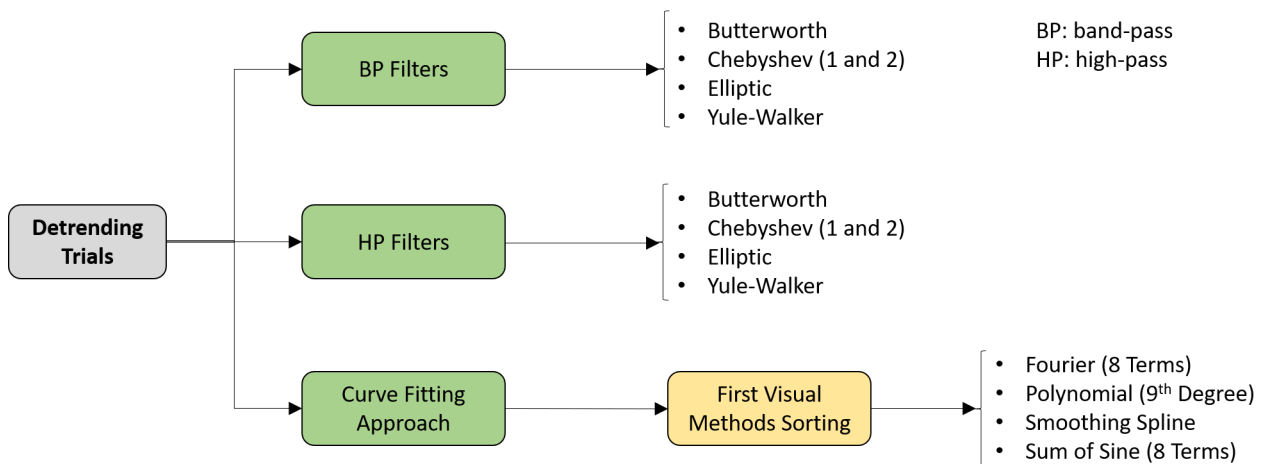
Figure 3.0.2: Scheme recapping the detrending trials performed

3.1   Filtering Approach

In this section the filtering approach with the corresponding trials will be described. As shown in figure 3.0.2, two main types of filters have been adopted:

- band-pass filters (BP);

- high-pass filters (HP).

Besides, for both BP and HP filters, five different filtering algorithms have been tested:

- Butterworth filter;

- Chebyshev 1 and 2 filters;

- elliptic filter;

- Yule-Walker filter.

Among all these filters, Yule-Walker is the only one being directly designed by the user, meaning that the magnitude and frequency masks to apply to the signal are shaped directly and the order of the filter is chosen according to the filter performance. For the other filter types an order estimation function has been used, while the stop-band attenuation amplitude, the maximum ripple amplitude and the stop-band and pass-band frequency ranges have been set. The cut-off frequencies to be respected by the applied filters have been set as [0.4, 4] Hz and 0.4 Hz for the BP and the HP filters respectively. Moreover, every filter has been applied forward and backward to avoid signal phase distortion. Tables 3.1.1 and 3.1.2 list the BP and HP filters parameters adopted in these trials.

Table 3.1.1: BP filters parameters

BP Filters		Butterworth	Chebyshev 1	Chebyshev 2	Elliptic	Yule-Walker
Order	n	8	7	7	5	10
Stop-band Attenuation	R_s	25 dB	50 dB	50 dB	50 dB	
Ripple Amplitude	R_p	0.025 dB	0.025 dB	0.025 dB	0.025 dB	
Cut-off Frequencies	f_c	[0.3, 5] Hz	[0.4, 4] Hz	[0.2, 6] Hz	[0.4, 4] Hz	[0.8, 4] Hz

Table 3.1.2: HP filters parameters

HP Filters		Butterworth	Chebyshev 1	Chebyshev 2	Elliptic	Yule-Walker
Order	n	5	4	4	3	40
Stop-band Attenuation	R_s	50 dB	50 dB	50 dB	50 dB	
Ripple Amplitude	R_p	0.5 dB	0.5 dB	0.5 dB	0.5 dB	
Cut-off Frequencies	f_c	0.3 Hz	0.4 Hz	0.1 Hz	0.4 Hz	0.6 Hz

Figures 3.1.1 and 3.1.2 show the resulting transfer functions (TF) of the BP and HP filters tested.

37
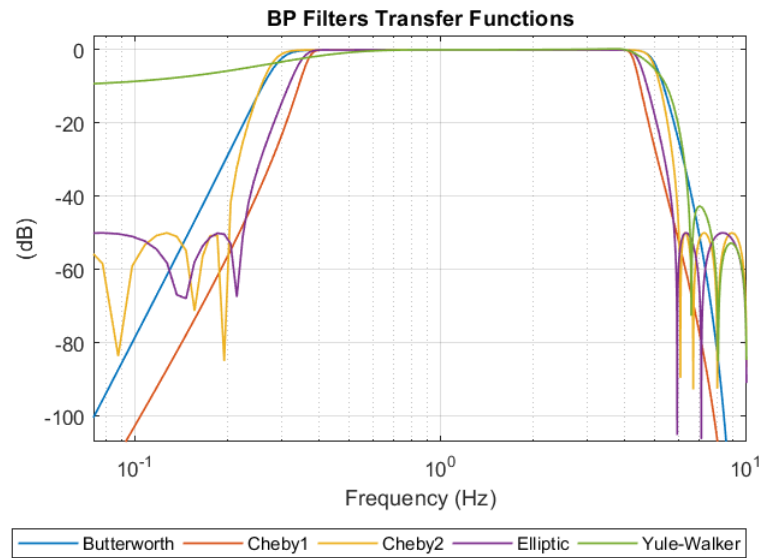
Figure 3.1.1: BP filters TFs
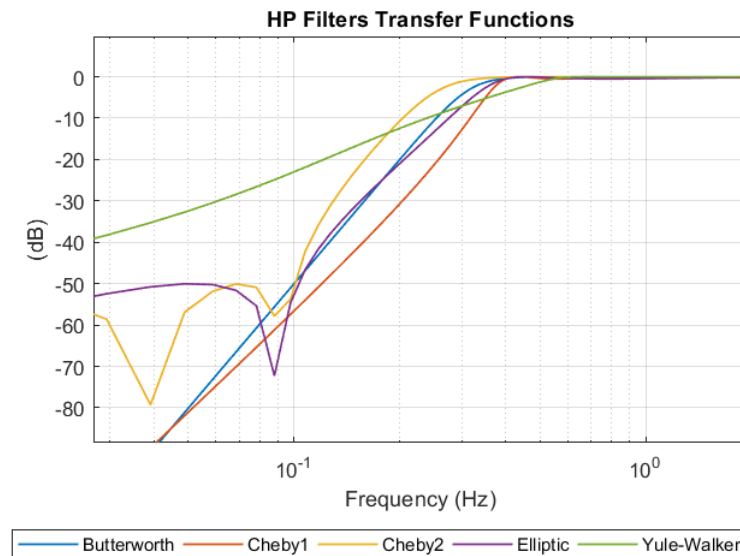
Figure 3.1.2: HP filters TFs

Figures 3.1.3 - 3.1.14 display 10 s of the resulting O2Hb, TOI and nTHI signals from channel 1 of HS1 under BL condition after the application of the BP (3.1.3 - 3.1.8) and HP (3.1.9 - 3.1.14) filters.
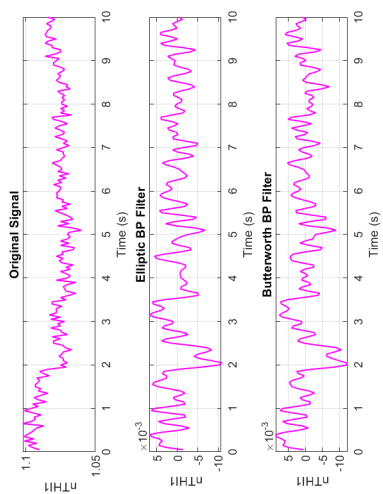
Figure 3.1.3
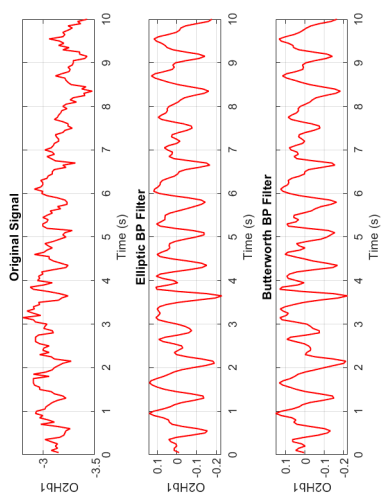
Figure 3.1.5
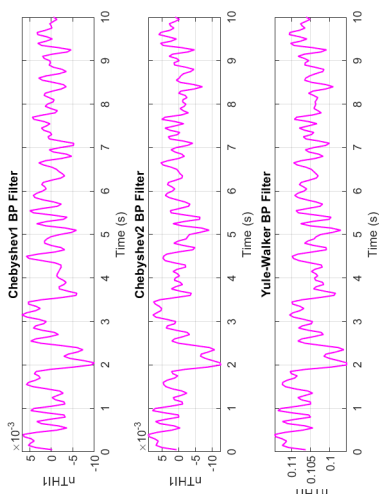
Figure 3.1.7

Figure 3.1.4

Figure 3.1.6

Figure 3.1.8

39
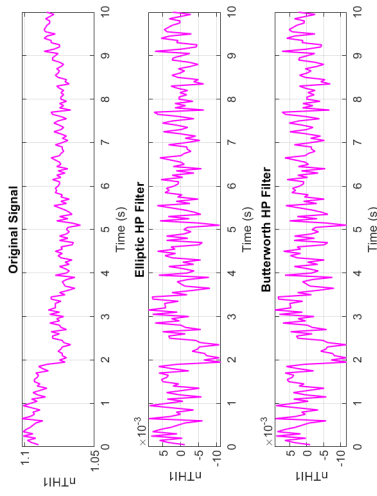
Figure 3.1.13
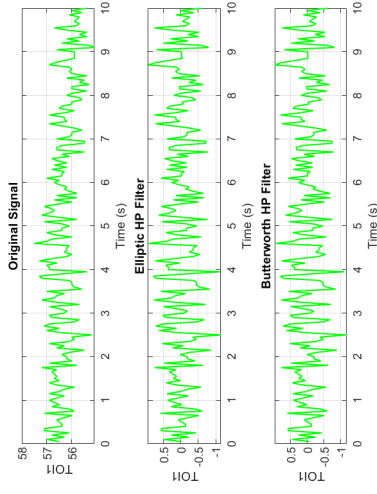
Figure 3.1.11

Figure 3.1.9
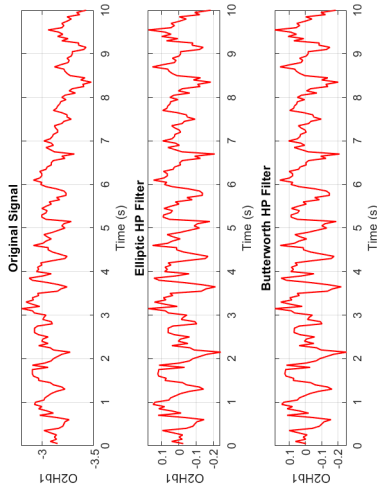
Figure 3.1.14

Figure 3.1.12

Figure 3.1.10
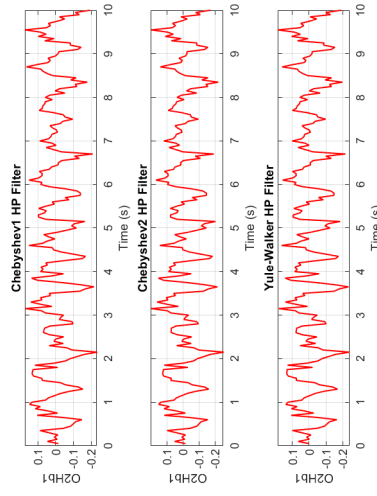
40

According to the TFs reported in figures 3.1.1 and 3.1.2, the Chebyshev 1 and the elliptic filter appear to be the best performing filters in both cases. In fact, they guarantee the steepest decay around the cut-off frequencies, resulting in a large stop-band attenuation. Also the Butterworth BP and HP filters behave quite well, although they cannot guarantee the same steepness. Furthermore, Butterworth BP filter required half of the R_s selected for the other BP filters (see table 3.1.1), as a $R_s = 50$ dB caused great instability in the filter stop-band. Besides, with reference to the filter order, the filters giving the best outcome by employing the smaller order are the elliptic filters. The Yule-Walker filters in this case behave the worst, as they require an exaggeratedly high order to get a proper decay. Lastly, only the Chebyshev 1 and elliptic BP and HP filters respect the initial cut-off frequency requirements expected from the desired filter: [0.4, 4] Hz and 0.4 Hz for the BP and HP versions respectively.

The resulting signals reported in figures 3.1.3 - 3.1.14 show two main relevant features: as expected, the application of a HP filter preserves more information about the original high frequency oscillations and the detrending performances are comparable with those belonging to BP filters, as the same low cut-off frequency and stop-band attenuation have been required (see tables 3.1.1 and 3.1.2). However, for the purpose of this work, BP filters may be favored as they are able to reduce the noisy high frequency oscillations of signals such as TOI and nTHI, which will be used in the next processing to extract the HBI information. Besides, as the HBI duration is the ultimate information needing to be extracted from these signals, all the high frequency oscillations located at frequencies $f \geq 4$ Hz are not much interesting as they would correspond to hypothetical heart rates HR ≥ 240 bpm. In fact, considering both the healthy subjects and the patients tested in this work, this HR value is beyond the maximum value that might be registered on resting subjects, even on those suffering from AF under pharmacological treatment [1], and hence the chosen upper cut-off frequency (4 Hz) may be acceptable to properly filter the NIRS signals.

3.2 Curve Fitting Approach

This approach consists in detecting the curve representing the slow trend of the signal and in the subtraction of the detected trend from the signal in the time domain. Hence, this method is solely based on the time morphology of the signal and the outcome may change accordingly.

Firstly, different methods available in the Curve Fitting Tool provided by MATLAB software have been just visually and qualitatively tested to shortlist only those giving the best fitting result on some sample signals extracted from the dataset. Among all the tested methods, four of them have been finally sorted:

- *Fourier* (8 terms);

- *polynomial* (9$^{\text{th}}$ degree);

- *smoothing spline*;

- *sum of sine* (8 terms).

Generally MATLAB provides each method with the corresponding coefficient of determination (R^2), estimating the goodness of the performed fitting process, which is useful in statistical analysis to determine if the adopted model is able to properly detect the trend of the scattered collected data. R^2 value ranges from 0 to 1, where $R^2 = 1$ represents an optimal fitting. However, the main intention here is detecting the slow trend of the studied signals, meaning that the goodness of the fitting should be related to the ability of the method of capturing only the low frequency trends, excluding all the information belonging to higher frequencies oscillations, which has to be preserved instead. Hence, R^2 may not be the most appropriate estimator to evaluate the performed fitting for this purpose, however its values will be shown as complementary information and it will be used as an indicative additional discriminant for the tested methods.

Before quantitatively testing the shortlisted methods, all the signals of the dataset have been grouped by type and their mean has been removed. This means that *all* the O2Hb signals belonging to *all* subjects (HS and PT) tested under *every* condition have been grouped together and the same has been done for TOI and nTHI signals as well. Then, the fittings have been applied to 10 s of signal of each group and the corresponding average R^2 value has been computed. Hence, one mean R^2 value for each group of signals and for each tested method has been obtained, leading to twelve R^2 mean values in total. This procedure is summarized in the scheme in figure 3.2.1.
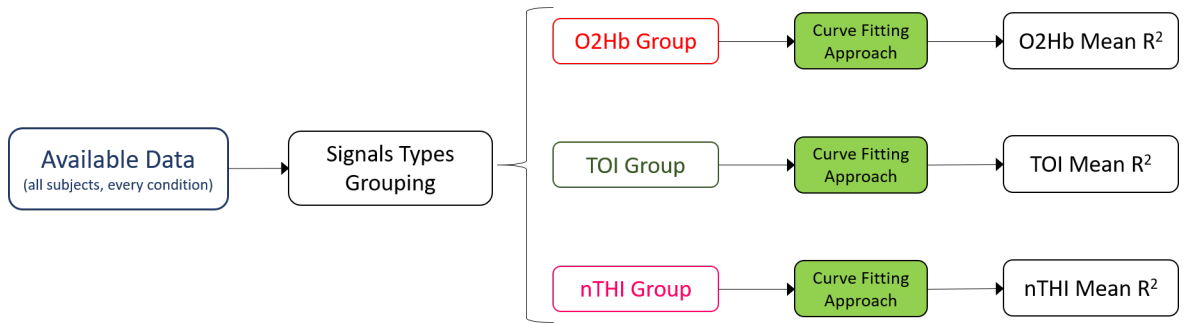
Figure 3.2.1: Scheme showing how the signals have been grouped before testing the fitting methods

Figure 3.2.2 shows the average coefficients of determination for each group of signals and for each tested method.
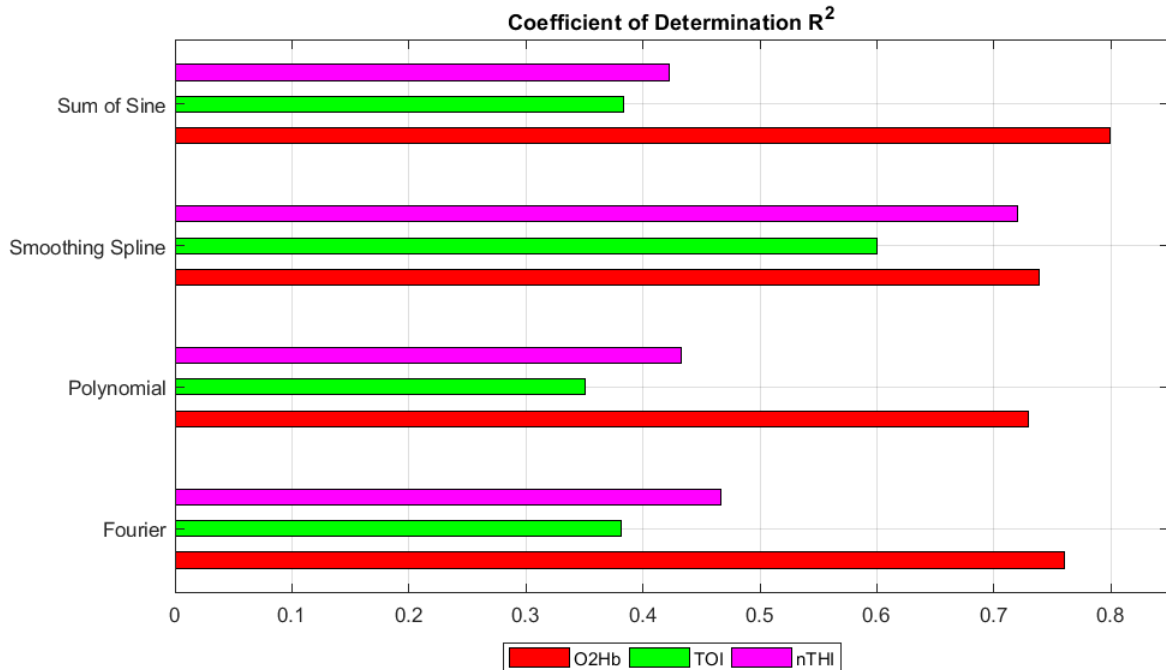
Figure 3.2.2: Comparison of the resulting average R^2 values from the tested fitting methods

While for O2Hb signals the mean R^2 value is larger for the sum of sine method, the smoothing spline fitting seems the best performing for TOI and nTHI signals when compared to the other approaches. Nevertheless, the low R^2 values shown for TOI and nTHI are due to the aforementioned purpose of the fitting, which is just the detection of the slow trend, excluding the other oscillations. On the other hand, the larger values shown for O2Hb are possibly due to the less noisy morphology of this kind of signal when compared to TOI and nTHI, meaning that its trend is overall easier to fit.

Anyway, as an example, figures 3.2.3 - 3.2.5 show the smoothing spline results in terms of slow trend detection and consequent signal detrending when applied to the O2Hb, TOI and nTHI signals from channel 1 of HS1 under BL condition.
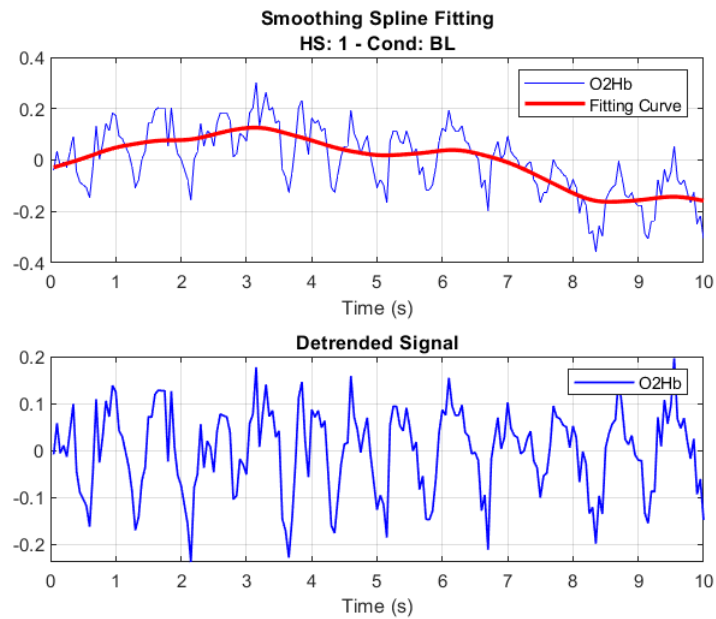
Figure 3.2.3: Example: result of the smoothing spline fitting method applied to O2Hb and corresponding detrended signal
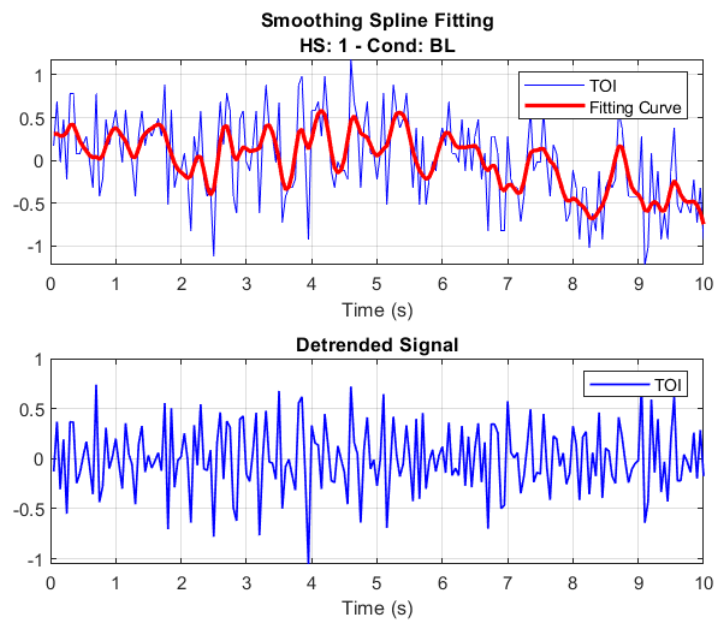
Figure 3.2.4: Example: result of the smoothing spline fitting method applied to TOI and corresponding detrended signal
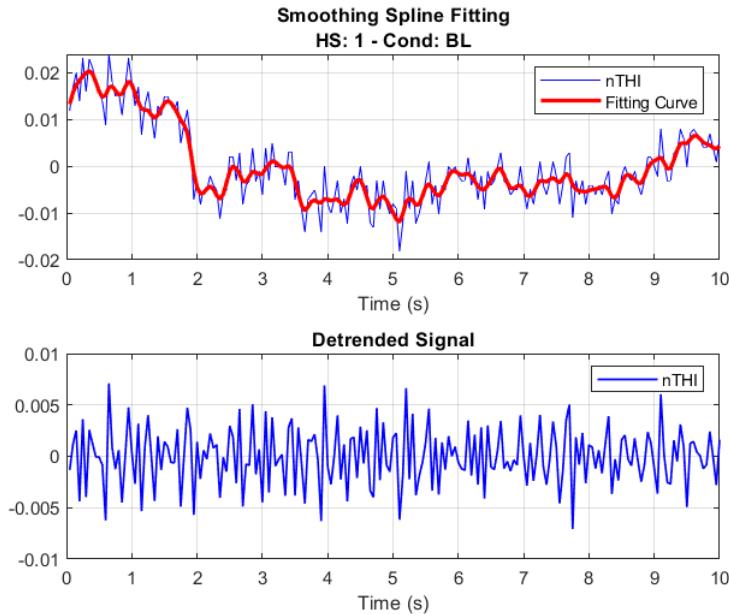
Figure 3.2.5: Example: result of the smoothing spline fitting method applied to nTHI and corresponding detrended signal

Although these results may be considered satisfying in terms of detrending quality, they are not exactly comparable to those obtained through the best performing filters reported in section 3.2, as shown in figure 3.2.6. Moreover, the main drawback of the curve fitting methods is related to their domain of application, that is the time domain. In the time domain, the quality of the trend fitting performed by these methods needs to be assessed especially visually and it is very signal-sensitive, meaning that the same method for one signal may not be as effective as it is for other signals. This is particularly true for the smoothing spline method, whose performance needs to be evaluated visually by setting an appropriate smoothing parameter which allows to increase or decrease the smoothness of the fitting curve according to the visualized signal. This procedure can be promptly done by visualizing the signal in the time domain but for this reason it cannot be effectively automated to deal with dozens of signals. In addition to that, the parameter selection is scarcely objective, thus without giving the same outcome every time.

Conversely, the main advantage of working in the frequency domain, as the filtering approach does, has the advantage of not dealing directly with the time morphology of the signals, but focusing on their spectra to cut off the frequencies responsible for the slow trend, hence operating in the same, objective way with every analyzed time series. Besides, the curve fitting methods are not able to cut off the high frequencies responsible for the noisy oscillations of the TOI and nTHI signals of interest, hence a BP filter should be further applied anyway.
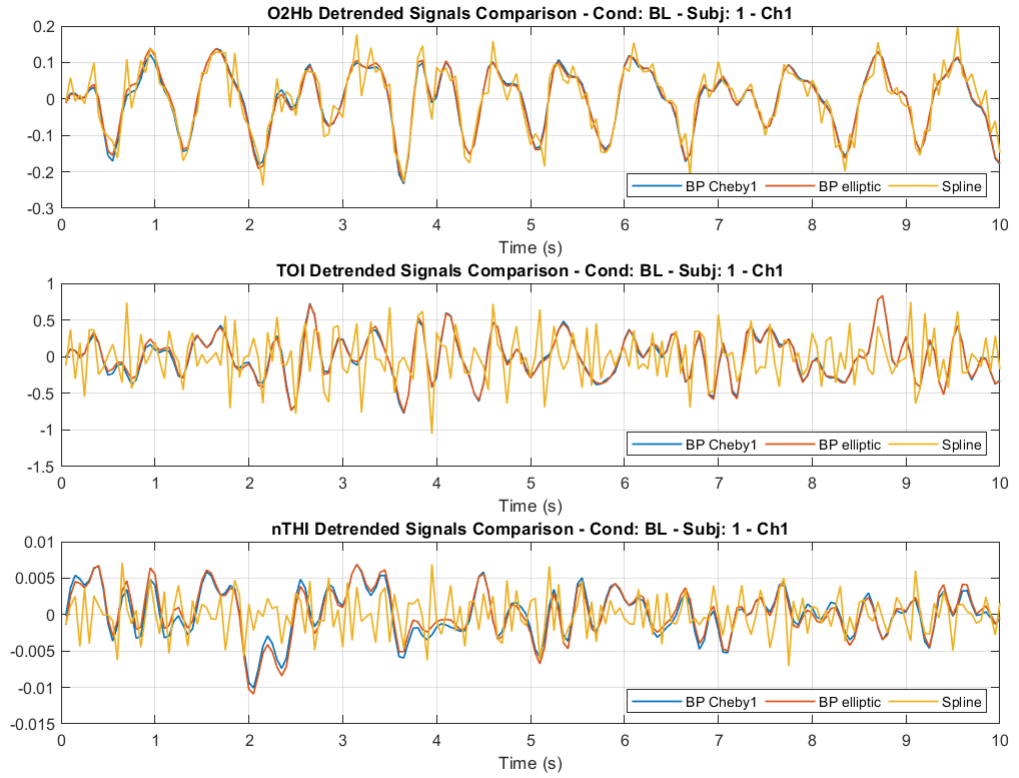
Figure 3.2.6: Results comparison among the best performing tested methods (channel 1, HS1 under BL condition)

3.3   Final Filter Selection

Ultimately, for the reasons discussed above and in spite of the clear closeness of the results given by the Chebyshev 1 and the elliptic BP filters (see figure 3.2.6), the latter has been selected as the proper filter required for this work. Besides, also other authors [25] report a similar use of an elliptic BP filter to detrend O2Hb signals (although sampled at a higher rate) which are next processed to extract the HBI.

Furthermore, to demonstrate the goodness of the selected BP elliptic filter in terms of signal spectral content, figures 3.3.1 and 3.3.2 show the power spectrum of the original and the detrended signals from HS1 under BL condition as an example. The power spectrum has been computed by using the Signal Analyzer MATLAB app.
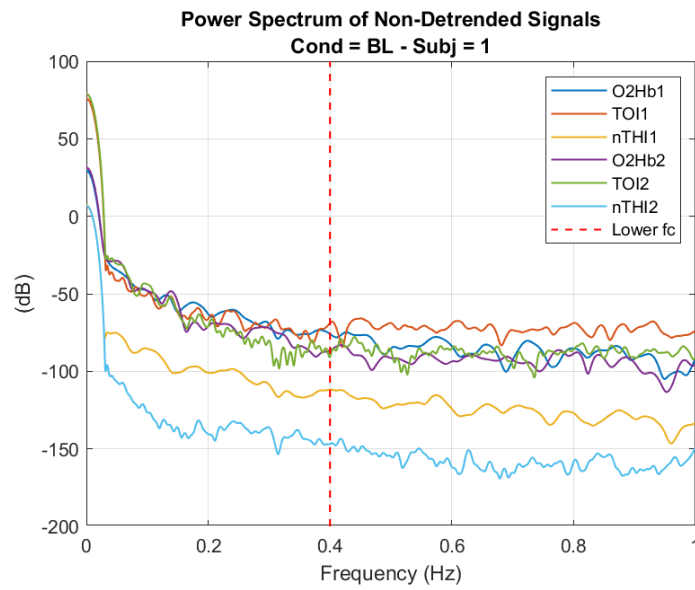
Figure 3.3.1: Example: power spectrum of the original signals from HS1 under BL condition (only low frequencies are shown)
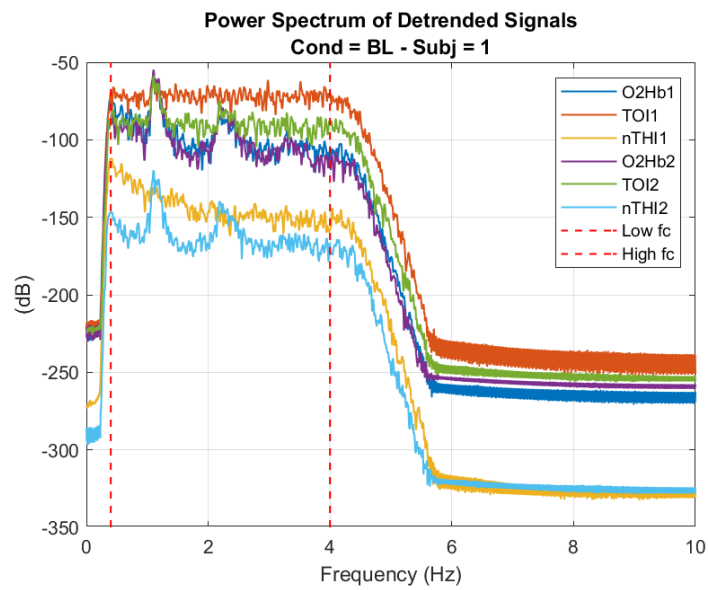
Figure 3.3.2: Example: power spectrum of the detrended signals from HS1 under BL condition

Chapter 4

Statistic and Correlation Analysis

In this chapter the statistic and correlation analysis performed on the dataset of the available detrended NIRS signals is described. The analysis consists in two main parts:

1. *statistic analysis* on the detrended signals;

2. *correlation analysis* between O2Hb and SRS signals (TOI and nTHI).

All the relevant results of this analysis are reported in the appendixes A - C.

4.1 Statistic Analysis

The statistic analysis performed on the detrended NIRS signals is divided into two parts:

1. statistic analysis on the *average* signals (AvgS);

2. statistic analysis on the *upper* and *lower* values with respect to the AvgS *median* (OTM: over the median and UTM: under the median values).

The first part of the analysis consisted in considering each type of signal from a specific channel of each subject and calculating the mean of the samples in the same location belonging to all the subjects tested under the same condition to obtain an *average* signal with reference to that specific condition. This procedure is recapped by the scheme in figure 4.1.1.
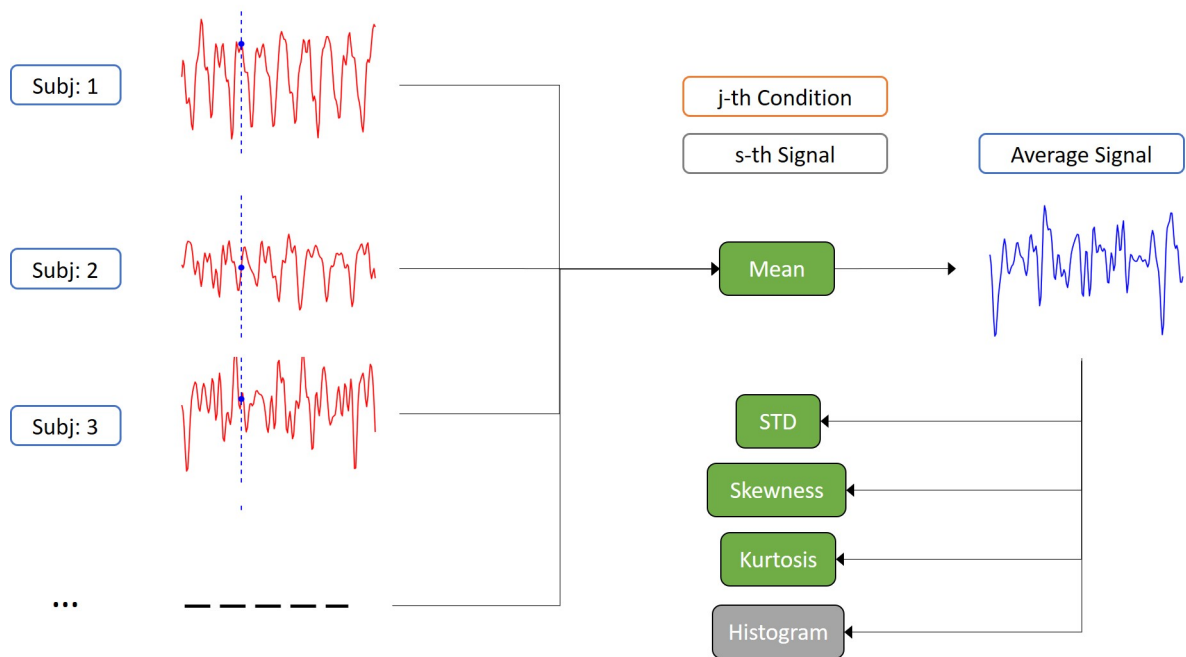
Figure 4.1.1: Scheme showing the steps of the calculation of the average signals from all the subjects tested under the same condition and the computation of the corresponding statistic information

As shown by the scheme in figure 4.1.1, considering for instance the s-th signal O2Hb1 and the AP condition, every signal sample in the same location belonging to every tested subject under this condition has been averaged to obtain only one average signal of that kind. Thus, the obtained average signal is comprehensive of the information contained in *all* the signals of the same type (e.g. O2Hb1) from *all* the subjects tested under that condition (e.g. AP). Next, the standard deviation (STD), skewness and kurtosis of the obtained average signals have been computed along with the signals samples histograms. The AvgS mean has not been computed as the average signals are obtained from detrended signals, whose mean has been removed and brought to zero after the filtering in the detrending process (see chapter 3). The results of this part of the statistic analysis can be found in appendix A. The main reason for this procedure is the aim of summarizing the statistical trends of all the subjects involved in the same condition through only one signal of each type (O2Hb and SRS), which is a synthesis of every subject outcome.

The second part of the analysis consisted in dividing the obtained AvgS into two blocks of samples with respect to their median, as shown in figure 4.1.2.
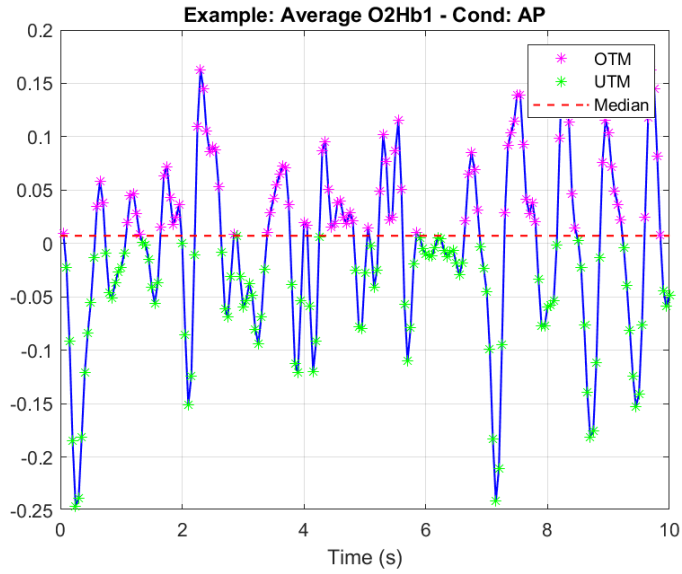
Figure 4.1.2: Example: average O2Hb1 signal from HS under the AP condition with the corresponding median, OTM and UTM values (only 10 s displayed)

Next, the mean, standard deviation, skewness and kurtosis of the obtained OTM and UTM values have been calculated: the results are available in appendix B.

As an example, the results corresponding to the groups of patients (PT) under every testing condition will be discussed here. Figures 4.1.3 - 4.1.8 show the histograms of the AvgS of this group of subjects under every testing condition. Overall, all the obtained probability distributions appear to be normal-looking at different levels. Specifically, with reference to the kurtosis values reported in table 4.1.1, O2Hb and nTHI signals seem to behave similarly by showing a more normal probability distribution during the Pre-CV condition (kurtosis closer to 3), while the distribution sharpens during the Post-CV condition (kurtosis larger than 3). Conversely, TOI signals do not seem to change their normal-like probability distribution when comparing the two conditions.
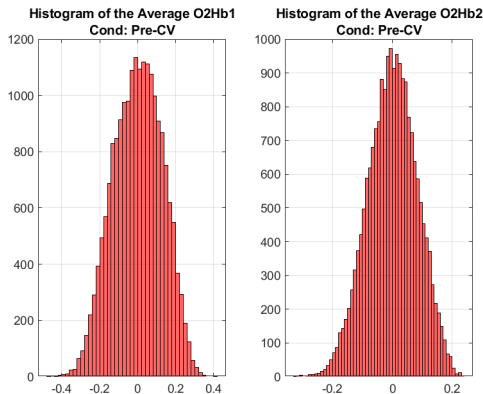
Figure 4.1.3
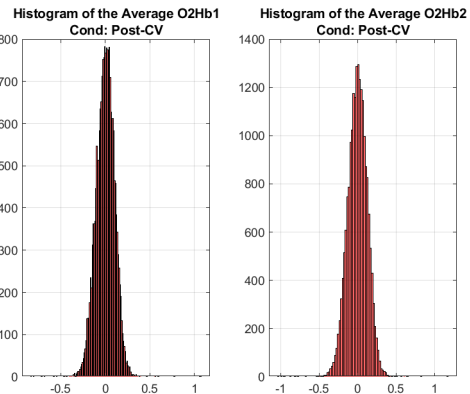
Figure 4.1.4
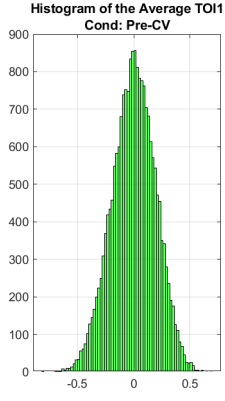
Figure 4.1.5
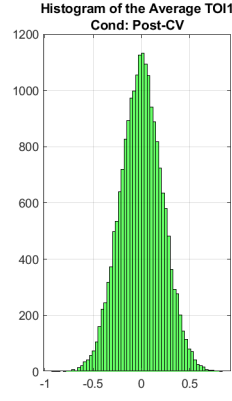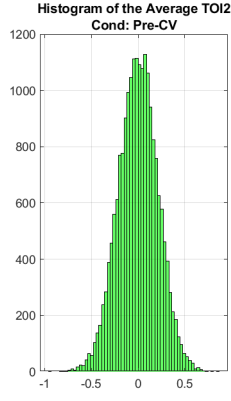
Figure 4.1.6
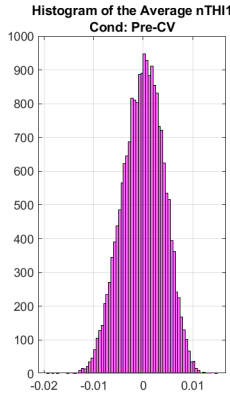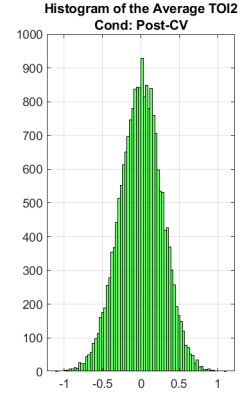
Figure 4.1.7
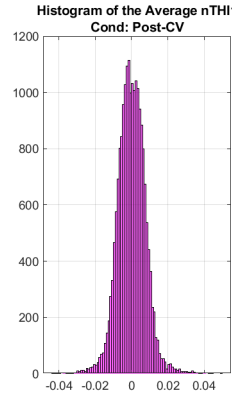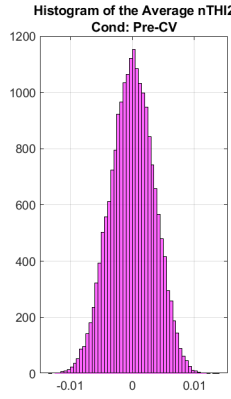
Figure 4.1.8
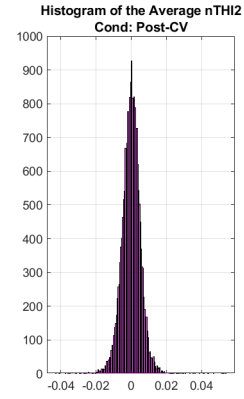
Table 4.1.1: STD, skewness and kurtosis of the AvgS obtained from all the PT under every testing condition

| Avg. Signals Statistics | Conditions | | | | | |
| | Pre-CV | | | Post-CV | | |
PT	STD	Skewness	Kurtosis	STD	Skewness	Kurtosis
O2Hb1	0.13	-0.12	2.52	0.10	-0.07	5.11
O2Hb2	0.08	-0.13	2.80	0.13	-0.11	4.69
TOI1	0.19	-0.10	2.89	0.22	0.00	3.03
TOI2	0.21	-0.05	3.06	0.28	-0.06	3.08
nTHI1	0.00	-0.15	2.76	0.01	0.14	5.19
nTHI2	0.00	-0.05	2.85	0.01	0.05	7.81

A common characteristics of all the AvgS obtained (from HS and PT), which can be seen in the complete set of results in the appendixes A and B, is the tendency to show a normal-like probability distribution with different levels of STD, skewness and kurtosis. However, overall it can be observed how most of the obtained distributions are not particularly skewed, hence showing almost coincident median and mean values. A confirmation of these results has been searched in the second part of the statistic analysis, involving the division of each AvgS into OTM and UTM values. In fact, as median and mean are mostly coincident and equal to zero, this is approximately equivalent to dividing the signal into the same number of positive and negative values. As the probability distributions are mostly symmetric, this leads to homogeneous signal amplitudes for positive and negative values, as confirmed by the results concerning the OTM and UTM values. As an example, tables 4.1.2 and 4.1.3 contain the results of the satistic measures on the OTM and UTM values extracted from the AvgS of the PT. It must be noticed that the mean concerning the OTM and the UTM values of the nTHI signals shown in tables 4.1.2 and 4.1.3 is either null or almost equal to zero since generally the detrended nTHI signals do not reach large amplitudes and all the values reported here have been rounded to two digits to the right of the decimal point.

Table 4.1.2: Mean, STD, skewness and kurtosis of the OTM values from the AvgS of every PT under every condition

OTM Statistics - PT	Conditions	
Avg. Signals	Pre-CV	Post-CV
Mean O2Hb1	0.11	0.08
O2Hb2	0.07	0.10
TOI1	0.15	0.17
TOI2	0.17	0.22
nTHI1	0.00	0.01
nTHI2	0.00	0.00

OTM Statistics - PT	Conditions	
Avg. Signals	Pre-CV	Post-CV
Skewness O2Hb1	0.61	2.08
O2Hb2	0.73	1.70
TOI1	0.86	1.01
TOI2	1.02	1.02
nTHI1	0.80	2.15
nTHI2	0.87	2.98

OTM Statistics - PT	Conditions	
Avg. Signals	Pre-CV	Post-CV
STD O2Hb1	0.07	0.06
O2Hb2	0.05	0.07
TOI1	0.11	0.13
TOI2	0.13	0.17
nTHI1	0.00	0.01
nTHI2	0.00	0.00

OTM Statistics - PT	Conditions	
Avg. Signals	Pre-CV	Post-CV
Kurtosis O2Hb1	2.73	20.41
O2Hb2	2.87	14.10
TOI1	3.43	3.90
TOI2	3.97	3.99
nTHI1	3.26	11.08
nTHI2	3.45	24.89

Table 4.1.3: Mean, STD, skewness and kurtosis of the UTM values from the AvgS of every PT under every condition

UTM Statistics - PT		Conditions	
	Avg. Signals	Pre-CV	Post-CV
Mean	**O2Hb1**	-0.11	-0.08
	O2Hb2	-0.07	-0.10
	TOI1	-0.15	-0.17
	TOI2	-0.17	-0.22
	nTHI1	0.00	-0.01
	nTHI2	0.00	0.00

UTM Statistics - PT		Conditions	
	Avg. Signals	Pre-CV	Post-CV
Skewness	**O2Hb1**	-0.75	-1.51
	O2Hb2	-0.97	-1.59
	TOI1	-0.96	-1.00
	TOI2	-1.06	-1.05
	nTHI1	-0.87	-1.86
	nTHI2	-0.92	-2.22

UTM Statistics - PT		Conditions	
	Avg. Signals	Pre-CV	Post-CV
STD	**O2Hb1**	0.08	0.07
	O2Hb2	0.05	0.08
	TOI1	0.12	0.13
	TOI2	0.13	0.17
	nTHI1	0.00	0.00
	nTHI2	0.00	0.00

UTM Statistics - PT		Conditions	
	Avg. Signals	Pre-CV	Post-CV
Kurtosis	**O2Hb1**	3.18	9.11
	O2Hb2	3.77	10.23
	TOI1	3.63	3.95
	TOI2	4.14	4.01
	nTHI1	3.51	8.98
	nTHI2	3.58	13.18

4.2 Correlation Analysis

As already discussed in the previous chapters, the signals obtained from the tested subjects through the NIRO-200NX NIRS monitor can be classified in two main categories:

- signals obtained by the application of the MLBL (O2Hb and HHb): LB signals;

- signals obtained by the application of the SRS algorithm (TOI and nTHI): SRS signals.

As already mentioned in chapter 1, some authors [23] marked a closer relation of the LB signals to the extracerebral circulation than to the intracranial circulation under some cirsumstances, meaning that the HBI detection merely based on this kind of signal may not exactly reflect the hemodynamic changes occurring at a cortical level. As the aim of this work is detecting the HBI from the deeper blood circulation involving the cerebral cortex, the LB signals should not be used. The SRS signals instead appear to better reflect the intracranial circulation, hence they will be used to extract the heartbeat information.

However, as already mentioned, the main drawback of the SRS signals is that they often look way noisier than the LB signals, making the HBI detection more difficult. This issue will be addressed in chapter 5.

In this context, a correlation analysis has been performed between the Lambert-Beer signals (O2Hb) and the SRS signals (TOI and nTHI) to investigate how the two kinds of signals are related. As shown in chapter 5, this analysis may provide useful information for a further signal processing involving both the LB and the SRS signals with the aim to extract the HBI information from the supposedly deeper SRS signals by relying on their hypothetical correlation with the shallower LB signals.

First, the linear dependence between the two kinds of signals has been investigated by computing the Pearson correlation coefficient (ρ_{AB}) between the two signals, which is one of the most common measures of correlation between two random variables, defined as:

$$\rho_{AB} = \frac{\sigma_{AB}}{\sigma_A \sigma_B} \tag{4.2.1}$$

where σ_{AB} is the covariance between the two random variables A and B, while σ_A and σ_B are the standard deviations of A and B respectively. ρ_{AB} can range from -1 (A and B totally negatively correlated) to 1 (A and B totally positively correlated). In this case the two couples of examined signals will be O2Hb-TOI and O2Hb-nTHI from both acquisition channels of every tested subject.

Furthermore, the correlation between the LB and the SRS signals has been evaluated by time shifting the two kinds of signals and calculating the Pearson coefficient at every time delay. To do that, the signals have been shifted at steps equal to their sampling interval (0.05 s) and up to 4 s of maximum delay. Hence, for each lag between the two signals, the Pearson coefficient has been computed.

All the results concerning the Pearson coefficient calculation and the correlation with delay between the two signals can be found in appendix C.

About the results of the correlation between the delayed signals, there are many differences in the behavior of each subject under the same condition (see appendix C). The

correlations obtained are not necessarily positive: there are also some negative correlations, indicating a likely phase opposition of the two signals. Anyway, there are subjects (both HS and PT) showing particularly large correlations (up to 0.97 and -0.89) under certain circumstances, showing a tight relation between the LB and SRS signals. On the other hand, there are also subjects showing very low correlations (up to 0.01 and -0.02). It must be noticed that there have been technical issues determining anomalous behaviors for some subjects, as mentioned in chapter 2, and as this will be further discussed in chapter 5. However, those exhibiting the best correlation are also the subjects who already showed the clearest SRS signals during their acquisition. In the next chapter these particular cases will be further discussed as well.

As an example, figures 4.2.1 - 4.2.4 here report the Pearson coefficients obtained on the PT signals under both the Pre-CV and Post-CV condition, along with an example of the resulting coefficient trend on the time shifted signals (figures 4.2.5 and 4.2.6).
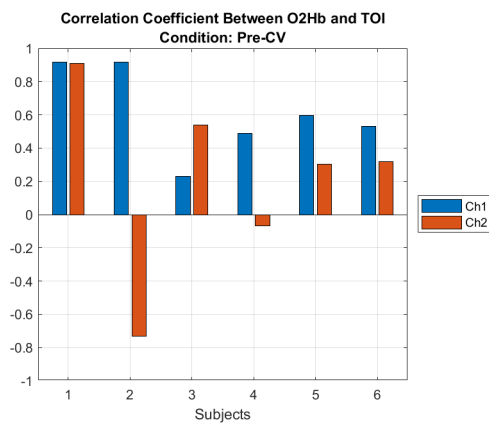
Figure 4.2.1
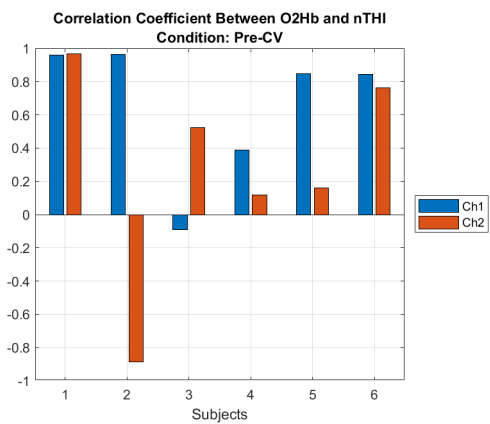
Figure 4.2.2
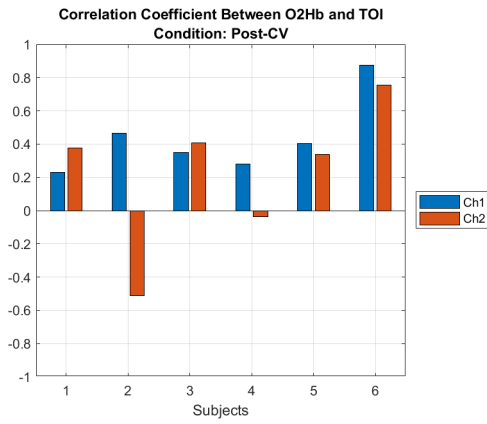
Figure 4.2.3
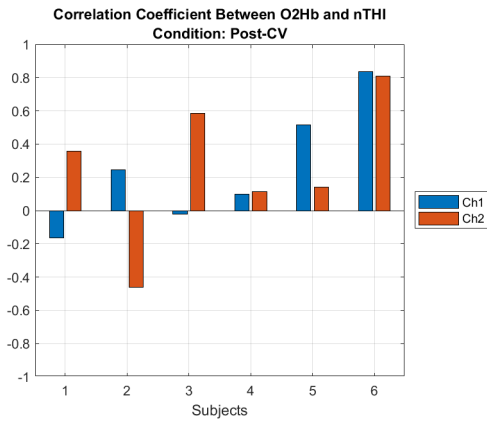
Figure 4.2.4
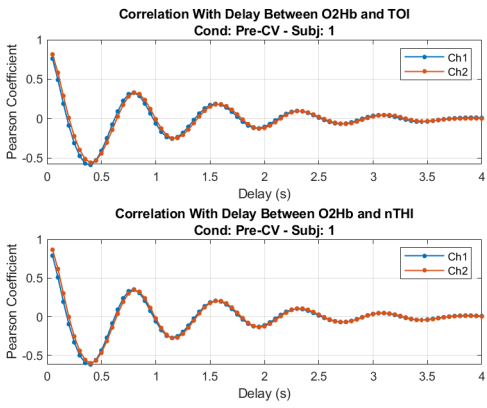
Figure 4.2.5

Figure 4.2.6

57
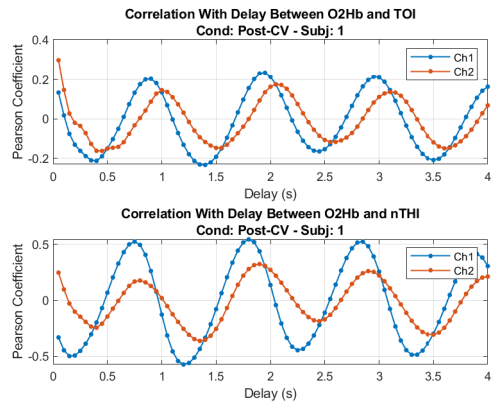
Chapter 5

Heartbeat Intervals Extraction

After the detrending procedure accomplished by adopting an elliptic BP filter with the features specified in chapter 3 section 3.1, all the available NIRS signals have been processed for further heartbeat intervals (HBI) extraction. Furthermore, as a validation mean, the available ECG signals have been processed to extract the HR and HBI values to compare with those obtained from the NIRS signals of the same patients (see section 5.5).

In chapter 4 the correlation between the LB and SRS signals has been explored. Here, the aim of the following processing is to use the correlation between these two kinds of signals to effectively extract the HBI information of interest. In fact, as already discussed in chapter 1 section 1.4, the main concern about the use of the O2Hb signals for HBI extraction is the influence by the extracranial circulation which may involve the LB signals while, under some circumstances, the SRS signals do not seem to be concerned. However, in most cases, SRS signals cannot be promptly used for HBI extraction either, as they appear to be very noisy and to "hide" the beat-to-beat information. In fact, the HBI extraction is based on the peak-to-peak distance computed on the signal of interest and, if the signal is too noisy, no clear peak can be identified.

For this reason, a SRS signals denoising method, based on the relation with the LB signals, is described in this chapter.

This method consists in three main steps:

1. O2Hb power spectral density (PSD) estimate computation;

2. narrow BP filter design around the main O2Hb PSD frequency detected;

3. application of the designed filter to the corresponding SRS signals.

The scheme in figure 5.0.1 recaps the procedure followed in the signal processing described in this chapter.
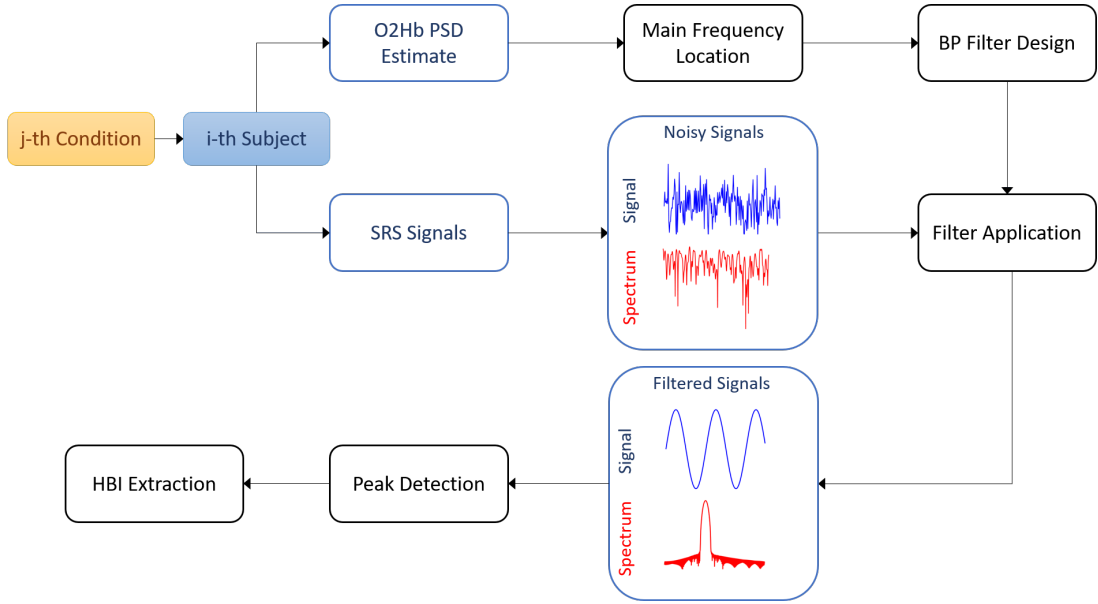
Figure 5.0.1: Scheme recapping the steps of the signal processing performed

All the PSD estimates introduced in this processing were computed by adopting the Welch periodogram MATLAB function with default options in terms of choice of the signal window (the Hamming window is used), windows overlap (50%) and number of points for the PSD representation.

As an example, in this chapter only the results concerning PT3 will be reported. All the relevant results of this processing regarding every tested subject (HS and PT) under every testing condition are collected in the appendixes D and E.

5.1 O2Hb PSD Estimate

The PSDs of all the O2Hb signals have been estimated. For each O2Hb PSD, the frequency corresponding to the PSD maximum has been located. In fact, as O2Hb signals appear more quasi-periodic than the SRS signals, their PSD generally shows a maximum around a certain frequency, which should be the main oscillation frequency of the signal and hence the frequency related to the hypothetical HBI values.

As a consequence, that frequency is considered as the central frequency of the narrow BP filter that should be designed and then applied to the corresponding SRS signals.

In fact, SRS signals PSD generally do not show a proper prominent maximum around a specific frequency as these signals are generally noisier and hence they look less quasi-periodic than the O2Hb signals.

Figures 5.1.1 - 5.1.6 show the resulting O2Hb estimate from both channels of PT3 and the distribution of the PSD maxima locations from both channels of *all* subjects (HS and PT) under every condition.
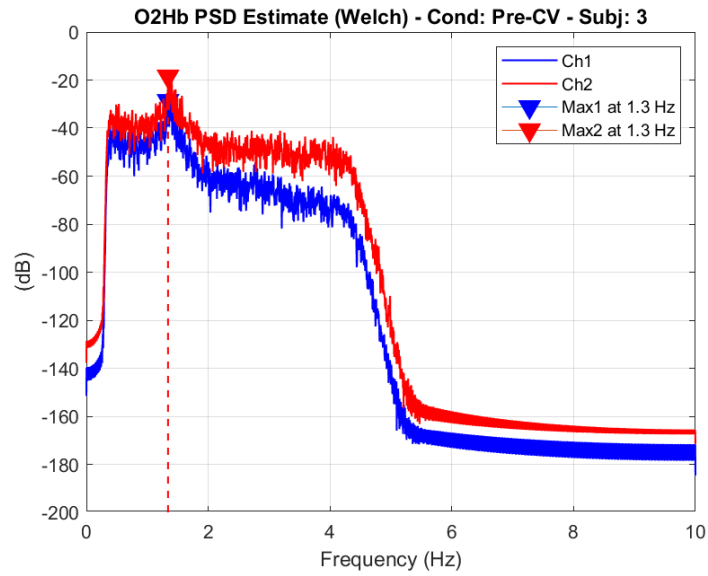
Figure 5.1.1: PSD estimate of the O2Hb signals from PT3 before the CV
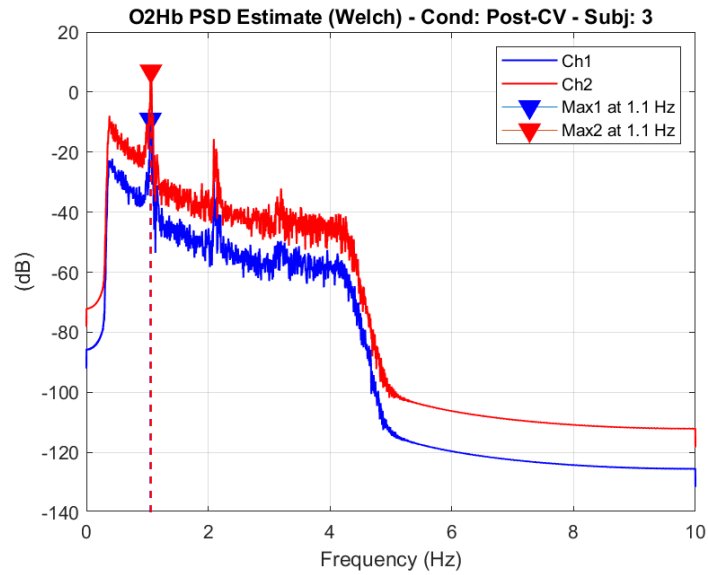
Figure 5.1.2: PSD estimate of the O2Hb signals from PT3 after the CV
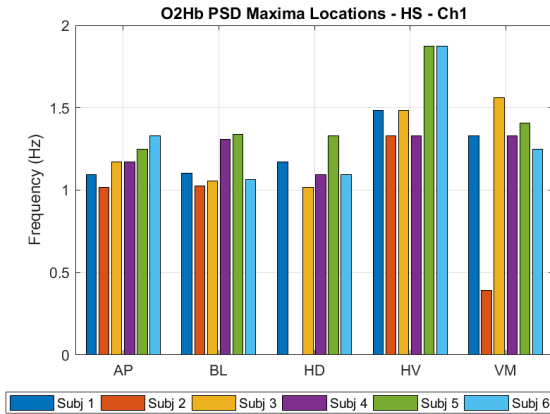
Figure 5.1.3
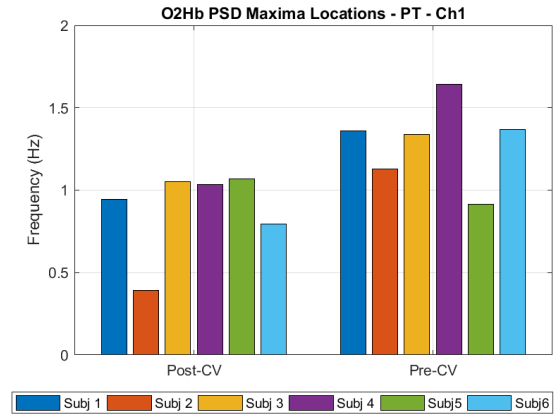
Figure 5.1.5
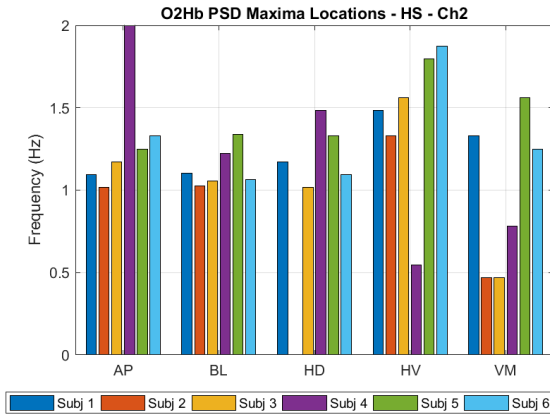
Figure 5.1.4
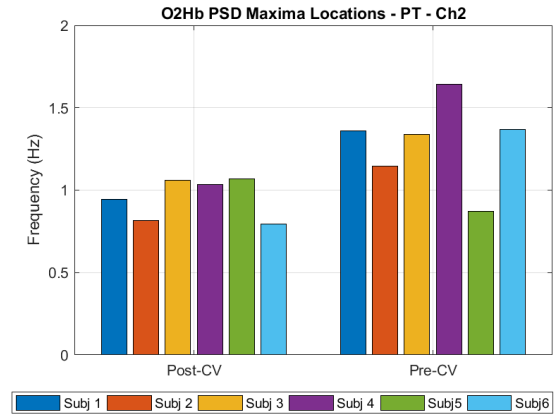
Figure 5.1.6

With reference to figures 5.1.1 and 5.1.2, as expected, the main frequency is shifted from a higher value *before* the CV to a lower value *after* the CV. In fact, as the cardioversion could restore the NSR of the patient, the frequency supposedly related to the HBI information should decrease accordingly, as the HR of the patient is reduced by the CV.

Meanwhile, figures 5.1.3 - 5.1.6 offer a broader evaluation of the O2Hb main frequency behavior. Looking at the PT results, the same behavior observed for PT3 is confirmed by other patients: although at different levels, almost every subject reveals decreasing O2Hb main frequency values when proceeding from the Pre-CV to the Post-CV condition. However, PT5 seems to behave conversely. This might be due to the presence of casual longer RR intervals on the ECG, which have been observed also on the SRS signals mainly

as momentary dips showing a sudden lack of deep oxygenation (see figures 5.1.7 and 5.1.8)[1]. These sporadic longer RR intervals have been observed both during the Pre-CV and the Post-CV condition, affecting both the HR mean values and the HBI extraction from the NIRS and the ECG signals of this patient (see the corresponding results in appendix D.2).
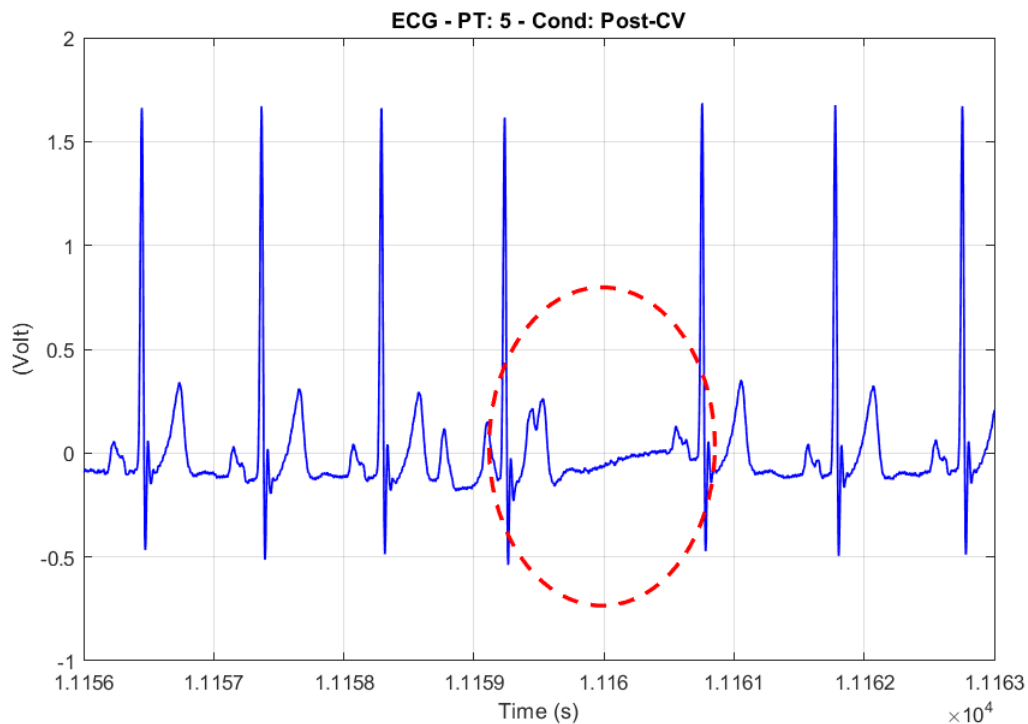
Figure 5.1.7: Example: longer RR interval detected on PT5

---

[1]The time axis represented in these two examples are arbitrary and do not match as the two kinds of signals have not been acquired in sync by the same system, as described in chapter 2. However they both refer to the same time interval which has been isolated by referring to the corresponding time of the day of the acquisition.
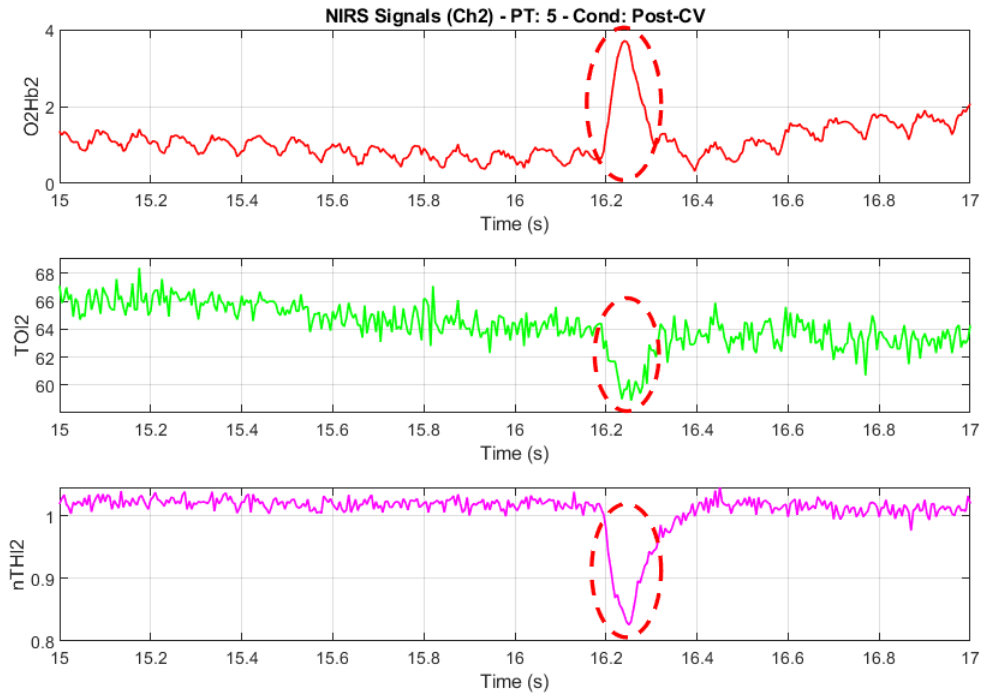
Figure 5.1.8: Example: dips in the SRS signals corresponding to the longer RR interval

Also channel 1 of PT2 under Post-CV condition shows an odd behavior (see figure 5.1.5). In fact, the maximum O2Hb frequency detected appears to be quite low compared to the other subjects under the same condition. This is also clear in the O2Hb PSD estimate shown in figure 5.1.9, where channel 1 shows and unlikely main frequency value (0.4 Hz). It should be reported that the band covering the NIRS optodes on this patient's forehead has been loosened a bit before the CV took place. Basically, the band used on the patients had two purposes: properly covering the optodes to further shield them from the environmental light and contributing to their adhesion on the skin along with the adopted biomedical adhesive stripes. As a consequence, an excessive loosening of the band may cause a signal corruption to some extent for two reasons: one related to some disturbing light reaching the detectors and one related to a scarce skin-optode adhesion. It is unclear what caused this odd O2Hb PSD estimate as the detrended NIRS signals from channel 1 of PT2 under Post-CV do not show particular differences from the others except some spikes on the O2Hb signal, which may be due to external light interference more than to motion artifacts, as the patient was still under some anesthetic effect right after the CV. Surely, this issue affected all the consequent processing and the final HBI and HR values (see appendix D.2).

Considering the HS results, the issues mentioned in chapter 2 concerning channel 2 of subject 4 are responsible for the unexpected results shown in figure 5.1.4, where, for instance, during the AP condition O2Hb shows an unlikely high main frequency. As already discussed previously, this subject's results cannot be considered reliable because of the

encountered technical issues.

Overall, for both the HS and the PT, it seems that the results in terms of O2Hb main frequency are mostly coherent between channel 1 and 2.
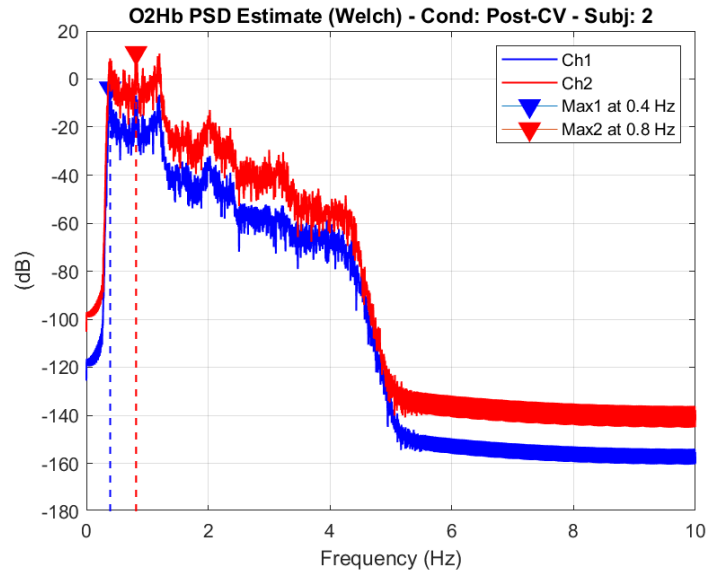
Figure 5.1.9: Peculiar result: PSD estimate of the O2Hb signals from PT2 after the CV

5.2   Narrow BP Filter Design

After locating the main frequencies from the computed O2Hb PSD estimates, the following step consisted in designing a properly narrow BP filter around those frequencies to denoise the corresponding SRS signals.

The critical parameter to set is the pass-band width of the desired filter. While an excessively wide band would include more original signal information, it would not properly denoise the signal, as all the disturbing high frequencies responsible for hiding the HBI content would still be there. On the other hand, an excessively narrow band would cut off too many frequencies causing a dramatic reduction of the signal information and a large smoothing effect, which may cause in some cases a great amplitude reduction of some pieces of the original signal and thus a more difficult HBI extraction as the peaks would almost disappear.

After performing some trials, a final filter configuration in terms of pass-band width has been selected and the filter parameters adopted are reported in table 5.2.1, where a hypothetical filter centered around a main frequency equal to 1 Hz is considered as an example. Because of the good results in terms of stop-band attenuation steepness and global filter performance previously obtained for the detrending process described in chapter 3, here a BP elliptic filter was used as well. Besides, also in this processing, the signals have been forward and backward filtered.

Table 5.2.1: Narrow BP elliptic filter parameters

BP Elliptic Filter		
Order	n	5
Stopband Attenuation	R_s	25 dB
Ripple Amplitude	R_p	0.025 dB
Cut-off Frequencies	f_c	[0.75, 1.25] Hz
Passband Mid-bandwidth	δ	0.25 Hz

The corresponding transfer function (TF) is shown in figure 5.2.1.
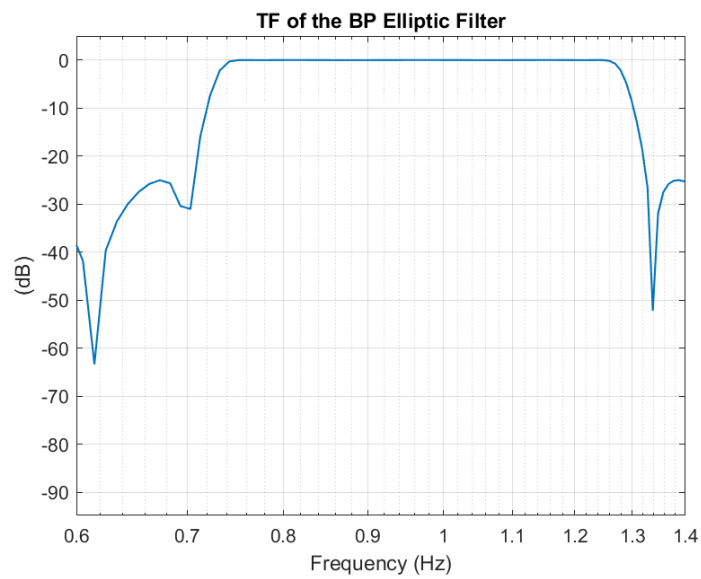
Figure 5.2.1: TF of the narrow BP elliptic filter shown as an example

5.3 Application of the Narrow BP Filter to the SRS Signals

The filter designed as described in section 5.2 has been then applied to the SRS signals corresponding to the O2Hb signals from which the main frequencies have been extracted.

Figures 5.3.1 - 5.3.4 show the resulting TOI and nTHI filtered signals from PT3 compared to their original versions (only 30 s are displayed). To compare the signals on the same diagram, both the original and the filtered version have been normalized by their maximum and centered around -1 and 1 respectively.
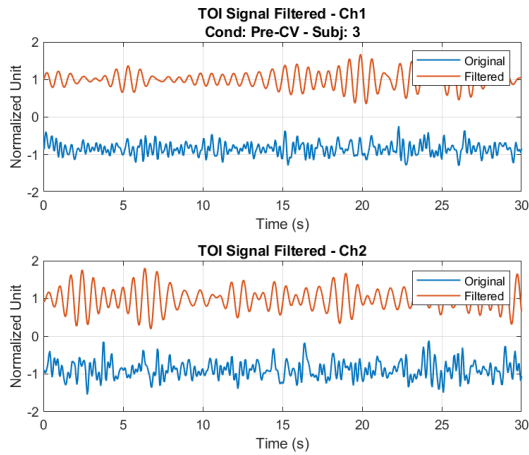
Figure 5.3.1
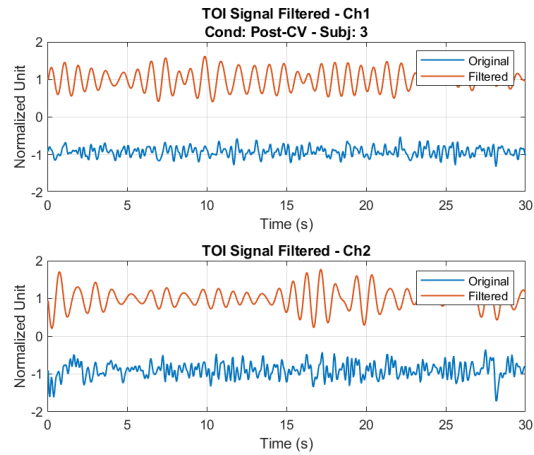
Figure 5.3.2
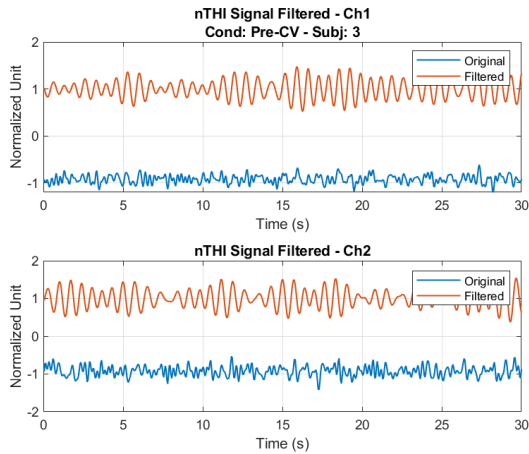
Figure 5.3.3
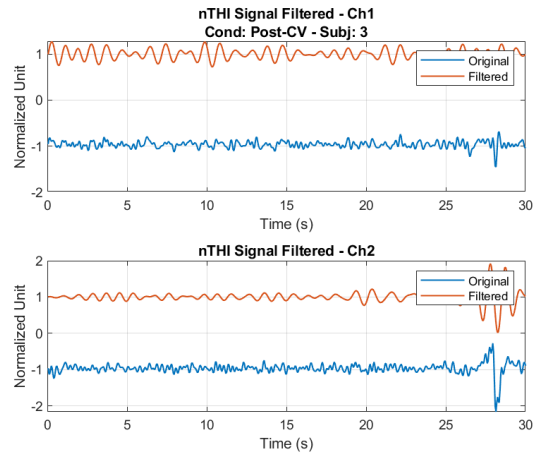
Figure 5.3.4

The resulting SRS signals PSD estimates after the filtering are shown in figures 5.3.5 - 5.3.8.
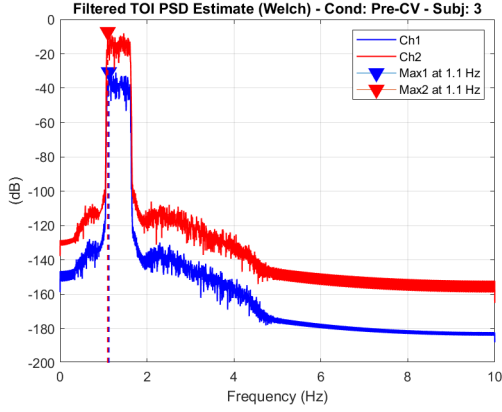
Figure 5.3.5
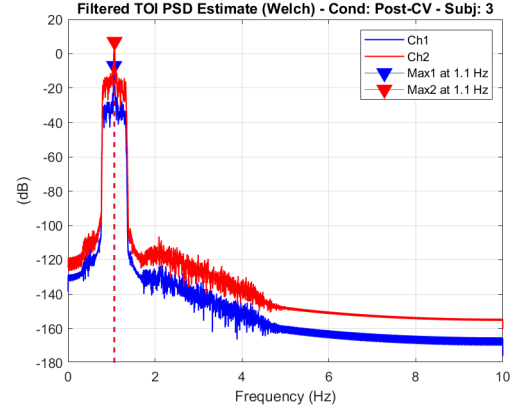
Figure 5.3.6
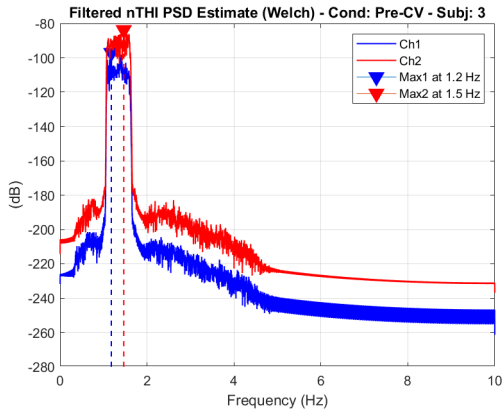
Figure 5.3.7
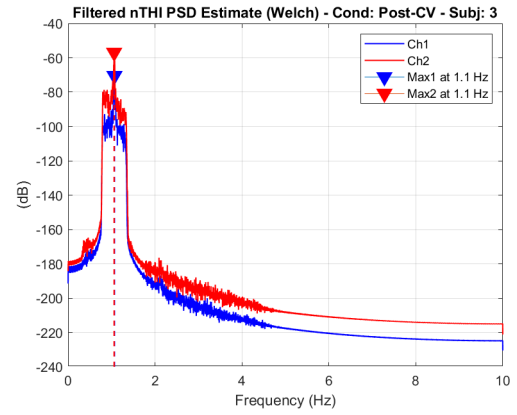
Figure 5.3.8

Stressing once more the fact that the choice of the pass-band width of the adopted filter is crucial for the good performance and results of this method, the maximum frequencies marked in figures 5.3.5 - 5.3.8 are not equal to those obtained on the corresponding O2Hb PSDs because the aim here was to narrow down the disturbing frequencies outside a particular range, whose central frequency had to be the main O2Hb frequency. Hence, the maxima reported on the TOI and nTHI PSDs are only indicative and do not have a real importance here since the real matter is the change occurred in these signals spectral content in terms of excluded frequencies rather than their maxima locations. In fact, *this* is the change causing the denoising of these signals. Moreover, as already discussed in the previous section, a tighter filter around the O2Hb main frequency may lead to an excessive loss of SRS signals information, thus reducing the ability to extract the HBI effectively.

68

5.3.1   Noisy SRS Signals: Special Cases

A relevant observation should be reported at this point. Beside the example case of the PT3 reported here, there have been cases (of both HS and PT), showing very clear TOI and especially nTHI signals during the acquisitions. Specifically, some subjects, under all their testing conditions, exhibit clear beat-to-beat information *already* in the original SRS signals which then appear almost as quasi-periodic as the corresponding O2Hb signals. An example of this particular phenomenon is shown in figure 5.3.9. The reason for this casual behavior is not much clear yet. Among the PT, some subjects exhibited this feature during the Pre-CV condition, after being administered an anesthetic in a previous exam. In fact, according to table 2.2.1 in chapter 2 section 2.2, these patients underwent a TEE before the CV and hence they already had been administered an anesthetic (Midazolam) during that exam. It is not completely sure if some residual anesthetic effect on these patients may have been responsible for this behavior. Anyway, the supposed relation between these two aspects should be further investigated. However, similar SRS signals behaviors were also observed in some patients who did not undergo a TEE and on one healthy subject as well (HS6). Furthermore, there has also been one patient (PT4) who underwent a TEE without showing any of these features and another one (PT5) undergoing a TEE but without showing them as much clearly as the others. If a likely reason for this behavior could be found, surely the SRS signals filtering performance could be greatly advantaged. In fact, it is understandable how original clearer SRS signals are easier to filter and make the filtering process less prone to undesired outcomes. As a confirmation, figures E.2.1 and E.2.13 show the resulting filtering of the same SRS signals reported in figure 5.3.9.
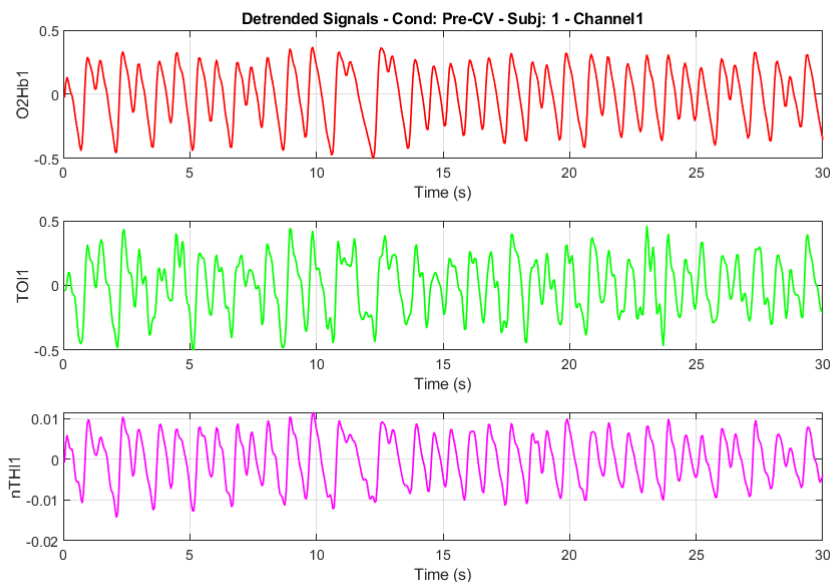
Figure 5.3.9: Example: clear TOI and especially nTHI signals on PT1, channel 1, before the CV (only 30 s displayed). Here, the correspondence between nTHI and O2Hb signals is incredibly clear.

5.4   Peak Detection and HBI Extraction

After filtering the SRS signals as shown in figures 5.3.1 - 5.3.4, the peaks indicating the beat-to-beat information are smoother and clearly visible. Hence, the peaks have been detected to compute the inter-peaks distance which is equal to the searched HBI values.

As an example, figures 5.4.1 and 5.4.2 show the resulting peak detection on the TOI and nTHI filtered signals from PT3 under Pre-CV condition (only 30 s are displayed).
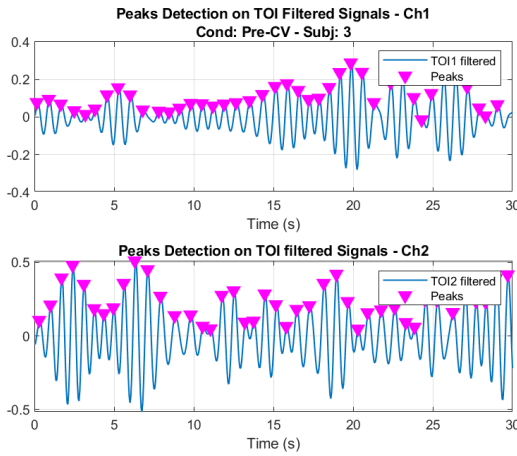
Figure 5.4.1
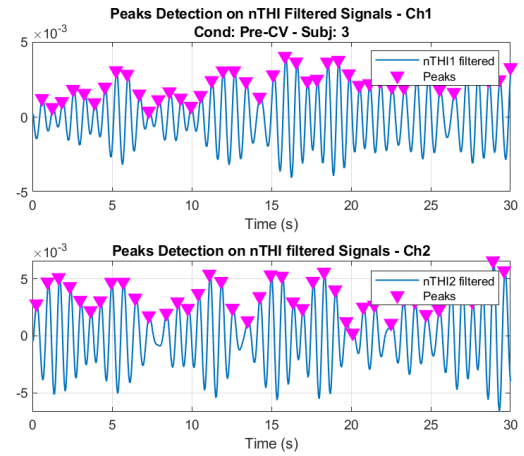
Figure 5.4.2

5.5   Comparison Between NIRS and ECG-related HBI Extracted from the Patients

Lastly, the HBI values have been computed by simply calculating the time distance between each detected peak on the filtered SRS signals.

In addition to that, for those subjects whose ECG signal was available, the HBI values extracted from their SRS signals were compared with those extracted from their ECG. This means that, to some extent, on these patients the HBI values from the ECG have been used to validate those obtained from the NIRS signals.

The histograms in figures 5.5.1 - 5.5.6 show the probability distribution of the HBI extracted from the PT3 NIRS and ECG signals, while tables 5.5.1 and 5.5.2 report the mean (μ) and standard deviation (σ) of the HBI and the corresponding HR values. The main details of the adopted HBI extraction procedure from the ECG signals are included in section 5.5.1.
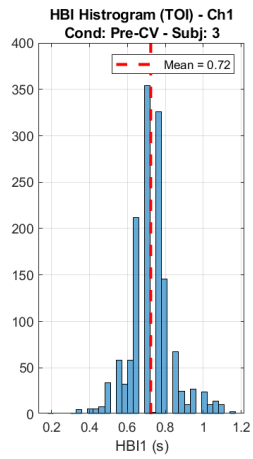
Figure 5.5.1
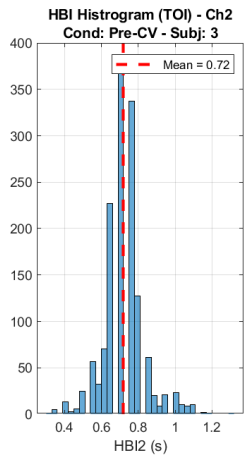
Figure 5.5.3
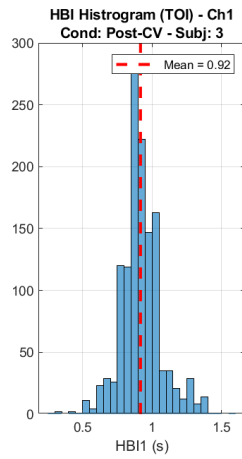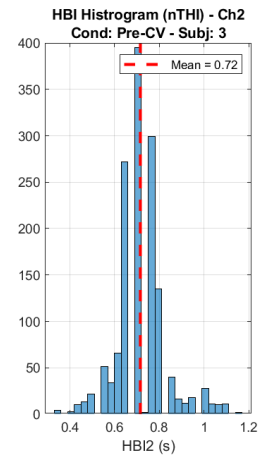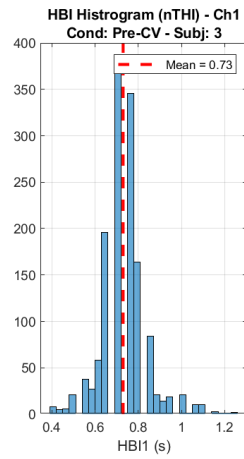
Figure 5.5.2
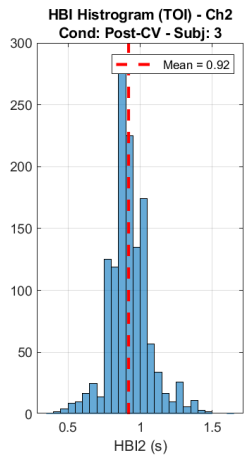
Figure 5.5.4
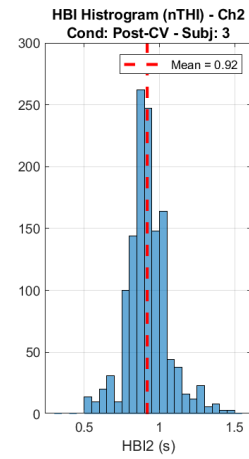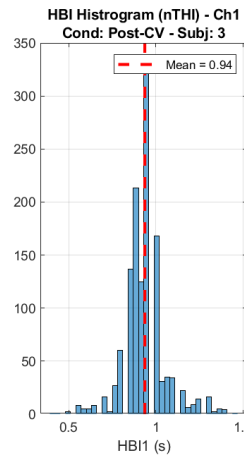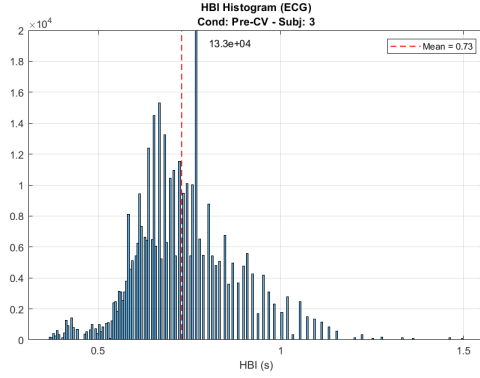
Figure 5.5.5
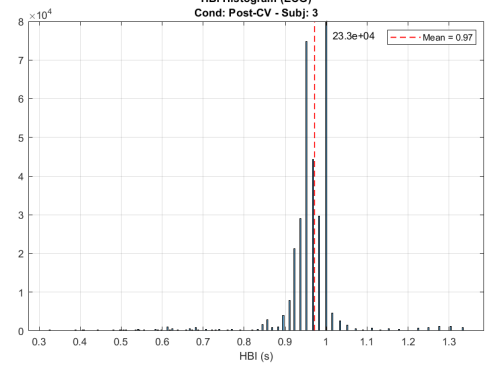
Figure 5.5.6

Table 5.5.1: Mean and standard deviation of the HBI extracted from the NIRS and ECG signals (PT3)

HBI (s) - PT3	Conditions							
	Pre-CV				Post-CV			
	μ_1	μ_2	σ_1	σ_2	μ_1	μ_2	σ_1	σ_2
TOI	0.72	0.72	0.12	0.11	0.92	0.92	0.15	0.14
nTHI	0.73	0.72	0.11	0.11	0.94	0.92	0.12	0.14
	μ		σ		μ		σ	
ECG	0.73		0.12		0.97		0.07	

Table 5.5.2: Mean and standard deviation of the HR computed from the HBI extracted from the NIRS and ECG signals (PT3)

HR (bpm) - PT3	Conditions							
	Pre-CV				Post-CV			
	μ_1	μ_2	σ_1	σ_2	μ_1	μ_2	σ_1	σ_2
TOI	85	86	16.0	14.9	67	67	12.4	11.8
nTHI	84	86	12.9	13.9	65	67	9.3	11.5
	μ		σ		μ		σ	
ECG	85		15.2		62		8.4	

To improve the visualization of the ECG-related HBI histograms in figures 5.5.5 and 5.5.6, the vertical axis range has been reduced so that the probability distributions could

be distinguished more clearly and their maxima have been simply marked by placing their corresponding value next to their bin.

With reference to tables 5.5.1 and 5.5.2, it seems that the HBI extracted from the NIRS signals are in agreement with those obtained from the ECG signal and the corresponding HR values behave accordingly. This is clear in terms of mean but some level of agreement in terms of standard deviation can be seen as well. Lastly, the expected increase of HBI duration along with the decrease of HR after the NSR restoration is seen on both the NIRS-related and the ECG-related values.

5.5.1   HBI Extraction from the Available ECG Signals

The adopted HBI extraction procedure from the ECG signals is synthesized in the scheme in figure 5.5.7. Basically, the scheme reports a QRS detection algorithm which references [26], [27] and has been implemented on MATLAB Simulink model. The QRS detector described here allows to detect the R-peaks on a ECG time series once the input signals has been properly processed.
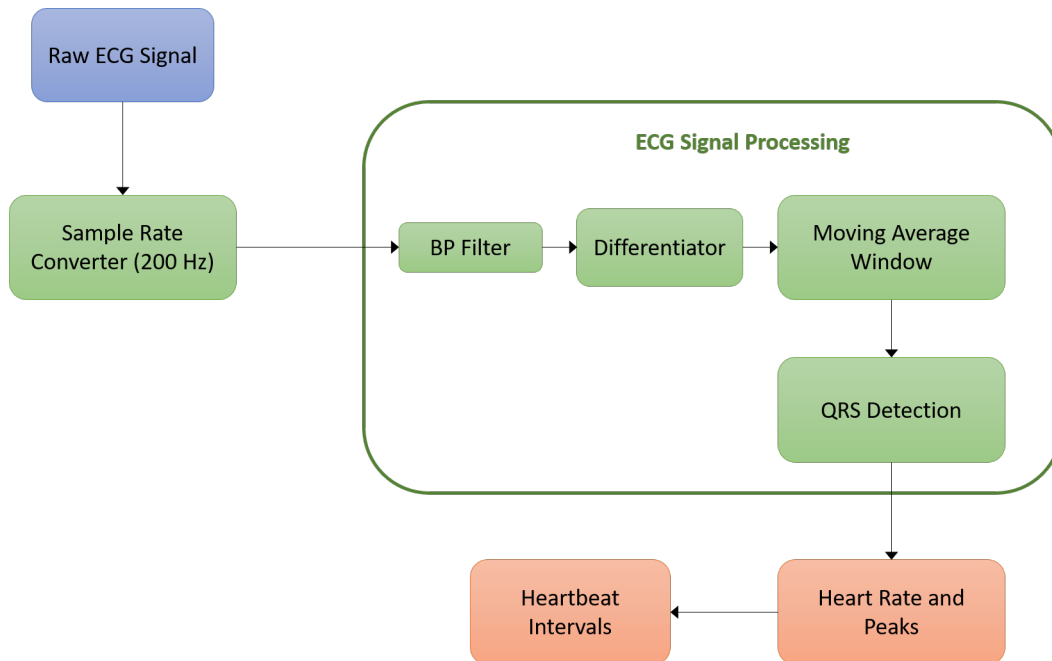
Figure 5.5.7: Scheme representing the steps of the adopted HBI extraction procedure from the ECG signals

As the whole system works under the assumption that all the input signals are sampled at 200 Hz, the first step of the processing is a sample rate conversion from any initial sample frequency to 200 Hz.

The ECG signal is then filtered to estimate the energy of the QRS frequency band according to the following steps:

1. FIR BP filtering with cut-off frequencies: [5, 26] Hz;

2. computation of the derivative of the filtered signal;

3. calculation of the absolute value of the obtained derivative;

4. averaging of the absolute value obtained over a 80 ms window.

These steps allow to obtain a filtered signal characterized by clearer QRS complexes, facilitating the R-peaks detection.

The final stage of the QRS detection is the application of the corresponding QRS detection function, which follows the QRS detection rules adopted in the algorithm implemented in [27]. According to these rules it is possible to guide a moving threshold spanning all over the signal and to accordingly determine if a detected peak is noise-related or is an actual QRS peak. After detecting the peaks of interest, the corresponding HR is computed as:

$$\text{HR}(bpm) = 60 \cdot \frac{f_s(Hz)}{\text{QRS}(samples)} = \frac{60}{\text{HBI}(s)} \qquad (5.5.1)$$

where f_s is the sampling frequency ($f_s = 200$ Hz after the sample rate conversion) and QRS is the samples interval corresponding to the QRS complex detected.

Proceeding with the example of PT3 used in this chapter, figures 5.5.8 and 5.5.9 show the raw and filtered ECG signals while figures 5.5.10 and 5.5.11 show the detected peaks with the moving threshold and the corresponding HR of this patient. In all figures the same 10 s interval of reference is displayed.
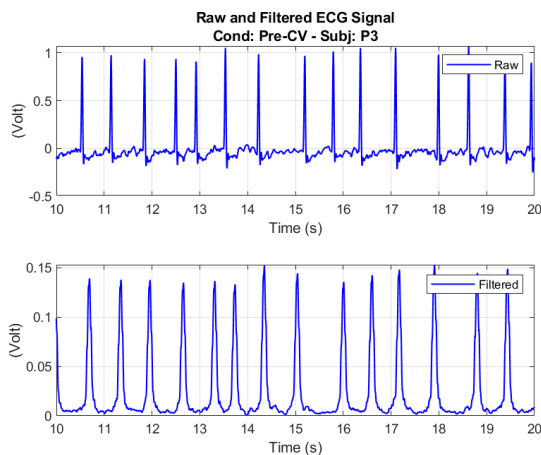
Figure 5.5.8
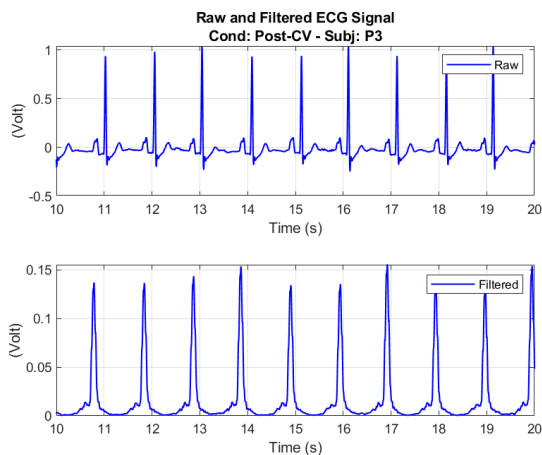
Figure 5.5.9
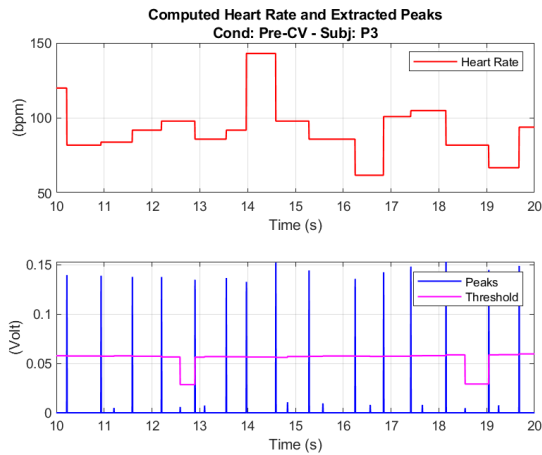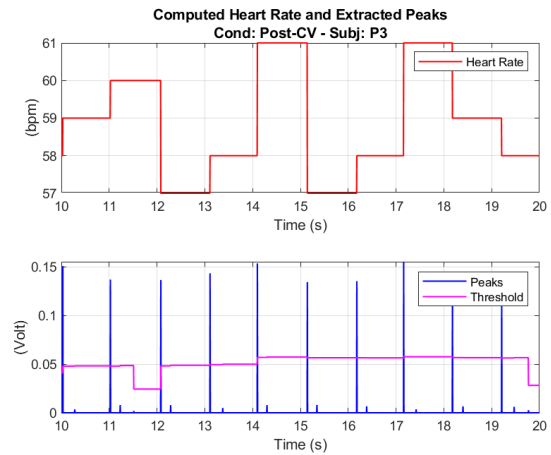
Figure 5.5.10   Figure 5.5.11

Two main features can be noticed on the example signals reported in figures 5.5.8 - 5.5.11:

- the raw and filtered ECG look quite different when referring to the Pre-CV and the Post-CV conditions. In fact, the NSR has been restored after the CV and hence a consequent change of HR can be already qualitatively perceived;

- as another evidence of the restored NSR, the HR scale ranges within lower values after the CV compared to the Pre-CV condition.

With reference to the latter observation, however the HR instantaneous change shown in figures 5.5.10 and 5.5.11 should be evaluated carefully. In fact, even after the performed filtering, some pieces of ECG signals are still quite noisy or corrupted by motion artifacts or affected by rapid large HR changes because of the particular features of the patients' AF. This leads to unexpected and sudden HR increase or decrease, partially affecting its mean value.

The ultimate stage of this processing consisted in calculating the HBI corresponding to the obtained HR values by using the equation (5.5.1).

Conclusions

The main attempt of this work has been the extraction of the heartbeat intervals from NIRS signals detected on two different categories of subjects tested under different kinds of conditions: healthy subjects and patients affected by AF. To accomplish that, NIRS signals have been sampled at a higher rate than usual (20 Hz) with the aim to see the "hidden" information related to the heartbeat, which is not visible when sampling at frequencies equal to or lower than 1 Hz, as it usually happens in NIRS cerebral oxymetry.

The main issue concerning the NIRS signals achieved by using the NIRO-200NX monitor, as described in this work, was the supposed interference of the extracerebral circulation on the LB signals, which led to the use of the SRS signals for the desired HBI extraction. This implied the need of a significant noise reduction of these signals finally leading to the heartbeat identification. Although most of the tested subjects showed very noisy SRS signals, some of them from both categories (HS and PT) showed, under some circumstances, striking clear beat-to-beat information on their SRS signals already in the acquisition phase, making the HBI extraction easier and smoother for these cases. However, overall the HBI information could be successfully extracted also from the noisiest signals, according to the adopted filtering method described in chapter 5.

The results of the adopted method of HBI extraction have been validated, when possible, by comparing the HBI and the HR extracted through the NIRS signals with those coming from the ECG corresponding signals. Overall, the obtained results and their comparison with the ECG-related information offered important confirmations of the validity of this method. However, some technical issues involved some subjects, determining anomalous results of the extraction process.

The main limits of this work consisted in the small number of participating subjects available up to now (only twelve subjects have been tested in total: six HS and six PT) and the large inter-subject variability in the behavior of the recorded NIRS signals (especially the SRS signals) which, under the same conditions, sometimes showed very clear HBI information while some other times this information was buried by excessive noise. These differences should be further investigated so that if the circumstances leading to clearer HBI on the SRS signals can be known in advance, they can be exploited to detect higher quality signals which may help enhance the performance of the extraction method. Besides, the acquisition conditions might be further improved by trying to ensure a better prevention of motion artifacts, which proved to extremely affect the quality of the recorded NIRS signals.

Lastly, the extraction method itself contains a very critical parameter to set which is the filtering pass-band width. This parameter is very important and very sensitive at the

same time, heavily affecting the goodness of the obtained results. Further experiments, involving many more subjects, may help validate this method and give a proper evaluation of its robustness, indicating which is the best trade-off value suitable for any processed NIRS signal.

Appendix A

Statistic Analysis Results - AvgS

In this appendix the histograms of the AvgS obtained from both HS and PT under *all* the testing conditions are reported along with the tables containing the corresponding statistical measures.

A.1   AvgS Histograms and Tables - HS

Figures A.1.1 - A.1.15 show the histograms of the average signals from all the HS under every testing condition and table A.1.1 reports the corresponding statistical measures.
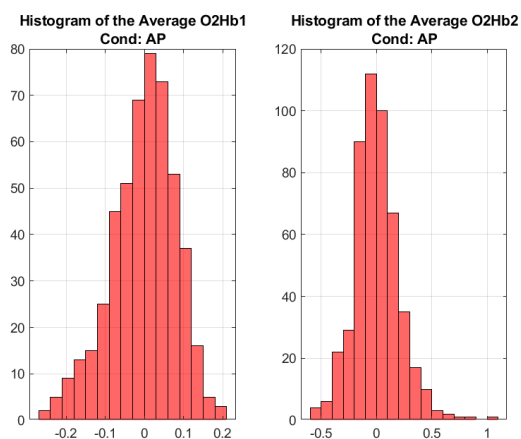

Figure A.1.1
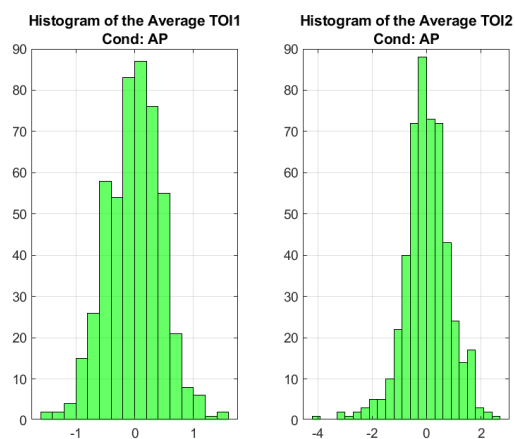

Figure A.1.2
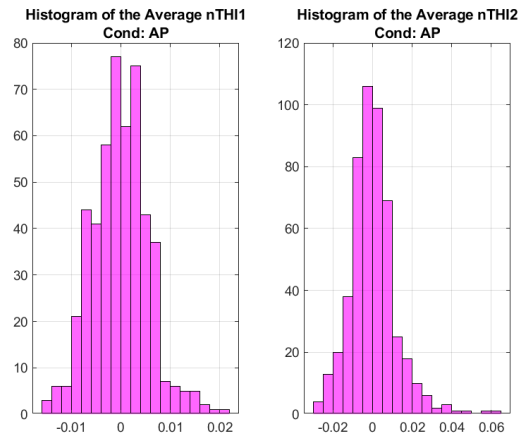
Figure A.1.3
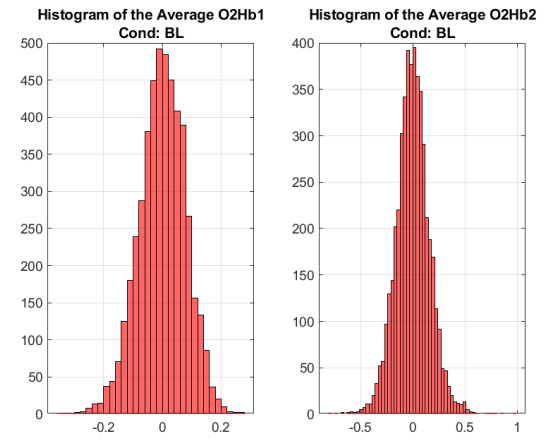
Figure A.1.4
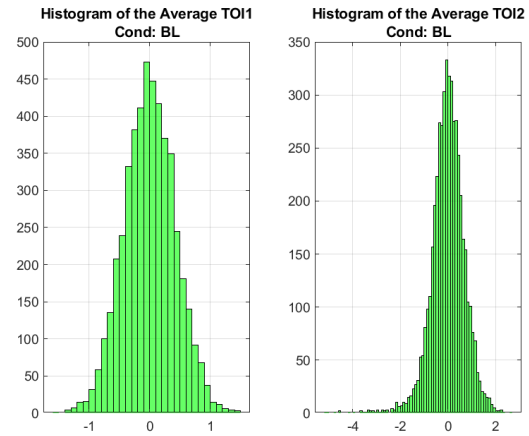
Figure A.1.5
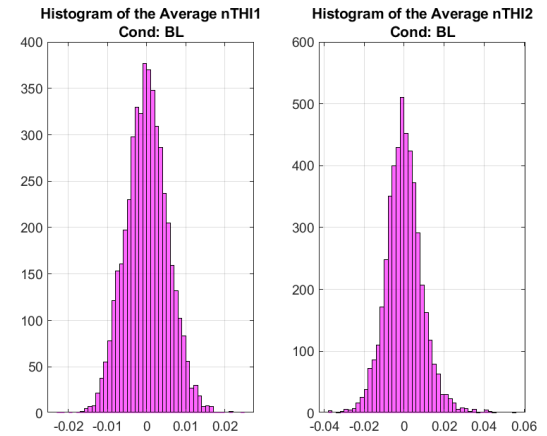
Figure A.1.6
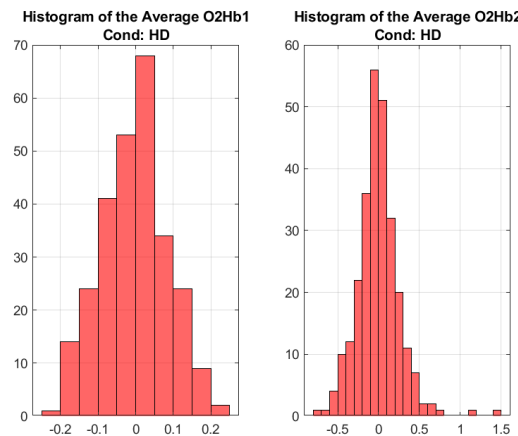
Figure A.1.7
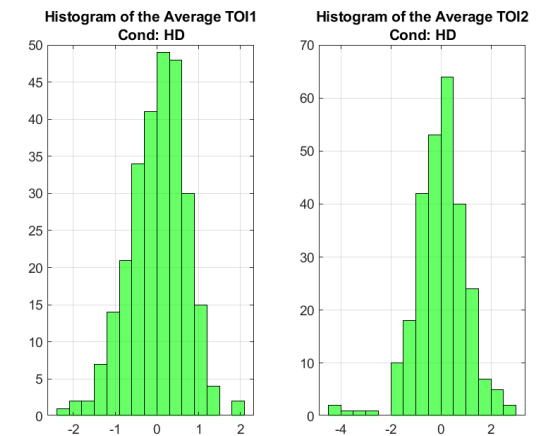
Figure A.1.8
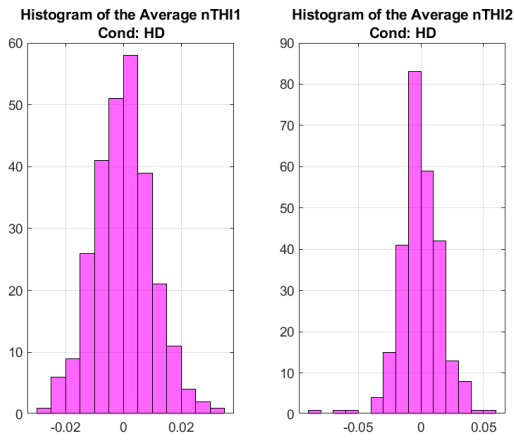
Figure A.1.9
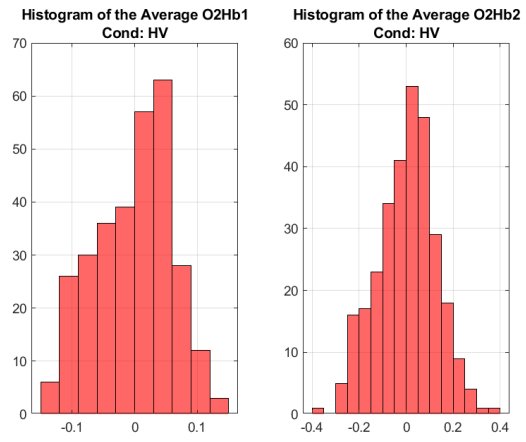
Figure A.1.10
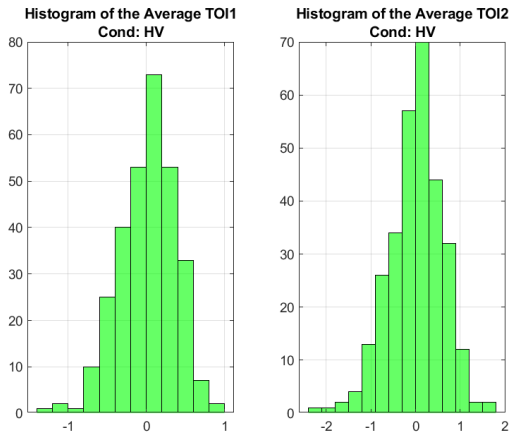
Figure A.1.11
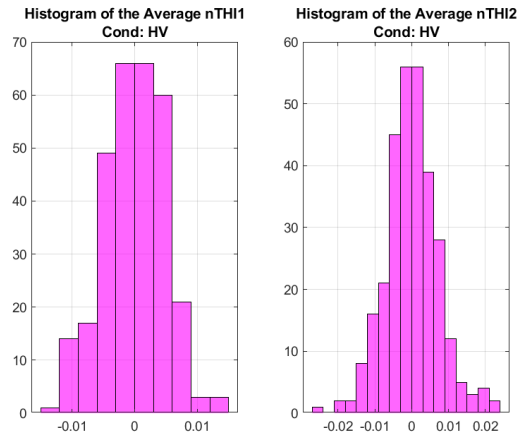
Figure A.1.12

Figure A.1.13

Figure A.1.14

81

Histogram of the Average nTHI1 Cond: VM

Histogram of the Average nTHI2 Cond: VM
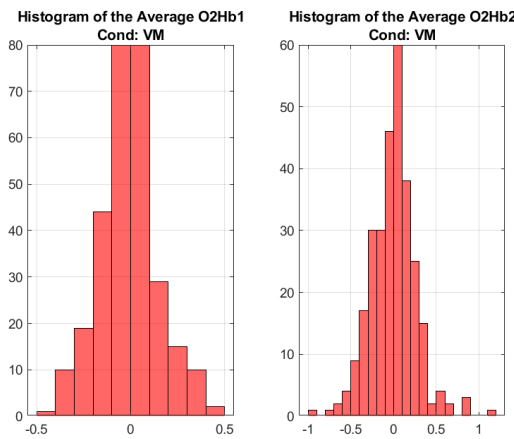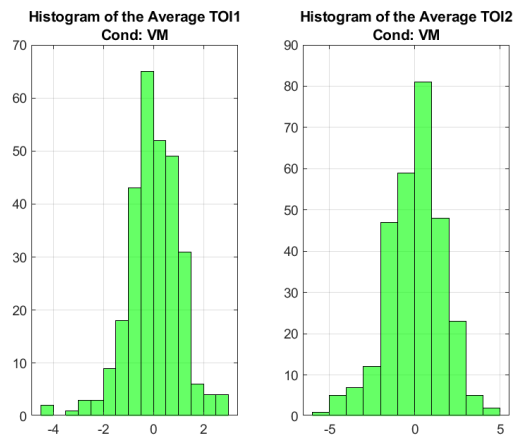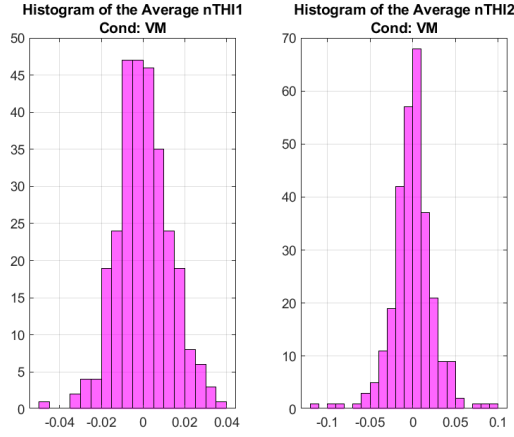
Figure A.1.15

Table A.1.1: STD, skewness and kurtosis of the AvgS obtained from all the HS under every testing condition

Avg. Signals Statistics	Conditions								
	Apnea			Baseline			Head Down		
HS (1/2)	Std	Skewness	Kurtosis	Std	Skewness	Kurtosis	Std	Skewness	Kurtosis
O2Hb1	0.08	-0.42	3.05	0.08	-0.22	3.23	0.09	0.04	2.64
O2Hb2	0.20	0.61	5.11	0.16	0.12	4.42	0.26	0.85	7.38
TOI1	0.47	-0.10	3.25	0.42	0.02	3.02	0.68	-0.36	3.33
TOI2	0.84	-0.52	5.11	0.71	-0.84	7.18	1.01	-0.66	5.47
nTHI1	0.01	0.28	3.61	0.01	0.08	3.17	0.01	0.08	3.12
nTHI2	0.01	1.00	6.33	0.01	0.38	4.86	0.02	-0.39	5.89

Avg. Signals Statistics	Conditions					
	Hyperventilation			Valsalva Maneuver		
HS (2/2)	STD	Skewness	Kurtosis	STD	Skewness	Kurtosis
O2Hb1	0.06	-0.20	2.31	1.04	-0.50	4.84
O2Hb2	0.12	-0.15	2.96	1.62	-0.41	3.64
TOI1	0.36	-0.48	3.46	0.16	0.22	3.33
TOI2	0.60	-0.37	3.45	0.27	0.32	5.02
nTHI1	0.00	-0.14	2.86	0.01	0.08	3.42
nTHI2	0.01	0.11	3.92	0.02	-0.33	6.81

A.2 AvgS Histograms and Tables - PT

Figures A.2.1 - A.2.6 show the histograms of the average signals from all the PT under every testing condition and table A.2.1 reports the corresponding statistical measures.
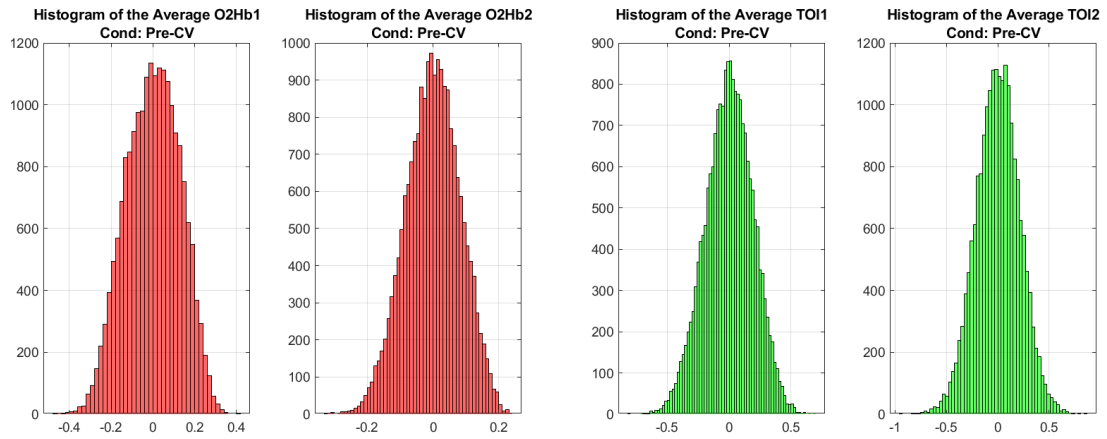

Figure A.2.1

Figure A.2.2
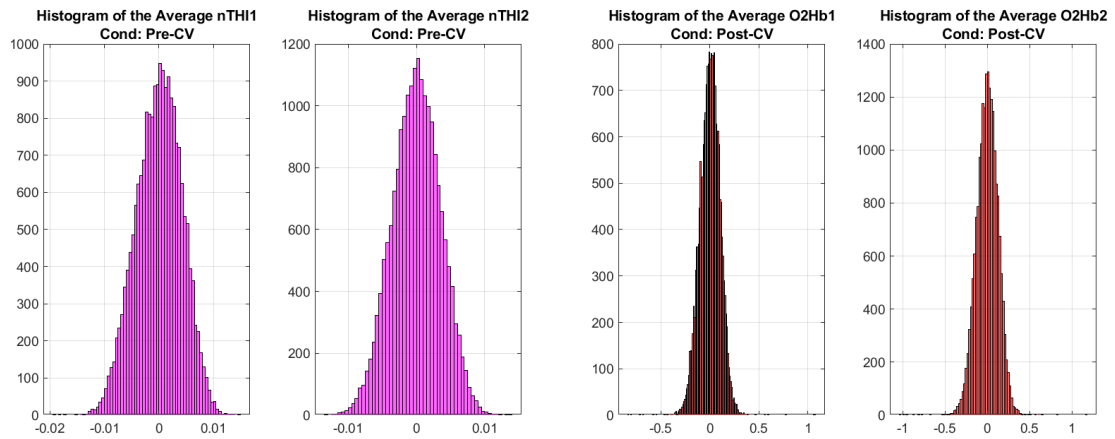
Figure A.2.3

Figure A.2.4

83
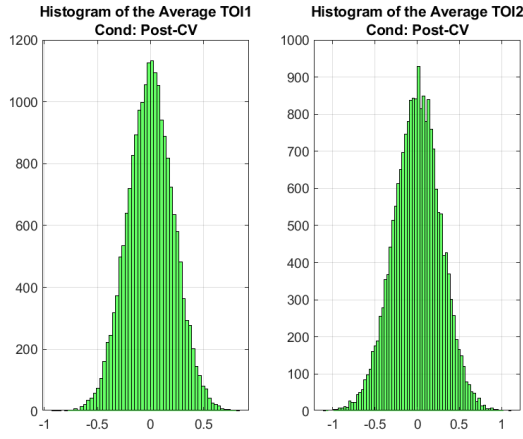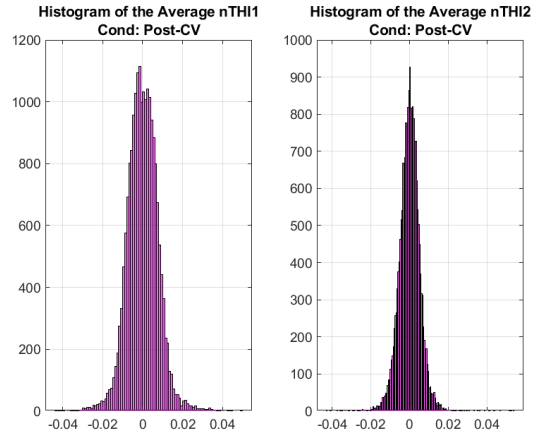
Figure A.2.5   Figure A.2.6

Table A.2.1: STD, skewness and kurtosis of the AvgS obtained from all the PT under every testing condition

Avg. Signals Statistics	Conditions					
	Pre-CV			Post-CV		
PT	STD	Skewness	Kurtosis	STD	Skewness	Kurtosis
O2Hb1	0.13	-0.12	2.52	0.10	-0.07	5.11
O2Hb2	0.08	-0.13	2.80	0.13	-0.11	4.69
TOI1	0.19	-0.10	2.89	0.22	0.00	3.03
TOI2	0.21	-0.05	3.06	0.28	-0.06	3.08
nTHI1	0.00	-0.15	2.76	0.01	0.14	5.19
nTHI2	0.00	-0.05	2.85	0.01	0.05	7.81

Appendix B

Statistic Analysis Results - OTM and UTM

This appendix contains all the results of the statistical analysis on the OTM and UTM values belonging to the AvgS from every subject under every condition.

B.1 OTM and UTM Tables - HS

Tables B.1.1 and B.1.2 contain the mean, STD, skewness and kurtosis of the OTM and UTM values from the AvgS of every HS under every testing condition.

Table B.1.1: Mean, STD, skewness and kurtosis of the OTM values from the AvgS of every HS under every condition

OTM Statistics - HS	Avg. Signals	Conditions				
		AP	BL	HD	HV	VM
Mean	O2Hb1	0.06	0.06	0.07	0.05	0.11
	O2Hb2	0.15	0.12	0.19	0.10	0.19
	TOI1	0.36	0.34	0.55	0.30	0.78
	TOI2	0.64	0.52	0.75	0.48	1.31
	nTHI1	0.00	0.00	0.01	0.00	0.01
	nTHI2	0.01	0.01	0.01	0.01	0.02

OTM Statistics - HS	Avg. Signals	Conditions				
		AP	BL	HD	HV	VM
Skewness	O2Hb1	0.88	0.93	0.79	0.90	1.18
	O2Hb2	2.05	1.76	2.93	1.14	2.27
	TOI1	1.28	1.01	1.23	0.83	1.06
	TOI2	1.10	1.20	1.21	0.85	1.05
	nTHI1	1.62	1.15	1.21	1.02	0.95
	nTHI2	2.31	1.98	1.20	1.45	1.91

OTM Statistics - HS	Avg. Signals	Conditions				
		AP	BL	HD	HV	VM
STD	O2Hb1	0.04	0.04	0.05	0.03	0.11
	O2Hb2	0.15	0.11	0.20	0.07	0.19
	TOI1	0.27	0.26	0.35	0.18	0.62
	TOI2	0.50	0.40	0.58	0.33	0.88
	nTHI1	0.00	0.00	0.01	0.00	0.01
	nTHI2	0.01	0.01	0.01	0.00	0.02

OTM Statistics - HS	Avg. Signals	Conditions				
		AP	BL	HD	HV	VM
Kurtosis	O2Hb1	3.41	3.71	2.79	3.56	3.51
	O2Hb2	9.36	8.40	15.54	4.29	9.78
	TOI1	5.08	3.89	5.29	3.26	4.11
	TOI2	3.75	4.57	4.26	3.31	3.90
	nTHI1	6.10	4.67	4.20	4.23	3.63
	nTHI2	9.95	9.02	4.24	5.17	7.45

Table B.1.2: Mean, STD, skewness and kurtosis of the UTM values from the AvgS of every HS under every condition

UTM Statistics - HS	Conditions				
Avg. Signals	AP	BL	HD	HV	VM
O2Hb1	-0.07	-0.06	-0.07	-0.05	-0.13
O2Hb2	-0.15	-0.13	-0.19	-0.10	-0.20
TOI1	-0.37	-0.34	-0.52	-0.27	-0.78
TOI2	-0.60	-0.52	-0.75	-0.45	-1.19
nTHI1	0.00	0.00	-0.01	0.00	-0.01
nTHI2	-0.01	-0.01	-0.01	-0.01	-0.02

(Mean)

UTM Statistics - HS	Conditions				
Avg. Signals	AP	BL	HD	HV	VM
O2Hb1	-0.99	-1.23	-0.64	-0.32	-1.02
O2Hb2	-1.28	-1.48	-1.30	-0.79	-1.36
TOI1	-1.06	-0.99	-1.14	-1.30	-2.15
TOI2	-2.28	-2.89	-2.28	-1.30	-1.43
nTHI1	-0.86	-0.98	-0.88	-0.82	-1.48
nTHI2	-1.11	-1.45	-2.77	-1.40	-2.57

(Skewness)

UTM Statistics - HS	Conditions				
Avg. Signals	AP	BL	HD	HV	VM
O2Hb1	0.06	0.05	0.05	0.04	0.09
O2Hb2	0.11	0.10	0.15	0.08	0.17
TOI1	0.30	0.25	0.47	0.25	0.76
TOI2	0.61	0.54	0.77	0.42	1.15
nTHI1	0.00	0.00	0.01	0.00	0.01
nTHI2	0.01	0.01	0.01	0.00	0.02

(STD)

UTM Statistics - HS	Conditions				
Avg. Signals	AP	BL	HD	HV	VM
O2Hb1	3.42	4.86	2.56	2.28	3.24
O2Hb2	4.42	6.38	4.51	3.03	5.45
TOI1	4.21	3.87	4.30	5.31	8.90
TOI2	9.84	16.82	9.79	5.02	4.97
nTHI1	3.39	4.01	3.39	2.88	6.38
nTHI2	3.70	5.92	14.43	5.27	12.05

(Kurtosis)

B.2 OTM and UTM Tables - PT

Tables B.2.1 and B.2.2 contain the mean, STD, skewness and kurtosis of the OTM and UTM values from the AvgS of every PT under every testing condition.

Table B.2.1: Mean, STD, skewness and kurtosis of the OTM values from the AvgS of every PT under every condition

OTM Statistics - PT	Conditions	
Avg. Signals	Pre-CV	Post-CV
O2Hb1	0.11	0.08
O2Hb2	0.07	0.10
TOI1	0.15	0.17
TOI2	0.17	0.22
nTHI1	0.00	0.01
nTHI2	0.00	0.00

(Mean)

OTM Statistics - PT	Conditions	
Avg. Signals	Pre-CV	Post-CV
O2Hb1	0.61	2.08
O2Hb2	0.73	1.70
TOI1	0.86	1.01
TOI2	1.02	1.02
nTHI1	0.80	2.15
nTHI2	0.87	2.98

(Skewness)

OTM Statistics - PT	Conditions	
Avg. Signals	Pre-CV	Post-CV
O2Hb1	0.07	0.06
O2Hb2	0.05	0.07
TOI1	0.11	0.13
TOI2	0.13	0.17
nTHI1	0.00	0.01
nTHI2	0.00	0.00

(STD)

OTM Statistics - PT	Conditions	
Avg. Signals	Pre-CV	Post-CV
O2Hb1	2.73	20.41
O2Hb2	2.87	14.10
TOI1	3.43	3.90
TOI2	3.97	3.99
nTHI1	3.26	11.08
nTHI2	3.45	24.89

(Kurtosis)

Table B.2.2: Mean, STD, skewness and kurtosis of the UTM values from the AvgS of every PT under every condition

UTM Statistics - PT		Conditions	
	Avg. Signals	Pre-CV	Post-CV
Mean	O2Hb1	-0.11	-0.08
	O2Hb2	-0.07	-0.10
	TOI1	-0.15	-0.17
	TOI2	-0.17	-0.22
	nTHI1	0.00	-0.01
	nTHI2	0.00	0.00

UTM Statistics - PT		Conditions	
	Avg. Signals	Pre-CV	Post-CV
Skewness	O2Hb1	-0.75	-1.51
	O2Hb2	-0.97	-1.59
	TOI1	-0.96	-1.00
	TOI2	-1.06	-1.05
	nTHI1	-0.87	-1.86
	nTHI2	-0.92	-2.22

UTM Statistics - PT		Conditions	
	Avg. Signals	Pre-CV	Post-CV
STD	O2Hb1	0.08	0.07
	O2Hb2	0.05	0.08
	TOI1	0.12	0.13
	TOI2	0.13	0.17
	nTHI1	0.00	0.00
	nTHI2	0.00	0.00

UTM Statistics - PT		Conditions	
	Avg. Signals	Pre-CV	Post-CV
Kurtosis	O2Hb1	3.18	9.11
	O2Hb2	3.77	10.23
	TOI1	3.63	3.95
	TOI2	4.14	4.01
	nTHI1	3.51	8.98
	nTHI2	3.58	13.18

Appendix C

Correlation Analysis Results

This appendix contains the results of the correlation analysis between the O2Hb and the SRS signals in terms of computation of the Pearson coefficient and evaluation of the correlation coefficient with delay between the signals.

C.1 Pearson Coefficient - HS

Figures C.1.1 - C.1.10 and table C.1.1 report the Pearson correlation results between the O2Hb and the SRS signals obtained from all the HS under every testing condition.

Table C.1.1: Correlation coefficient values computed between the O2Hb and the SRS signals - HS (maxima positive coefficients and maxima negative coefficients marked in red and blue respectively)

$\rho(\text{O2Hb, TOI})$			Conditions				
	HS		AP	BL	HD	HV	VM
Subjects	1	Ch1	0.42	0.44	0.52	0.45	0.38
		Ch2	0.71	0.73	0.69	0.69	0.57
	2	Ch1	0.51	0.54	NA	0.64	0.58
		Ch2	0.35	0.36	NA	0.22	0.26
	3	Ch1	0.76	0.71	0.68	0.71	0.87
		Ch2	-0.06	0.01	0.03	0.04	-0.06
	4	Ch1	-0.05	-0.02	-0.23	0.01	-0.05
		Ch2	0.76	0.75	0.62	0.90	0.24
	5	Ch1	0.62	0.66	0.64	0.67	0.77
		Ch2	0.63	0.64	0.55	0.59	0.45
	6	Ch1	0.53	0.52	0.43	0.40	0.50
		Ch2	0.81	0.82	0.72	0.73	0.49

$\rho(\text{O2Hb, nTHI})$			Conditions				
	HS		AP	BL	HD	HV	VM
Subjects	1	Ch1	0.34	0.59	0.53	0.76	0.71
		Ch2	0.85	0.81	0.75	0.70	0.56
	2	Ch1	0.64	0.61	NA	0.49	0.52
		Ch2	0.43	0.43	NA	0.44	0.40
	3	Ch1	0.76	0.67	0.77	0.75	0.81
		Ch2	-0.02	0.07	0.26	-0.04	-0.06
	4	Ch1	0.04	0.05	-0.05	0.02	-0.12
		Ch2	0.90	0.87	0.46	0.80	0.48
	5	Ch1	0.66	0.63	0.43	0.54	0.74
		Ch2	0.87	0.79	0.76	0.70	0.65
	6	Ch1	0.73	0.71	0.39	0.52	0.53
		Ch2	0.95	0.94	0.94	0.91	0.40
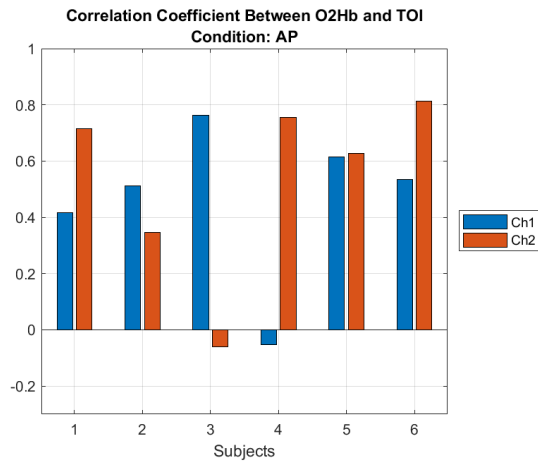
Figure C.1.1

Figure C.1.2
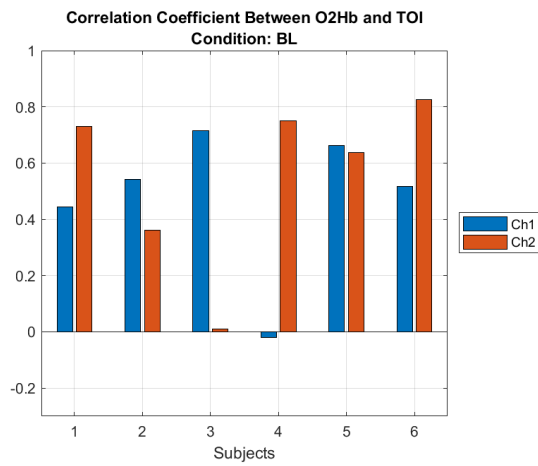
Figure C.1.3
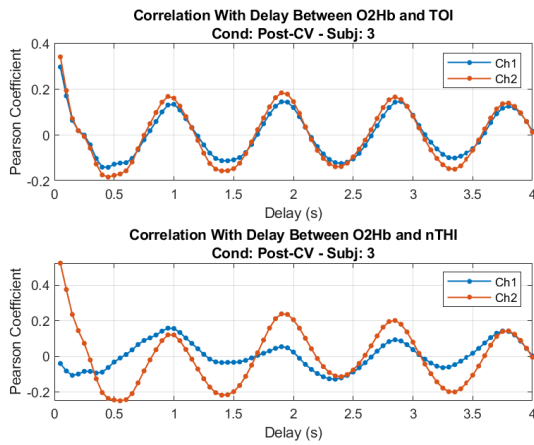

Figure C.1.4
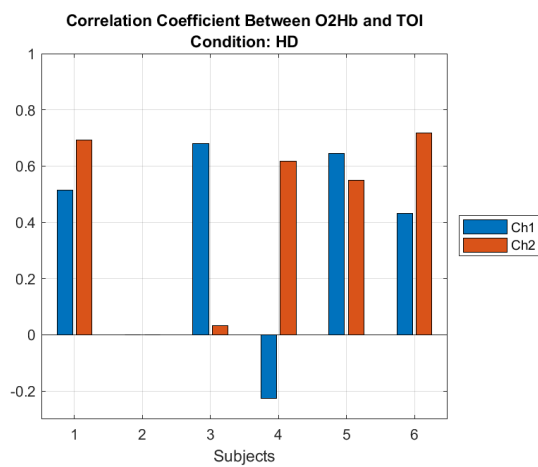
Figure C.1.5
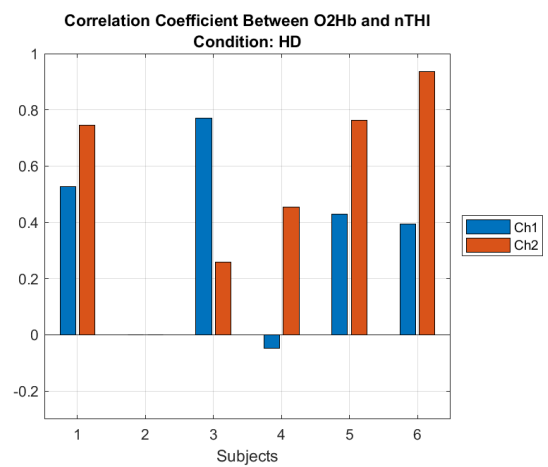
Figure C.1.6
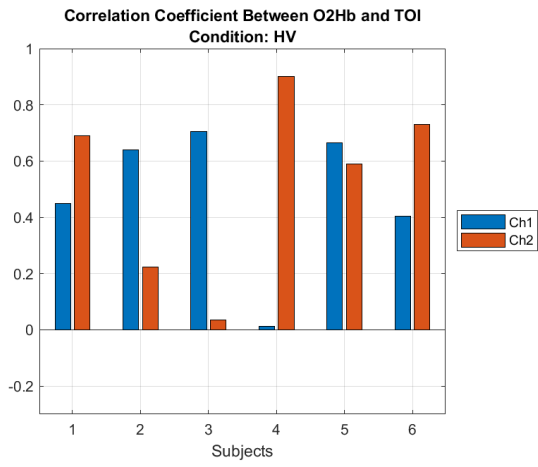
Figure C.1.7
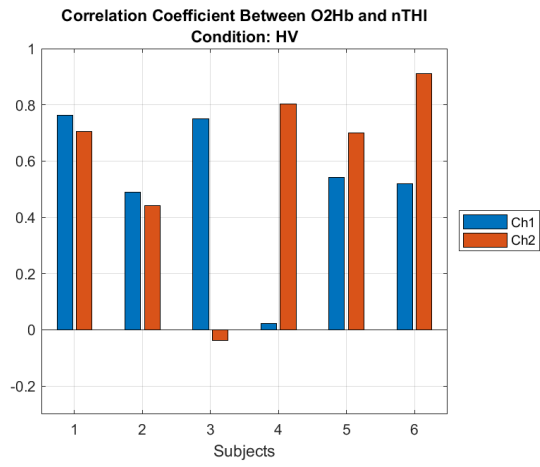
Figure C.1.8
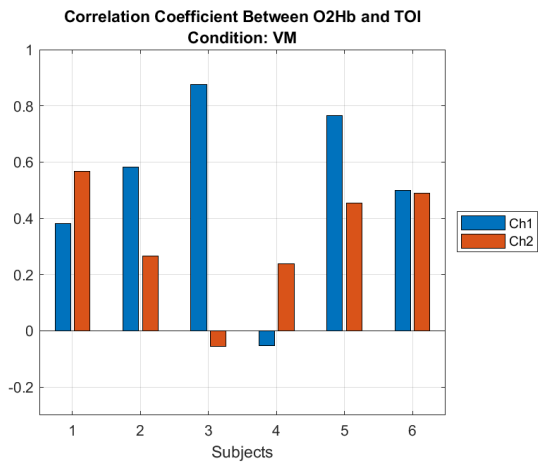
Figure C.1.9
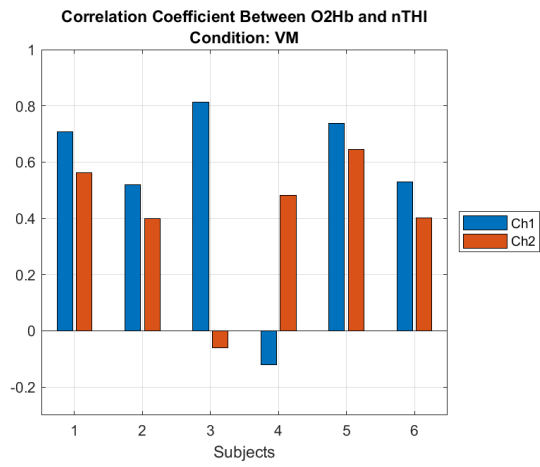

Figure C.1.10

C.2 Pearson Coefficient With Delay - HS

Figures C.2.1 - C.2.29 show the trend of the evaluated Pearson correlation between the O2Hb and the SRS signals with increasing delay between the two signals obtained from all the HS under every testing condition.
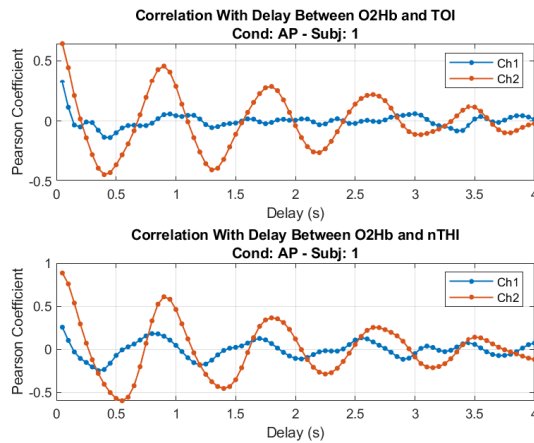
Figure C.2.1
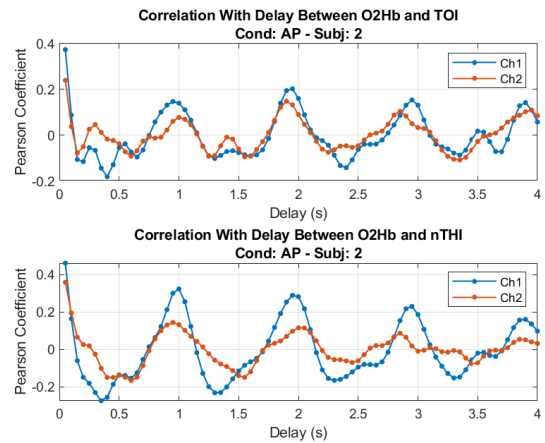
Figure C.2.2
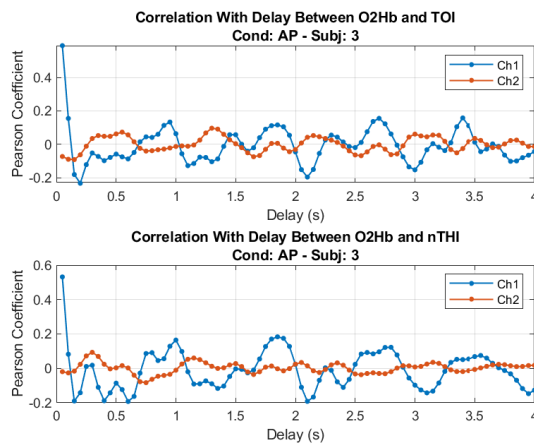
Figure C.2.3
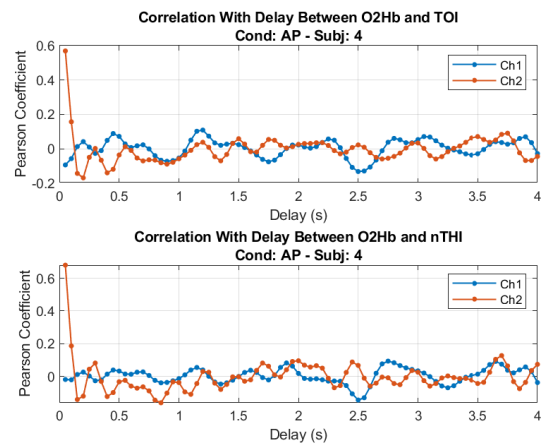
Figure C.2.4
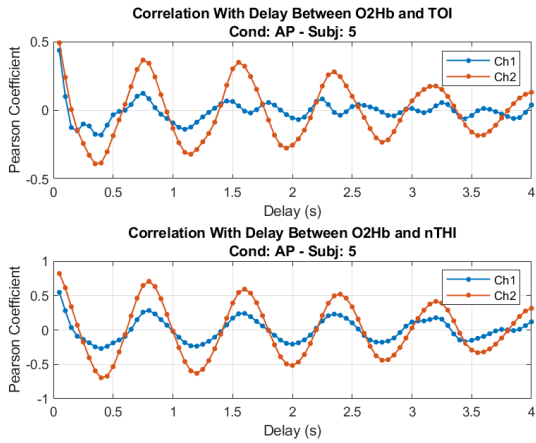
Figure C.2.5
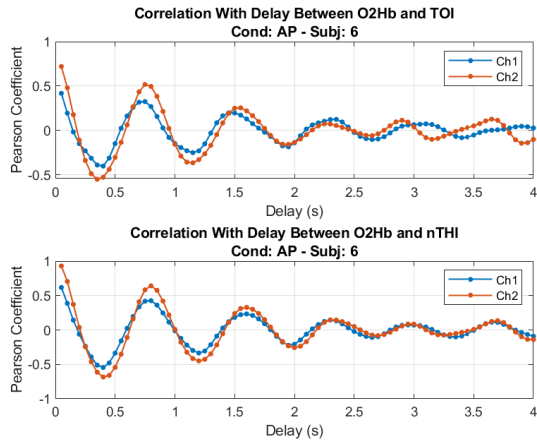
Figure C.2.6
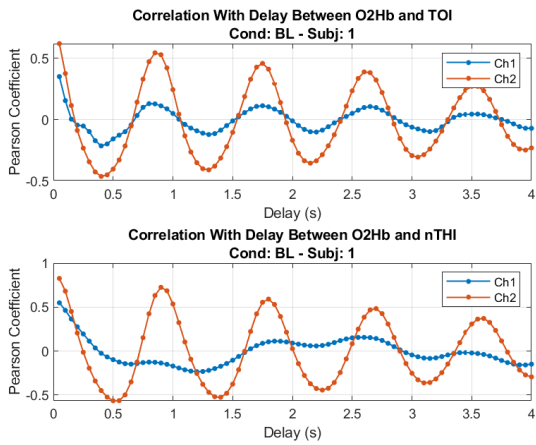
Figure C.2.7
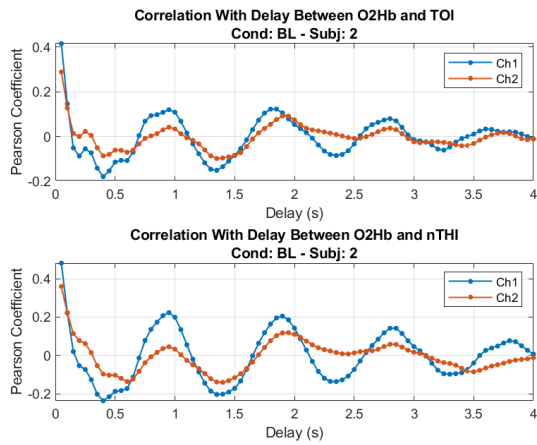
Figure C.2.8
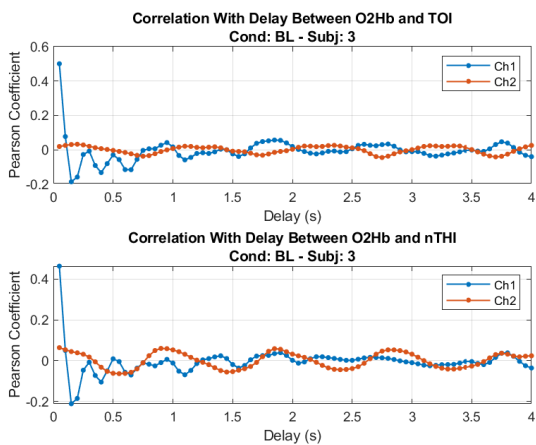
Figure C.2.9
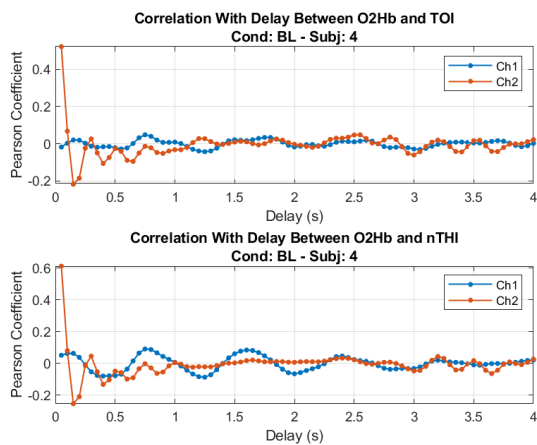
Figure C.2.10
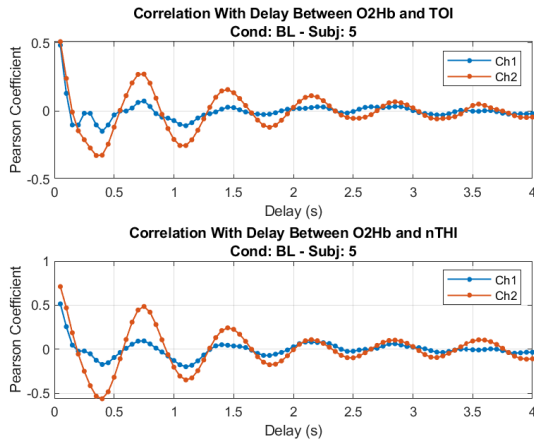
Figure C.2.11
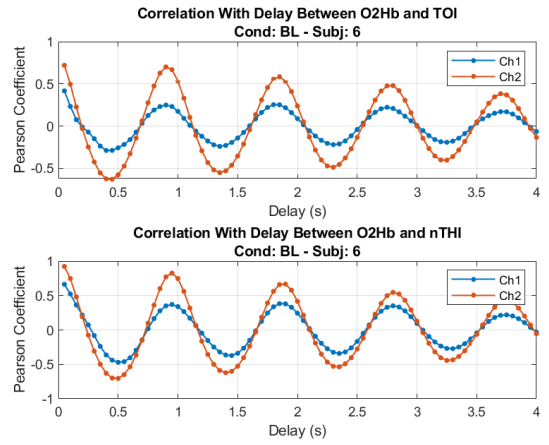
Figure C.2.12
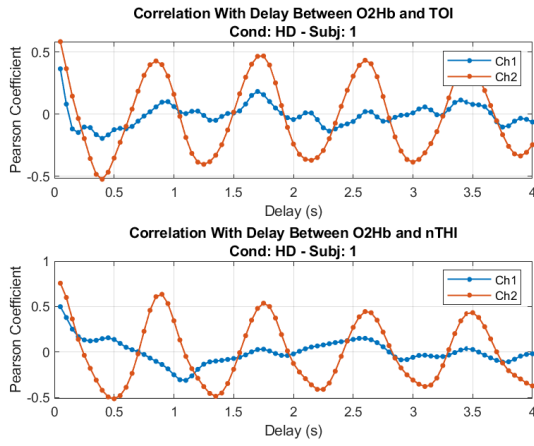
Figure C.2.13
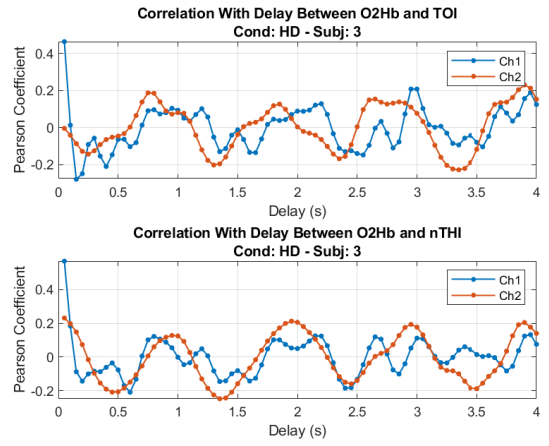
Figure C.2.14
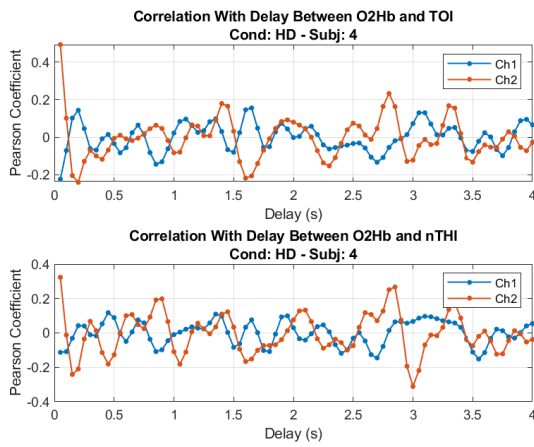
Figure C.2.15

Figure C.2.16

94
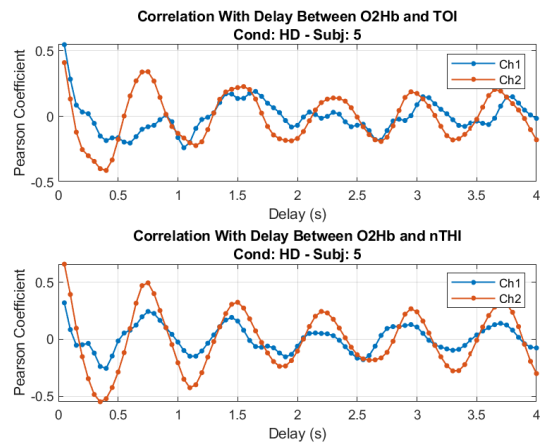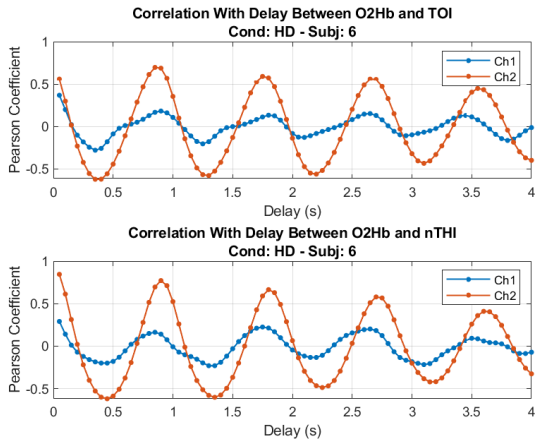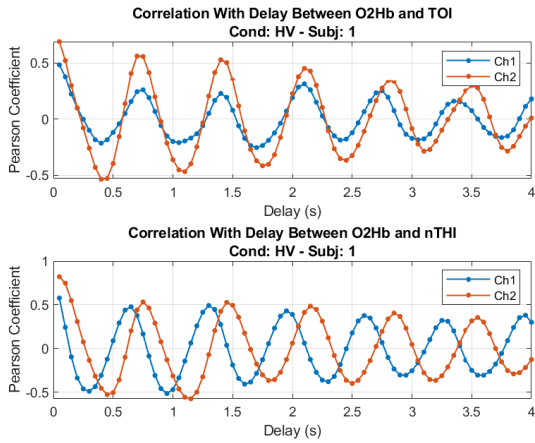
Figure C.2.17

Figure C.2.18
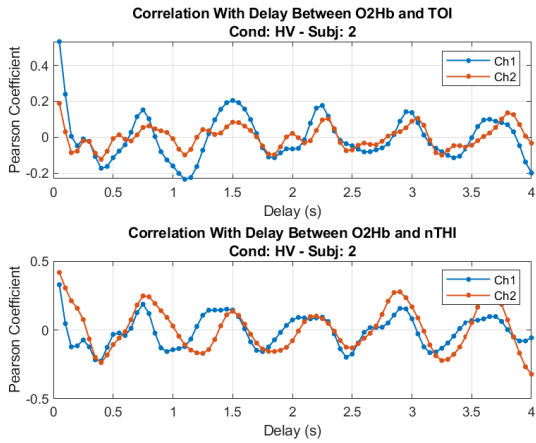
Figure C.2.19
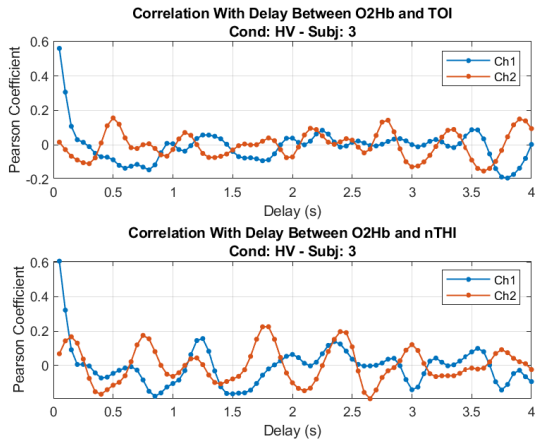
Figure C.2.20
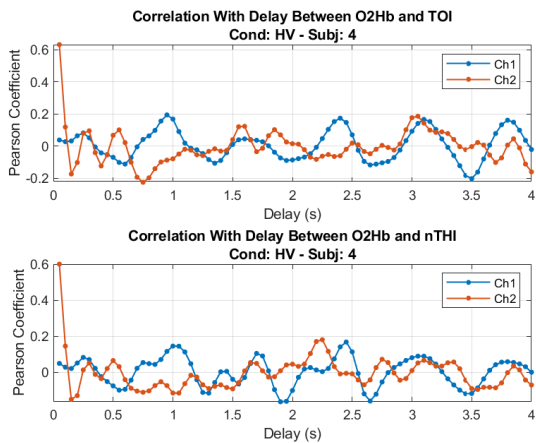
Figure C.2.21

Figure C.2.22

95
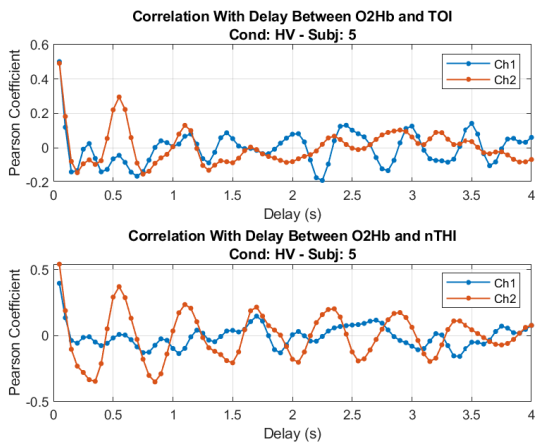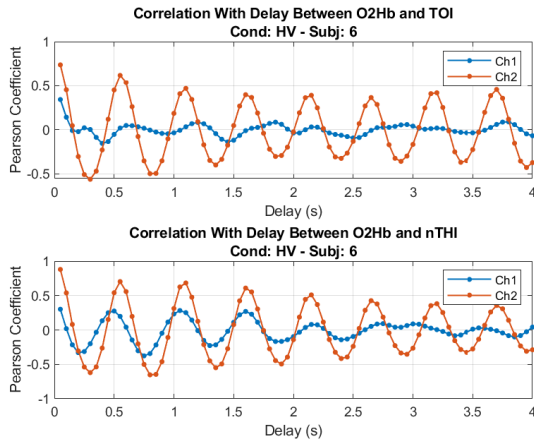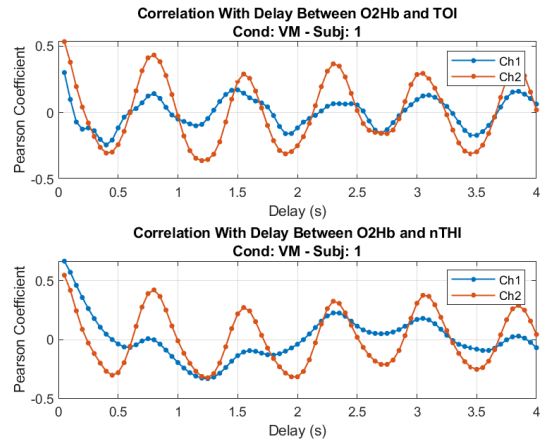
Figure C.2.23

Figure C.2.24
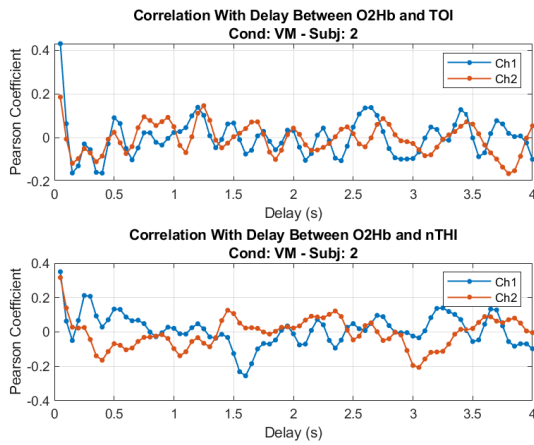
Figure C.2.25
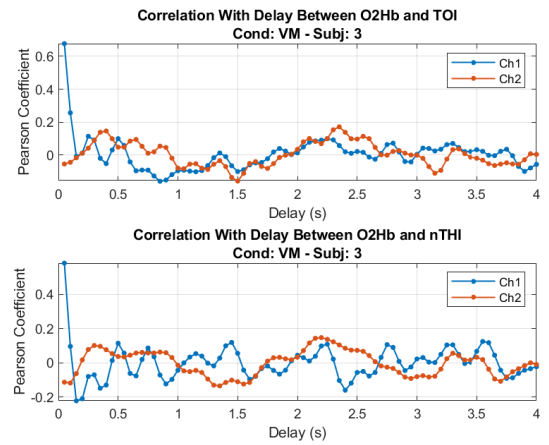
Figure C.2.26
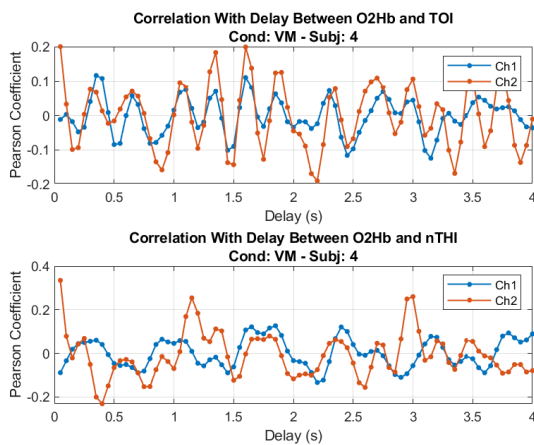
Figure C.2.27
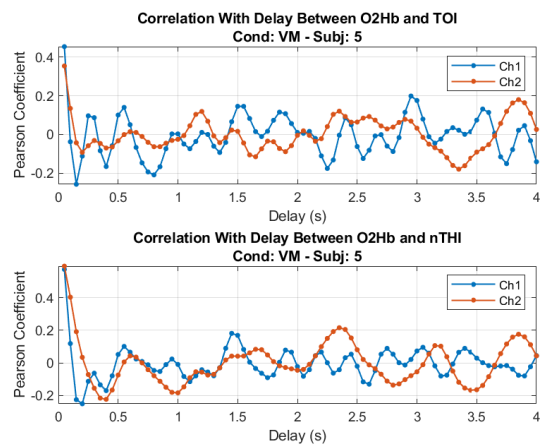
Figure C.2.28
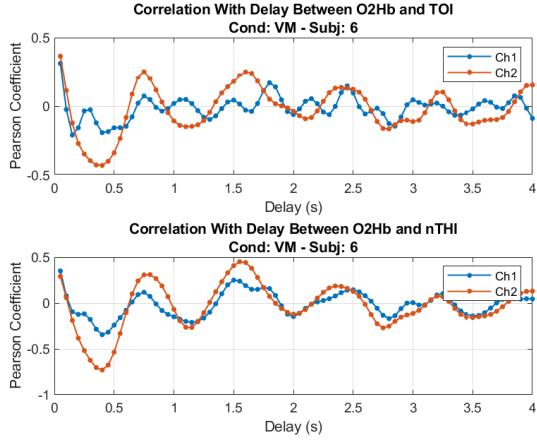
Figure C.2.29

C.3 Pearson Coefficient - PT

Figures C.3.1 - C.3.4 and table C.3.1 report the Pearson correlation results between the O2Hb and the SRS signals obtained from all the PT under every testing condition.

Table C.3.1: Correlation coefficient values computed between the O2Hb and the SRS signals - PT (maxima positive coefficients and maxima negative coefficients marked in red and blue respectively)

ρ(O2Hb, TOI)			Conditions		ρ(O2Hb, nTHI)			Conditions	
PT			Pre-CV	Post-CV	PT			Pre-CV	Post-CV
	1	Ch1	0.92	0.23		1	Ch1	0.96	-0.16
		Ch2	0.91	0.38			Ch2	0.97	0.36
	2	Ch1	0.92	0.46		2	Ch1	0.96	0.24
		Ch2	-0.73	-0.51			Ch2	-0.89	-0.46
Subjects	3	Ch1	0.23	0.35	Subjects	3	Ch1	-0.09	-0.02
		Ch2	0.54	0.41			Ch2	0.52	0.59
	4	Ch1	0.49	0.28		4	Ch1	0.39	0.10
		Ch2	-0.07	-0.04			Ch2	0.12	0.11
	5	Ch1	0.60	0.40		5	Ch1	0.85	0.52
		Ch2	0.30	0.34			Ch2	0.16	0.14
	6	Ch1	0.53	0.87		6	Ch1	0.85	0.84
		Ch2	0.32	0.76			Ch2	0.76	0.81

97
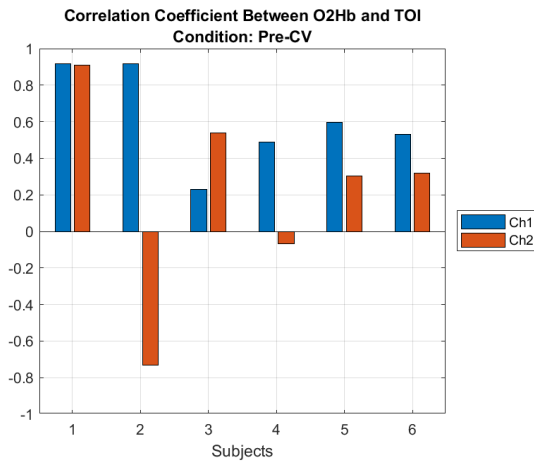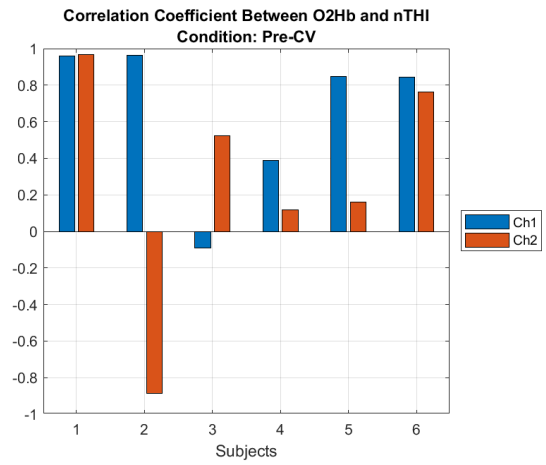
Figure C.3.1

Figure C.3.2
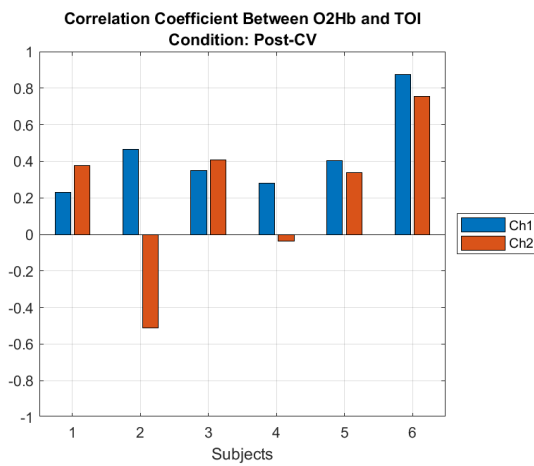
Figure C.3.3
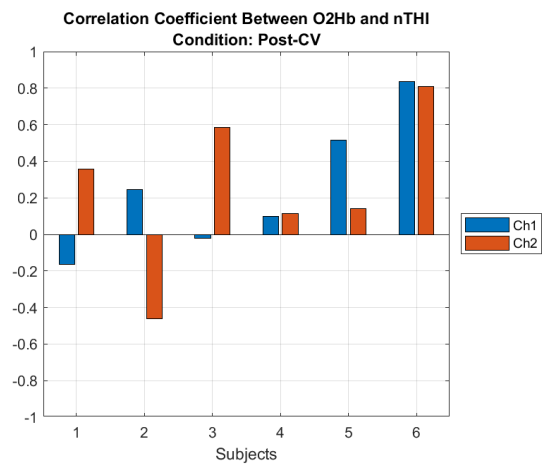
Figure C.3.4

C.4 Pearson Coefficient With Delay - PT

Figures C.4.1 - C.4.12 show the trend of the evaluated Pearson correlation between the O2Hb and the SRS signals with increasing delay between the two signals obtained from all the PT under every testing condition.
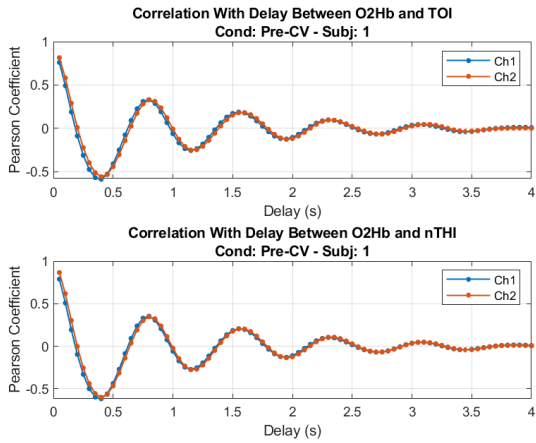
Figure C.4.1
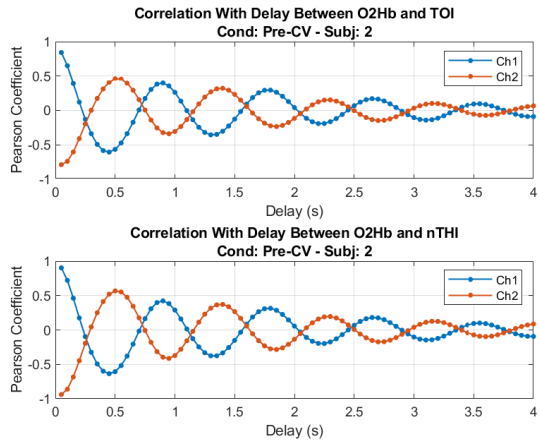
Figure C.4.2
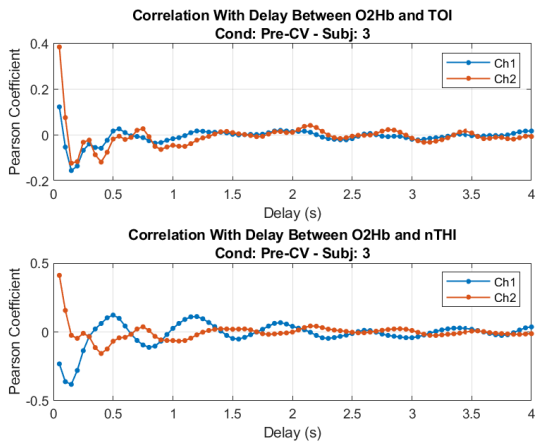
Figure C.4.3
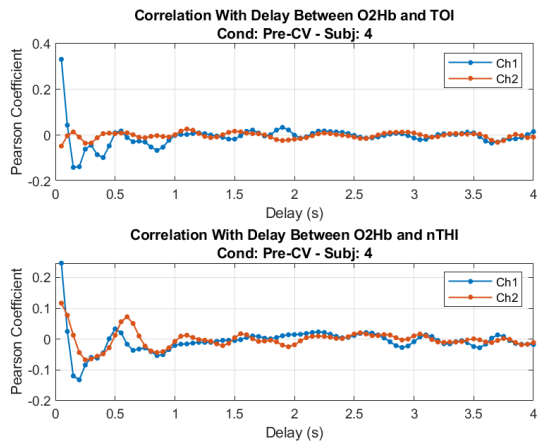
Figure C.4.4
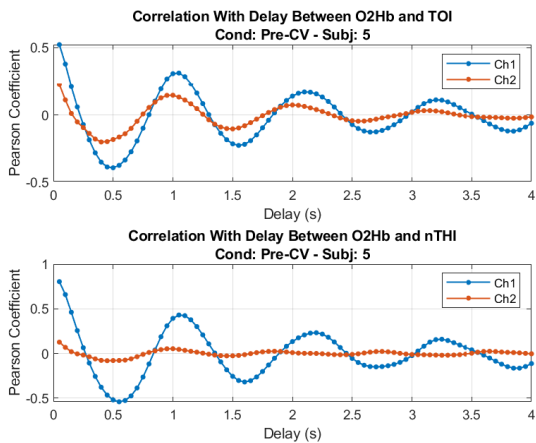
Figure C.4.5
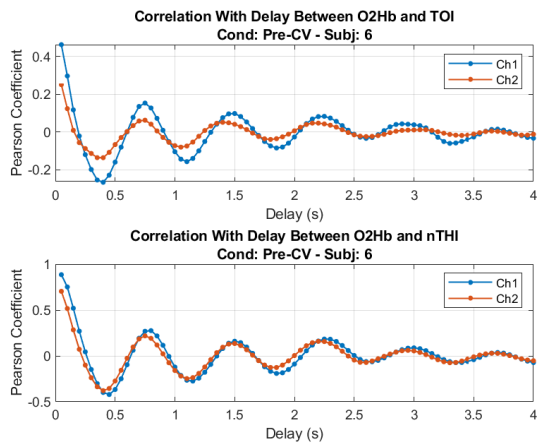
Figure C.4.6
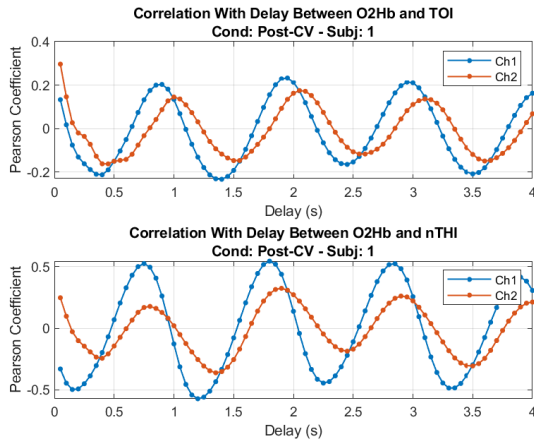
Figure C.4.7
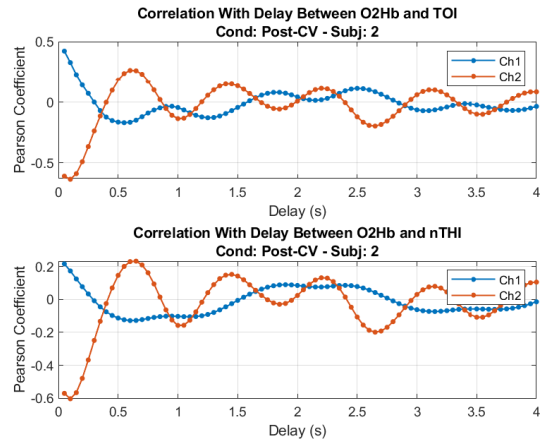
Figure C.4.8

Figure C.4.9
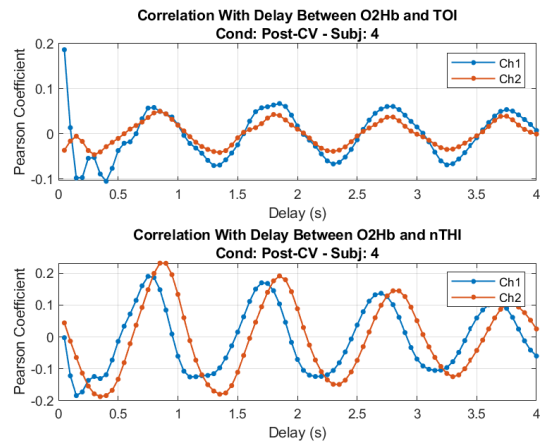
Figure C.4.10
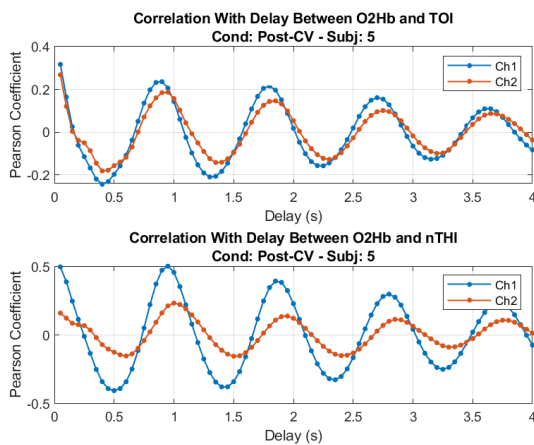
Figure C.4.11

Figure C.4.12

100
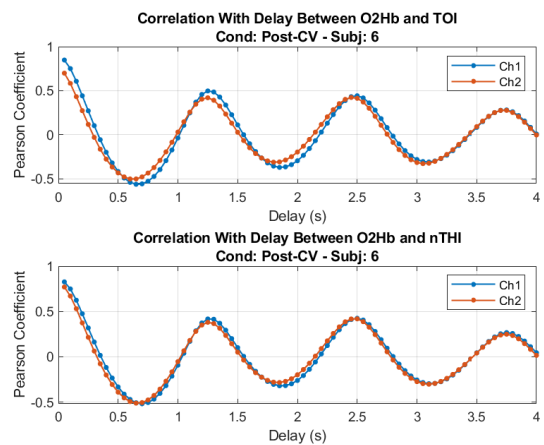
Appendix D

HBI and HR Extracted

This appendix contains the tables of the mean (μ) and standard deviation (σ) of both HBI and HR values obtained from *every* subject under *every* testing condition.

D.1 HBI and HR Tables - HS

Tables D.1.1 - D.1.4 report the HBI and HR μ and σ obtained from the HS under all the testing conditions. The values marked in red are apparently anomalous values, maybe due to the particular morphology of the original SRS signals from that channel. This might be a consequence of recording technical issues encountered with that subject (e.g. HS3 and HS4 as mentioned in chapter 2) or the failure of the SRS signals filtering algorithm which has faced a particularly noisy signal, leading to an unreliable resulting filtered signal. Furthermore, due to the nature of the performed trials, all the HS signals are very short time series (the maximum duration is 4 min under the BL condition) and this may have affected the HBI extraction outcomes which would probably take more advantage on longer time series, characterized by more peaks.

Table D.1.1

HBI (s) - HS (1/2)			Conditions													
			Apnea				Baseline				Head Down			
			μ_1	μ_2	σ_1	σ_2	μ_1	μ_2	σ_1	σ_2	μ_1	μ_2	σ_1	σ_2
Subjects	1	TOI	0.84	0.88	0.13	0.10	0.87	0.88	0.14	0.07	0.86	0.85	0.13	0.06
		nTHI	0.87	0.88	0.16	0.07	0.89	0.87	0.16	0.05	0.76	0.85	0.09	0.05
	2	TOI	0.95	0.90	0.16	0.14	0.92	0.93	0.15	0.17	NA			
		nTHI	0.98	1.00	0.14	0.19	0.93	0.95	0.13	0.18				
	3	TOI	0.77	0.78	0.09	0.11	0.91	0.89	0.18	0.16	1.01	0.94	0.12	0.11
		nTHI	0.88	0.85	0.13	0.17	0.90	0.91	0.18	0.16	1.00	0.92	0.27	0.17
	4	TOI	0.82	0.30	0.16	0.03	0.73	0.78	0.12	0.13	0.79	0.65	0.12	0.06
		nTHI	0.84	0.30	0.15	0.03	0.74	0.80	0.12	0.13	0.84	0.65	0.10	0.07
	5	TOI	0.84	0.77	0.12	0.08	0.72	0.73	0.11	0.09	0.74	0.74	0.09	0.08
		nTHI	0.77	0.78	0.09	0.07	0.72	0.72	0.10	0.08	0.73	0.75	0.09	0.06
	6	TOI	0.72	0.78	0.09	0.09	0.90	0.92	0.12	0.08	0.85	0.91	0.13	0.05
		nTHI	0.76	0.78	0.10	0.08	0.92	0.91	0.08	0.08	0.95	0.90	0.16	0.05

Table D.1.2

HBI (s) - HS (2/2)			Conditions							
			Hyperventilation				Valsalva Maneuver			
			μ_1	μ_2	σ_1	σ_2	μ_1	μ_2	σ_1	σ_2
Subjects	1	TOI	0.67	0.69	0.05	0.06	0.68	0.75	0.08	0.07
		nTHI	0.67	0.69	0.03	0.04	0.75	0.75	0.11	0.04
	2	TOI	0.71	0.72	0.09	0.10	1.74	1.64	0.15	0.12
		nTHI	0.71	0.77	0.08	0.12	1.78	1.98	0.80	0.28
	3	TOI	0.68	0.64	0.10	0.09	0.60	1.69	0.08	0.26
		nTHI	0.64	0.67	0.08	0.07	0.63	1.64	0.08	0.30
	4	TOI	0.75	1.57	0.10	0.21	0.76	1.18	0.11	0.31
		nTHI	0.77	1.89	0.08	0.59	0.75	1.10	0.09	0.16
	5	TOI	0.53	0.55	0.07	0.08	0.67	0.60	0.12	0.08
		nTHI	0.52	0.57	0.04	0.04	0.71	0.63	0.06	0.10
	6	TOI	0.54	0.53	0.05	0.03	0.79	0.73	0.12	0.08
		nTHI	0.55	0.53	0.05	0.03	0.78	0.74	0.09	0.09

Table D.1.3

HR (bpm) - HS (1/2)			Conditions													
			Apnea					Baseline					Head Down			
			μ_1	μ_2	σ_1	σ_2		μ_1	μ_2	σ_1	σ_2		μ_1	μ_2	σ_1	σ_2
Subjects	1	TOI	73	69	12.3	6.6		71	69	10.9	5.2		72	71	11.6	4.7
		nTHI	71	68	13.2	5.3		70	69	12.0	4.2		81	71	10.5	4.4
	2	TOI	65	69	10.8	13.6		67	67	11.1	13.7		NA			
		nTHI	62	62	8.1	11.1		66	66	10.2	16.3					
	3	TOI	79	78	9.8	11.5		68	69	14.8	13.6		60	64	6.7	7.3
		nTHI	70	74	9.9	14.6		70	68	15.4	12.3		64	67	14.3	14.3
	4	TOI	76	202	17.0	20.7		84	79	15.0	15.0		78	93	13.8	9.9
		nTHI	74	201	14.0	26.3		84	77	15.5	13.2		72	93	8.8	11.1
	5	TOI	73	79	10.7	8.0		85	84	14.1	15.2		81	82	8.0	8.5
		nTHI	79	77	10.3	6.1		85	84	12.3	9.5		83	81	8.7	6.4
	6	TOI	85	78	9.4	9.3		68	66	10.5	5.5		72	66	10.1	3.3
		nTHI	80	78	10.1	8.3		66	66	5.9	6.5		65	67	8.7	3.7

Table D.1.4

HR (bpm) - HS (2/2)			Conditions								
			Hyperventilation					Valsalva Maneuver			
			μ_1	μ_2	σ_1	σ_2		μ_1	μ_2	σ_1	σ_2
Subjects	1	TOI	90	88	6.8	6.9		90	81	10.8	6.7
		nTHI	90	87	4.2	5.3		82	80	11.6	3.6
	2	TOI	86	85	10.5	12.3		35	37	3.5	2.6
		nTHI	86	80	9.7	10.7		83	31	139.9	4.6
	3	TOI	90	97	11.3	23.6		101	36	14.9	5.0
		nTHI	95	91	10.6	9.4		98	38	15.0	6.6
	4	TOI	81	39	11.2	5.8		80	53	10.2	11.6
		nTHI	79	35	9.3	13.8		81	56	8.1	7.7
	5	TOI	115	113	16.3	19.4		93	101	20.5	13.0
		nTHI	116	106	9.0	8.0		85	98	6.8	18.1
	6	TOI	113	113	11.5	7.8		78	83	13.3	9.9
		nTHI	109	113	11.8	7.0		78	83	8.8	13.5

D.2   HBI and HR Tables - PT

Tables D.2.1 and D.2.2 report the HBI and HR μ and σ from the PT under every testing condition. Again, the values marked in red are apparently anomalous values which are maybe due to the particular morphology of the original SRS signals from that channel.

For the reasons discussed above, the peculiar features of PT2 and PT5 have led to odd HBI and HR mean values.

Specifically, channel 1 of PT2 under Post-CV condition may have been affected by the band loosening as discussed in section 5.1, possibly causing an uncommon reduction of the O2Hb main frequency value which led to a malfunctioning SRS filtering algorithm (based on a too low central frequency), eventually determining the detection of too distant peaks, hence calculating too large HBI and too low HR values (9 bpm).

In the case of PT5, the long RR intervals related to this patient's fibrillation condition may be responsible for the odd increase of HR after the CV, although the NSR had been restored and the patient's HR should have been higher during the AF and then reduced after the CV. Furthermore, the long RR intervals may be responsible for the similar results obtained on the HBI and HR extracted from both the NIRS and ECG signals.

Table D.2.1

HBI (s) - PT			Conditions								
			Pre-CV					Post-CV			
			μ_1	μ_2	σ_1	σ_2		μ_1	μ_2	σ_1	σ_2
	1	TOI	0.76	0.77	0.09	0.09		1.02	1.01	0.15	0.19
		nTHI	0.77	0.77	0.09	0.09		1.05	1.03	0.07	0.14
			μ_1	μ_2	σ_1	σ_2		μ_1	μ_2	σ_1	σ_2
	2	TOI	0.89	0.88	0.10	0.11		6.41	1.12	0.05	0.22
		nTHI	0.89	0.88	0.10	0.10		6.41	1.12	0.06	0.23
			μ_1	μ_2	σ_1	σ_2		μ_1	μ_2	σ_1	σ_2
	3	TOI	0.72	0.72	0.12	0.11		0.92	0.92	0.15	0.14
		nTHI	0.73	0.72	0.11	0.11		0.94	0.92	0.12	0.14
			μ		σ			μ		σ	
		ECG	0.73		0.12			0.97		0.07	
Subjects			μ_1	μ_2	σ_1	σ_2		μ_1	μ_2	σ_1	σ_2
	4	TOI	0.60	0.60	0.08	0.08		0.92	0.91	0.17	0.17
		nTHI	0.60	0.60	0.08	0.08		0.94	0.94	0.15	0.16
			μ		σ			μ		σ	
		ECG	0.52		0.09			0.97		0.05	
			μ_1	μ_2	σ_1	σ_2		μ_1	μ_2	σ_1	σ_2
	5	TOI	1.05	1.05	0.15	0.20		0.90	0.89	0.13	0.15
		nTHI	1.05	1.06	0.13	0.21		0.92	0.90	0.08	0.14
			μ		σ			μ		σ	
		ECG	0.99		0.14			0.93		0.07	
			μ_1	μ_2	σ_1	σ_2		μ_1	μ_2	σ_1	σ_2
	6	TOI	0.72	0.71	0.10	0.11		1.23	1.23	0.13	0.15
		nTHI	0.73	0.73	0.08	0.08		1.23	1.23	0.15	0.15
			μ		σ			μ		σ	
		ECG	0.69		0.11			1.17		0.25	

Table D.2.2

HR (bpm) - PT			Conditions							
			Pre-CV				Post-CV			
			μ_1	μ_2	σ_1	σ_2	μ_1	μ_2	σ_1	σ_2
Subjects	1	TOI	80	80	11.6	11.3	60	62	10.2	12.2
		nTHI	80	79	10.7	9.7	58	59	4.2	13.0
			μ_1	μ_2	σ_1	σ_2	μ_1	μ_2	σ_1	σ_2
	2	TOI	68	69	8.5	9.1	9	56	0.1	11.6
		nTHI	68	69	8.8	8.6	9	56	0.1	11.6
			μ_1	μ_2	σ_1	σ_2	μ_1	μ_2	σ_1	σ_2
	3	TOI	85	86	16.0	14.9	67	67	12.4	11.8
		nTHI	84	86	12.9	13.9	65	67	9.3	11.5
			μ		σ		μ		σ	
		ECG	85		15.2		62		8.4	
			μ_1	μ_2	σ_1	σ_2	μ_1	μ_2	σ_1	σ_2
	4	TOI	103	103	15.6	16.9	68	68	13.6	13.5
		nTHI	102	103	16.2	16.0	66	65	11.8	11.9
			μ		σ		μ		σ	
		ECG	117		16.3		62		5.0	
			μ_1	μ_2	σ_1	σ_2	μ_1	μ_2	σ_1	σ_2
	5	TOI	59	59	9.5	11.8	69	69	11.7	12.4
		nTHI	58	59	7.1	13.1	66	69	6.6	11.3
			μ		σ		μ		σ	
		ECG	61		7.7		65		4.8	
			μ_1	μ_2	σ_1	σ_2	μ_1	μ_2	σ_1	σ_2
	6	TOI	85	87	14.6	16.5	50	50	6.5	7.7
		nTHI	84	84	9.7	10.8	50	49	8.4	7.0
			μ		σ		μ		σ	
		ECG	89		13.3		55		21.8	

Appendix E

Narrow Filtering Results

In this appendix the complete set of results from the SRS signals filtering from *every* tested subject (HS and PT) under *every* testing condition is reported.

E.1   SRS Signals Filtering - HS

Figures E.1.1 - E.1.29 show the original and filtered version of the TOI signals of the HS under every testing condition.
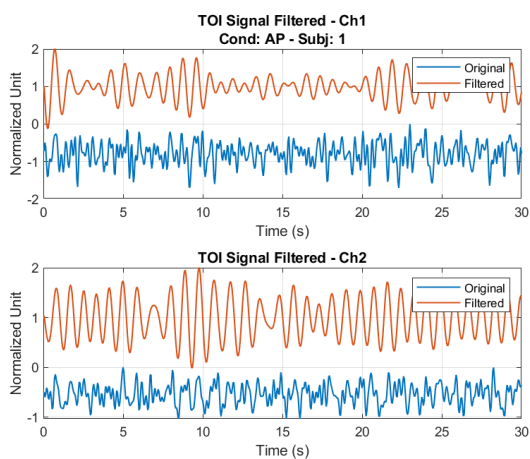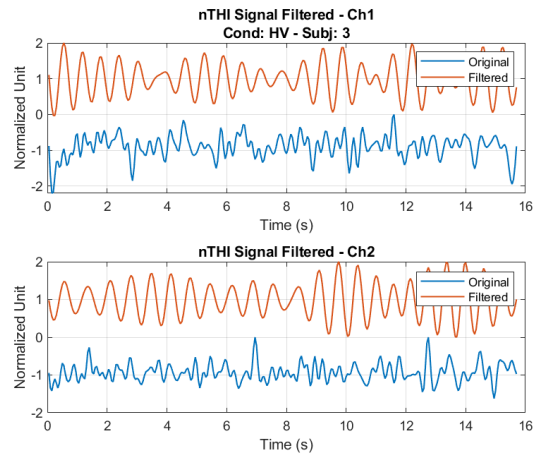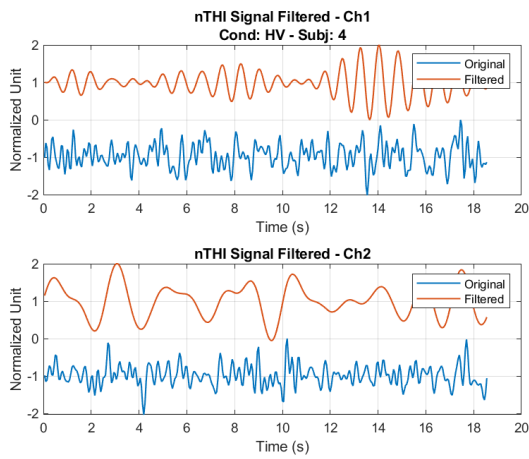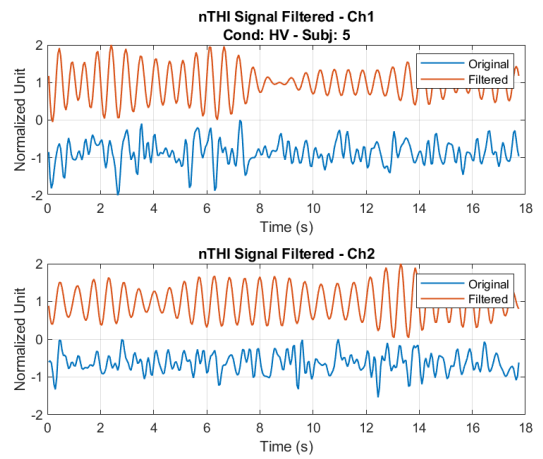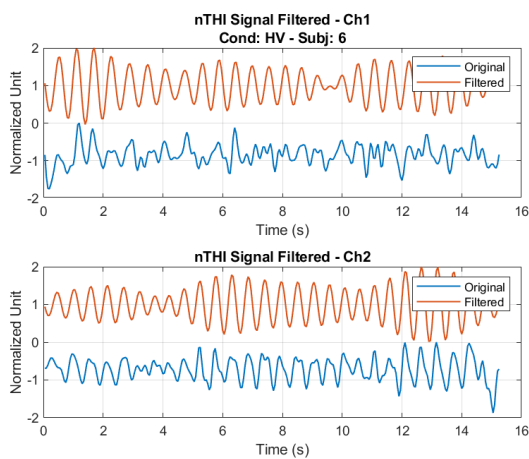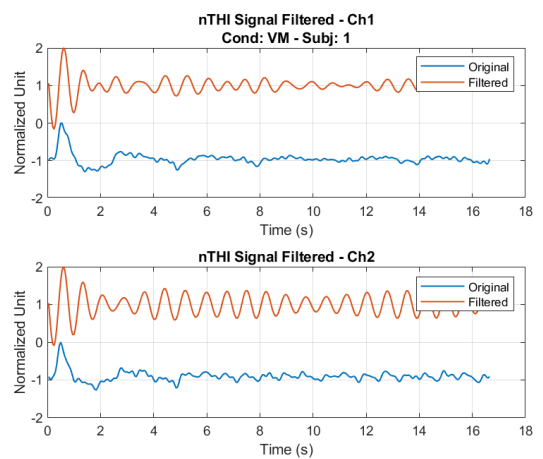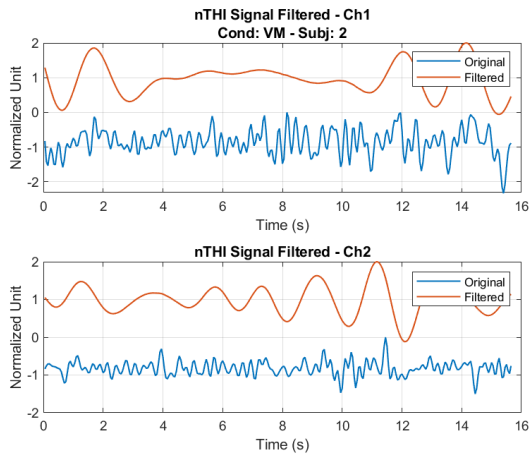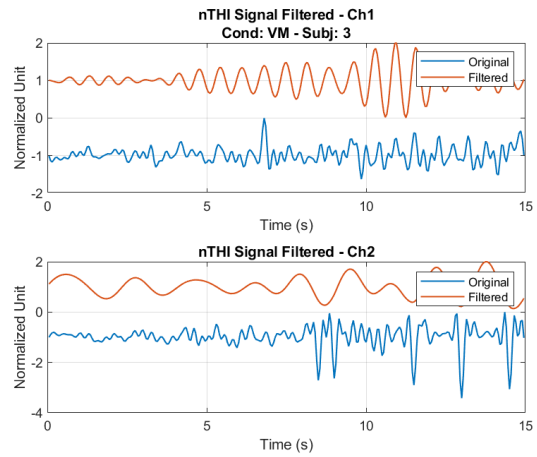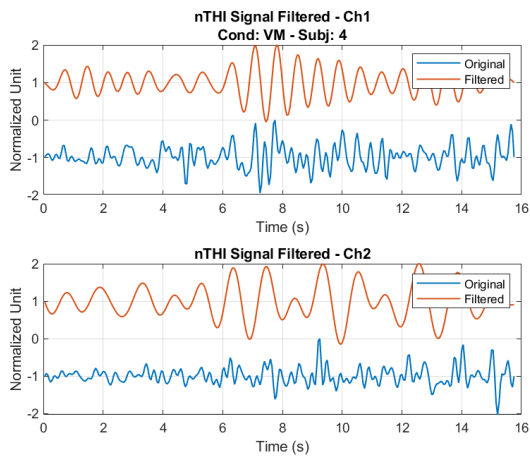

Figure E.1.1
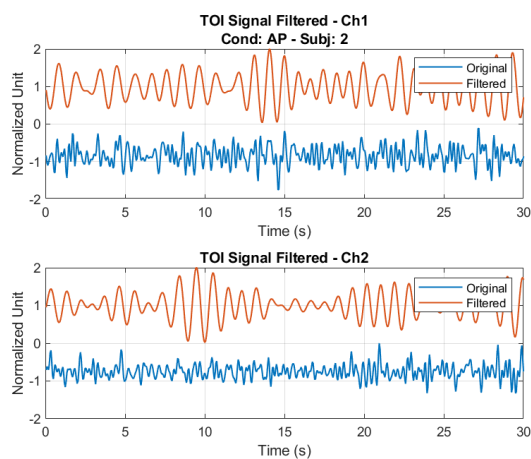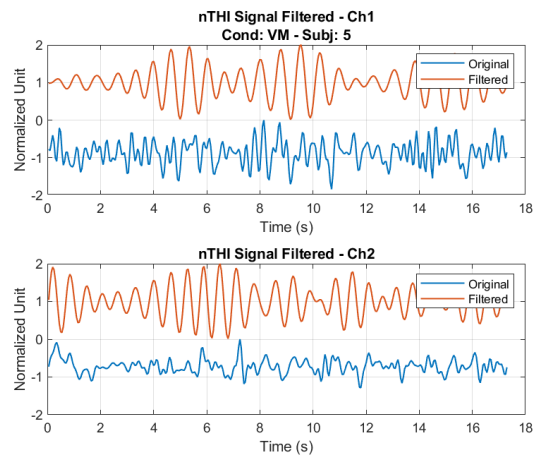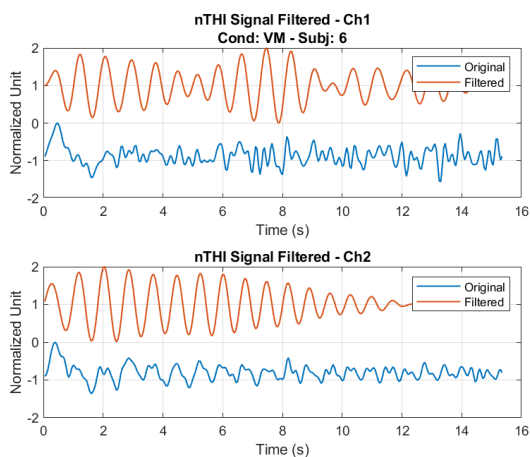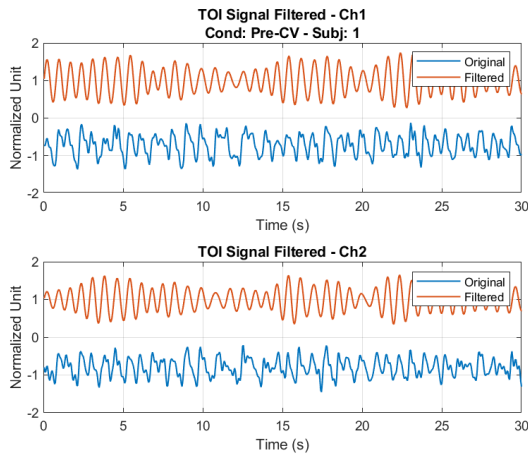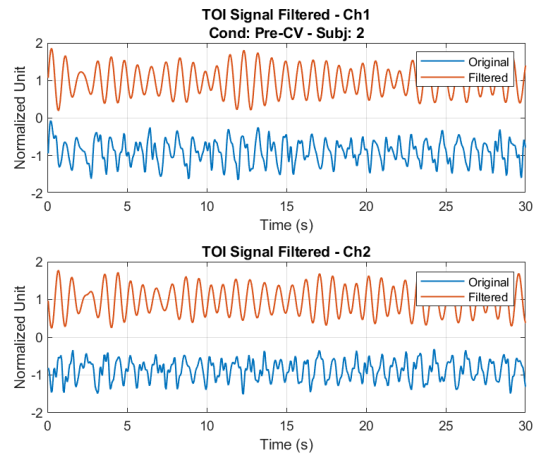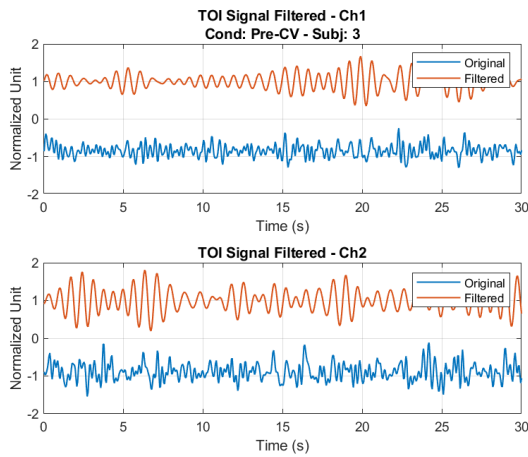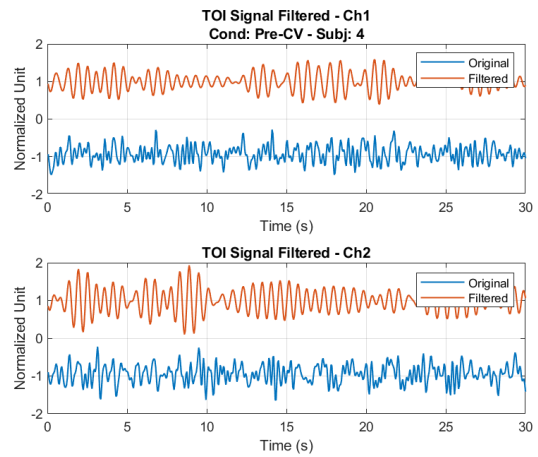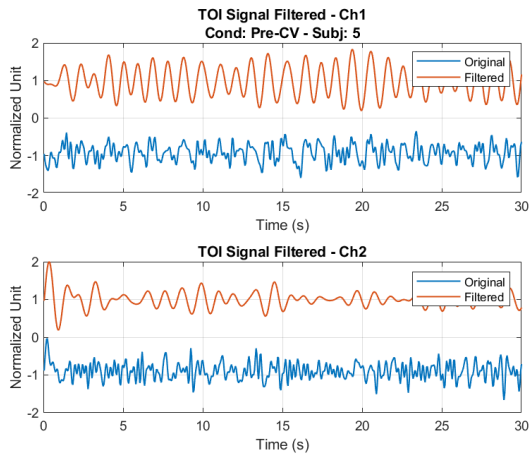
Figure E.1.2
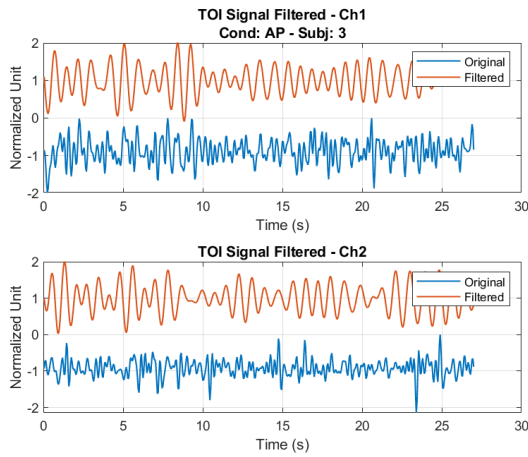
Figure E.1.3
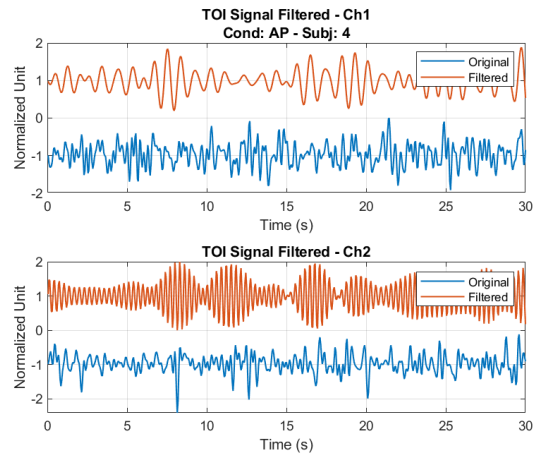
Figure E.1.4
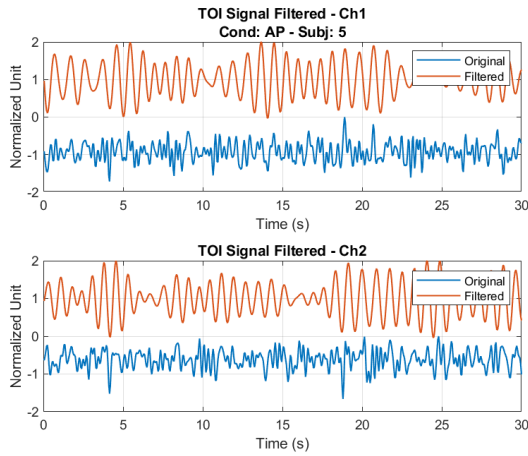
Figure E.1.5
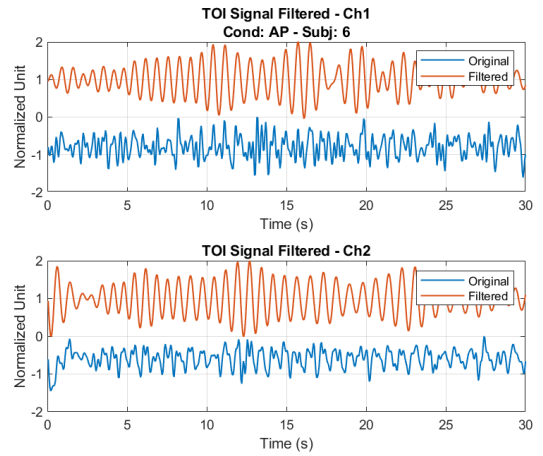
Figure E.1.6
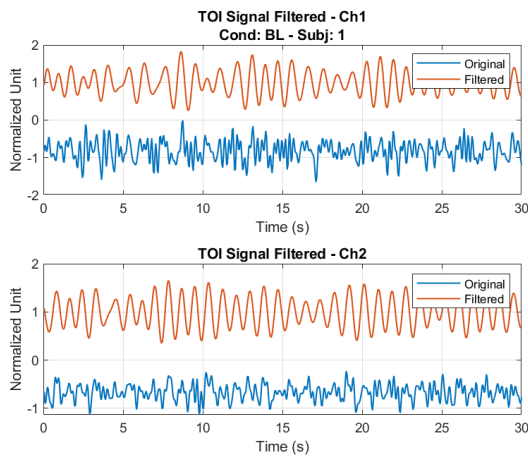
Figure E.1.7
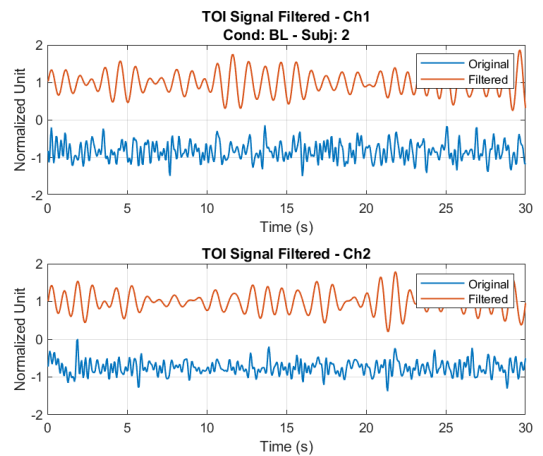
Figure E.1.8
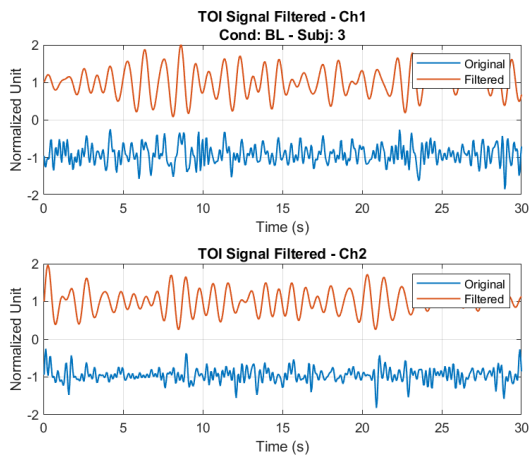
Figure E.1.9
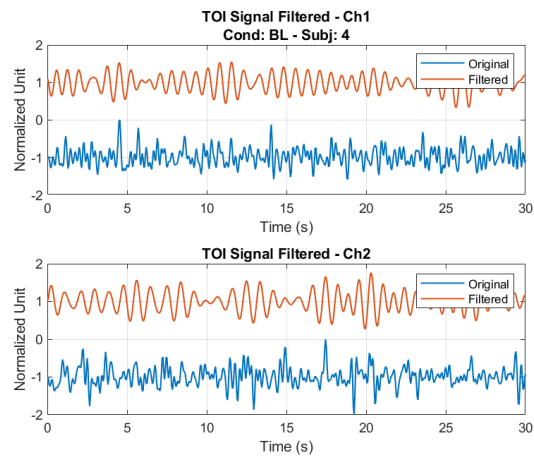
Figure E.1.10
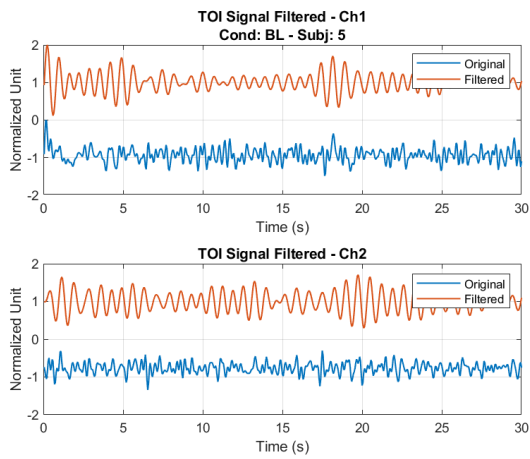
Figure E.1.11
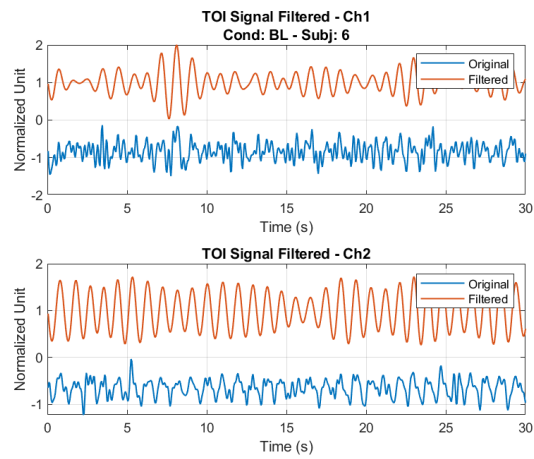
Figure E.1.12
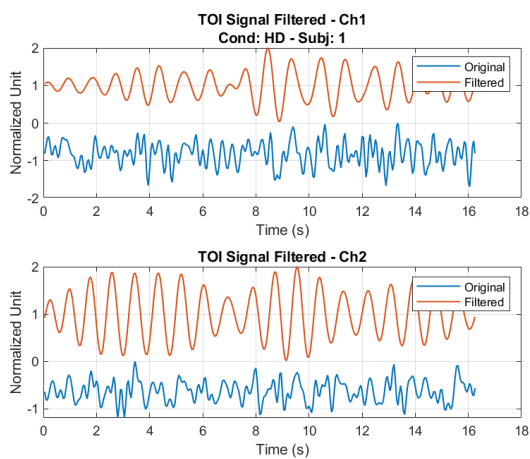
Figure E.1.13
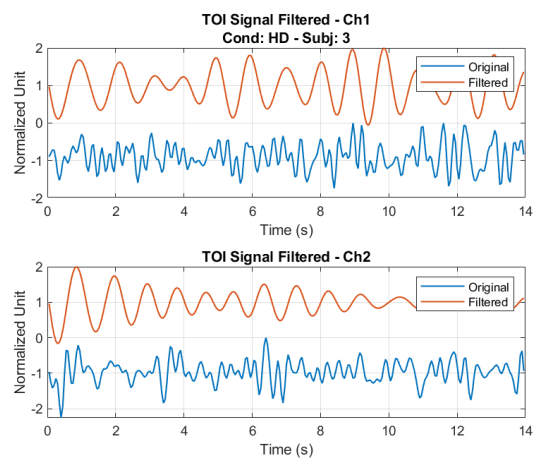
Figure E.1.14
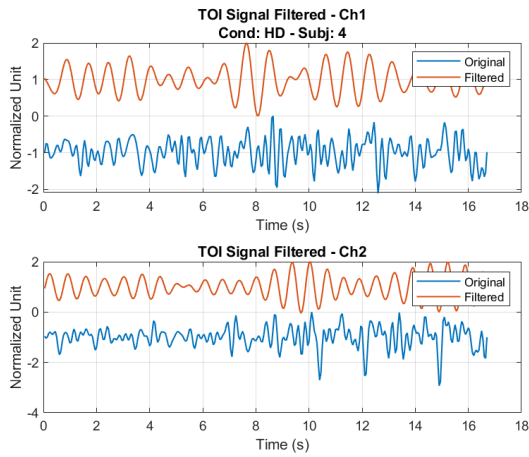
Figure E.1.15
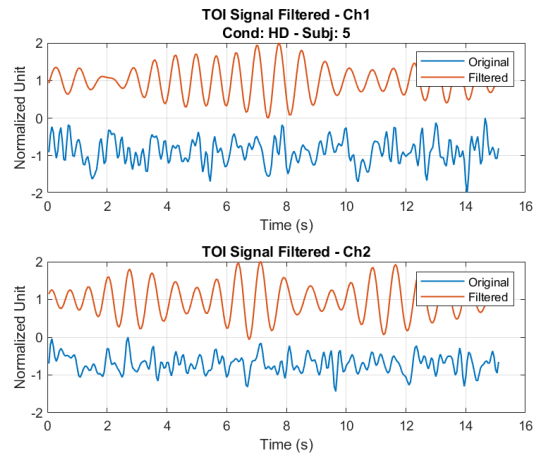
Figure E.1.16
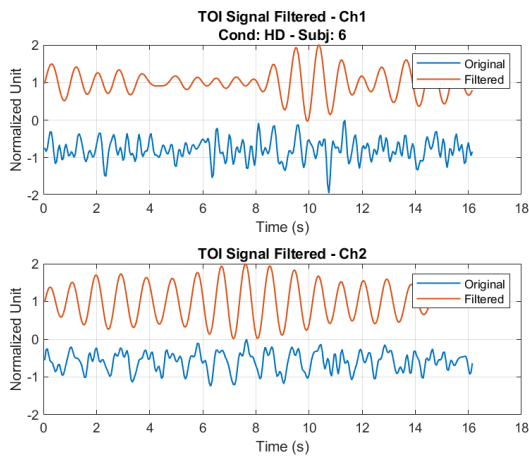
Figure E.1.17
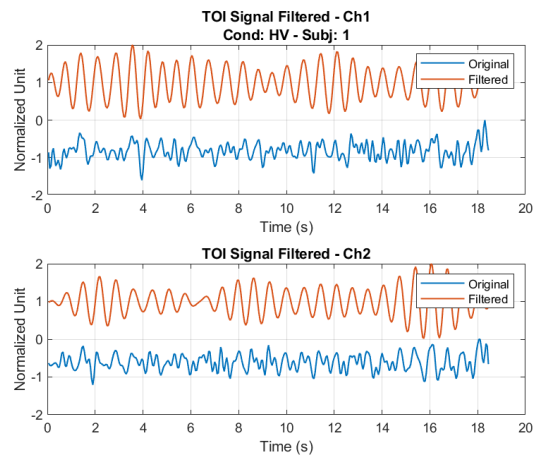
Figure E.1.18
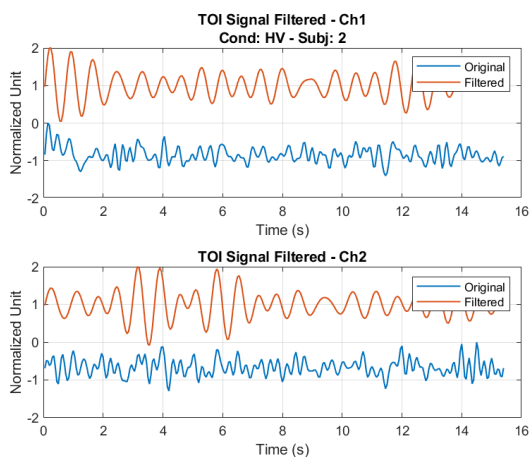
Figure E.1.19
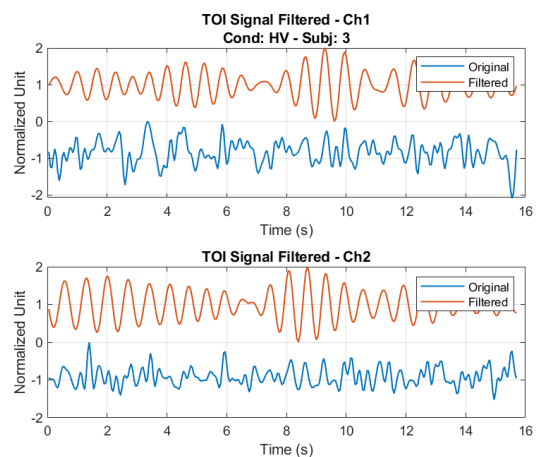
Figure E.1.20
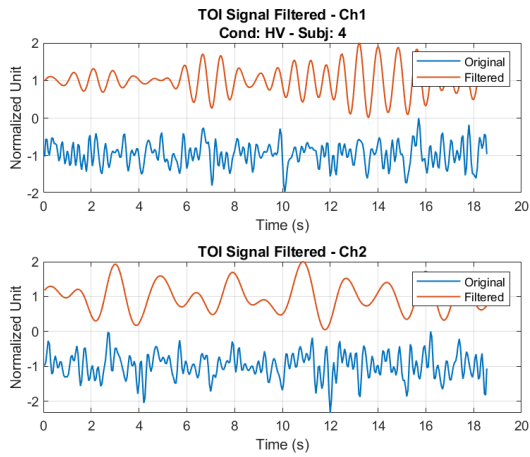
Figure E.1.21
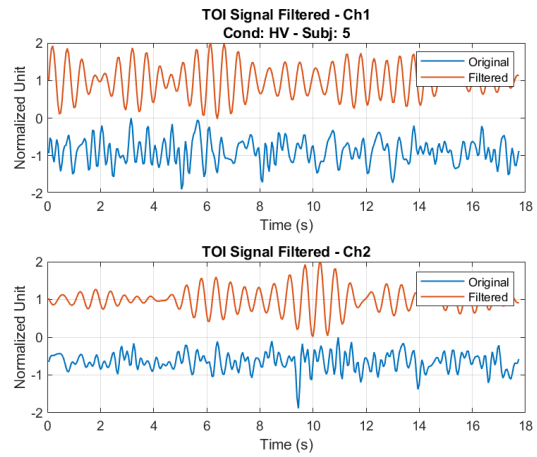
Figure E.1.22
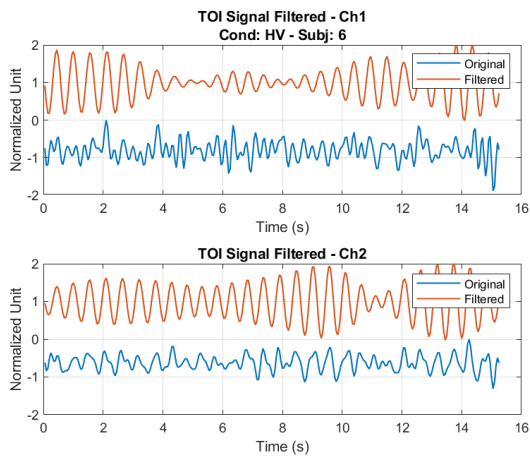
Figure E.1.23
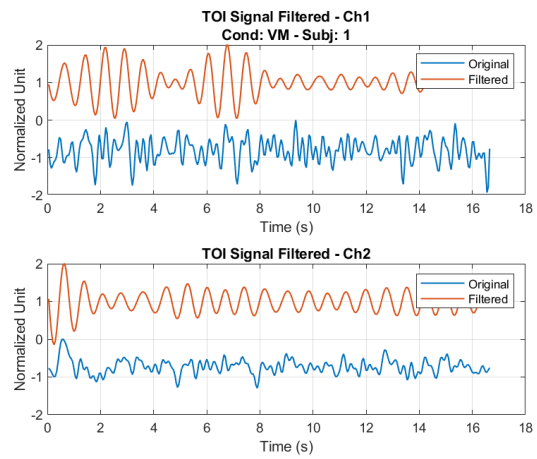
Figure E.1.24
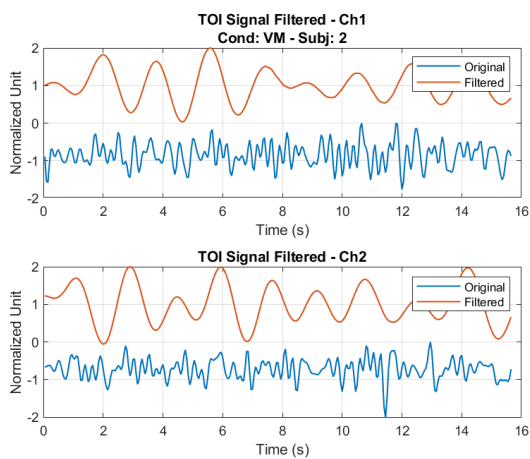
Figure E.1.25
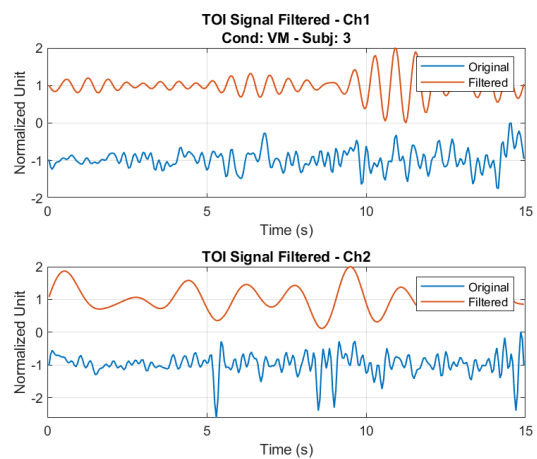
Figure E.1.26
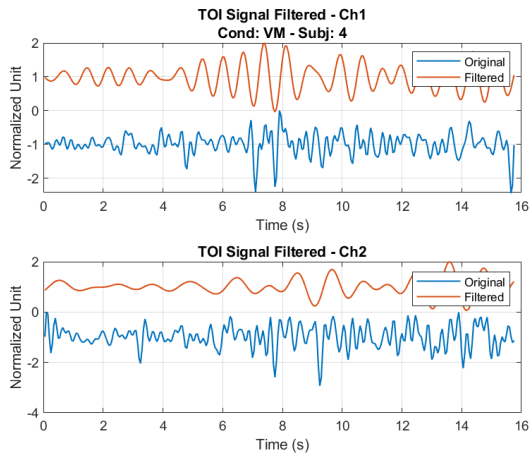
Figure E.1.27
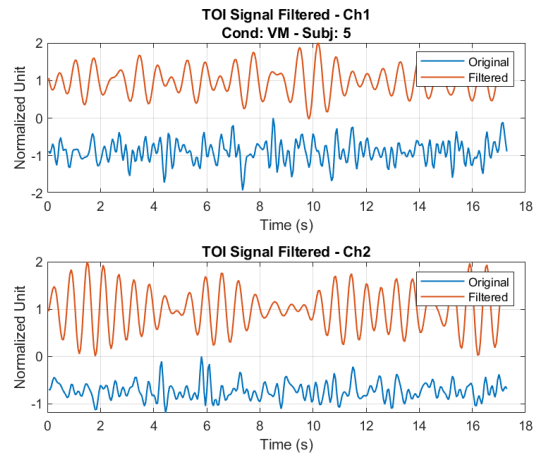
Figure E.1.28
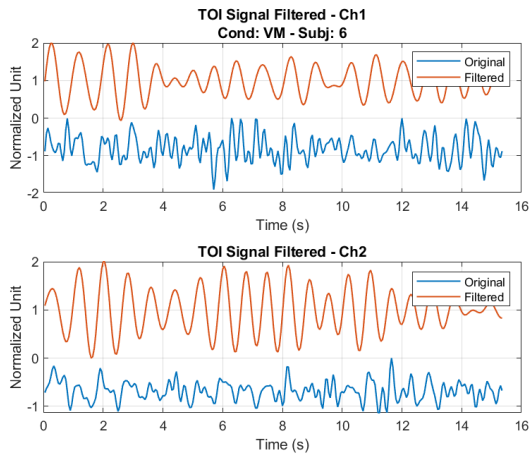
Figure E.1.29

Figures E.1.30 - E.1.58 show the original and filtered version of the nTHI signals of the HS under every testing condition.
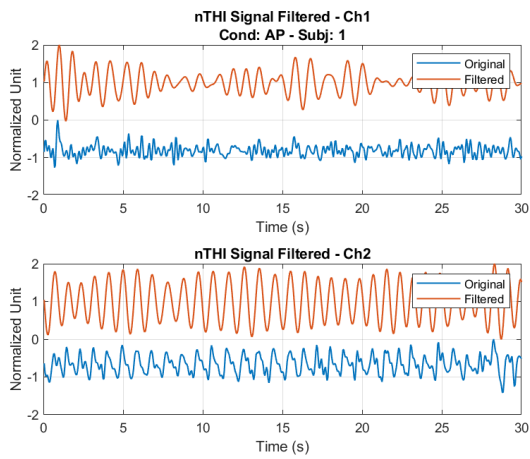
Figure E.1.30
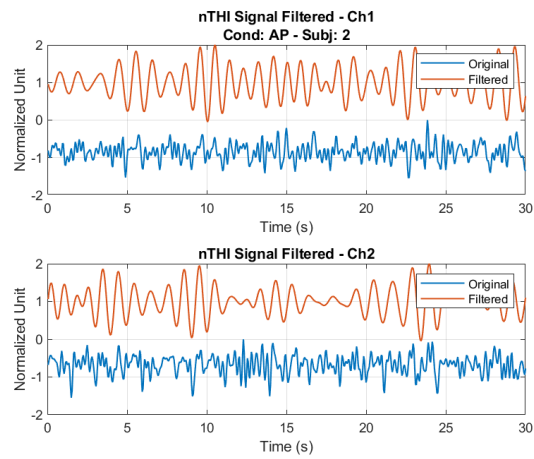
Figure E.1.31
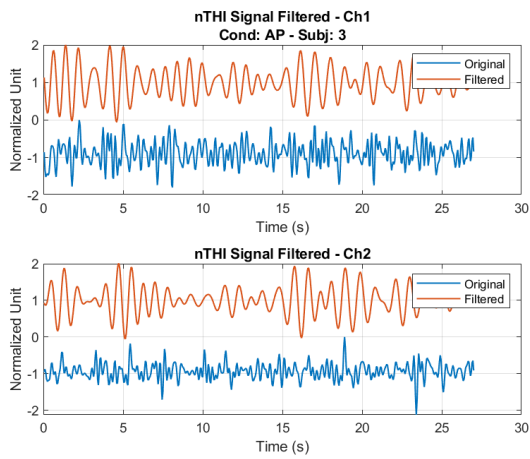
Figure E.1.32
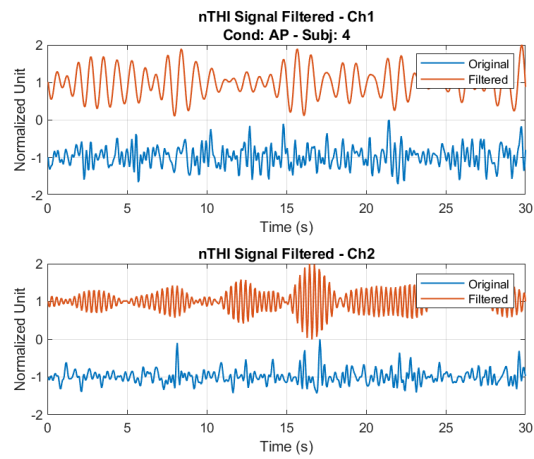
Figure E.1.33
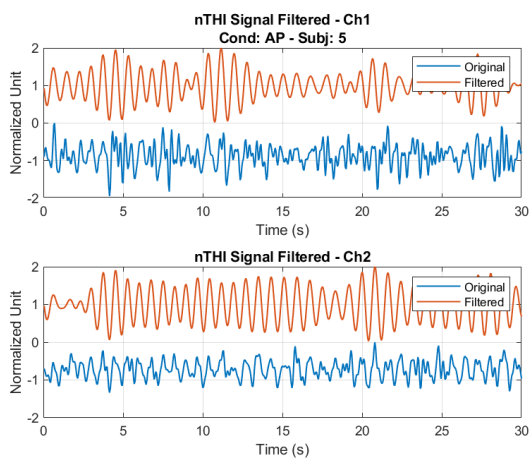
Figure E.1.34
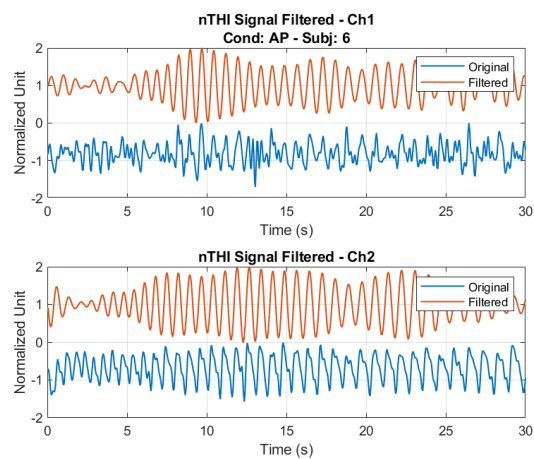

Figure E.1.35
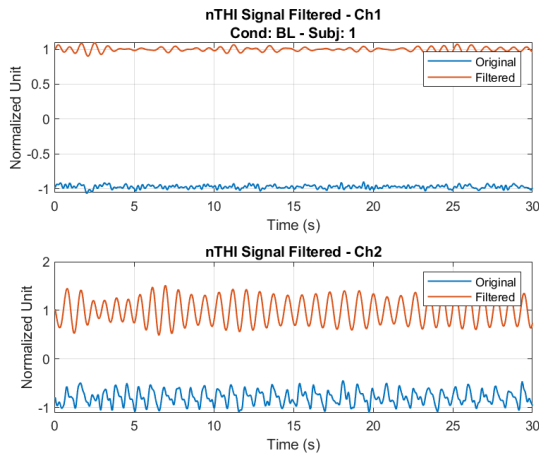
Figure E.1.36
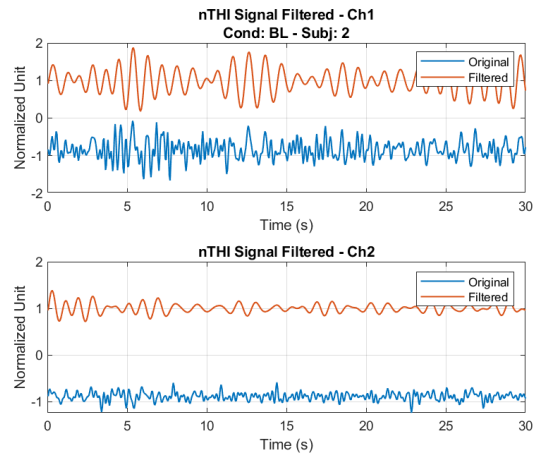
Figure E.1.37
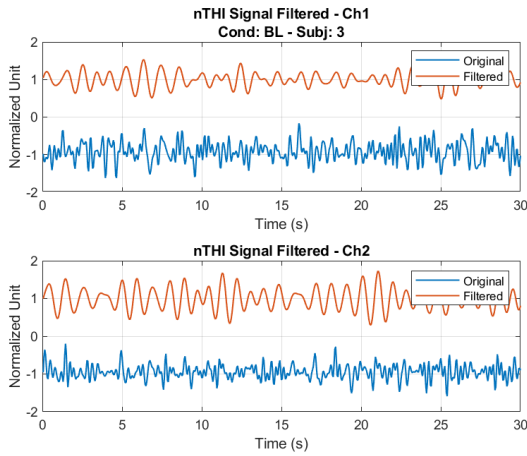
Figure E.1.38
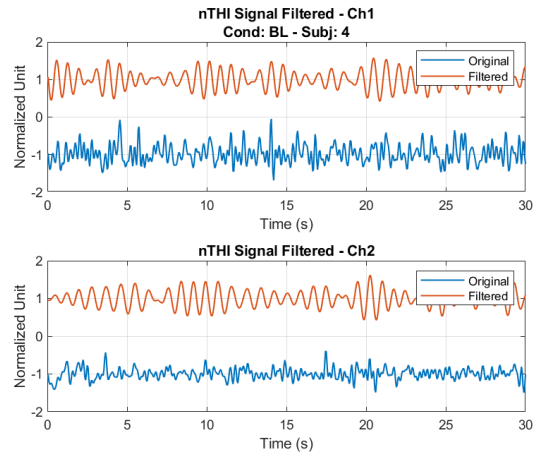
Figure E.1.39
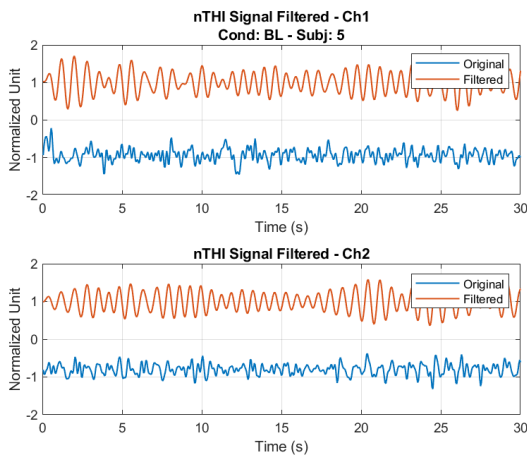
Figure E.1.40
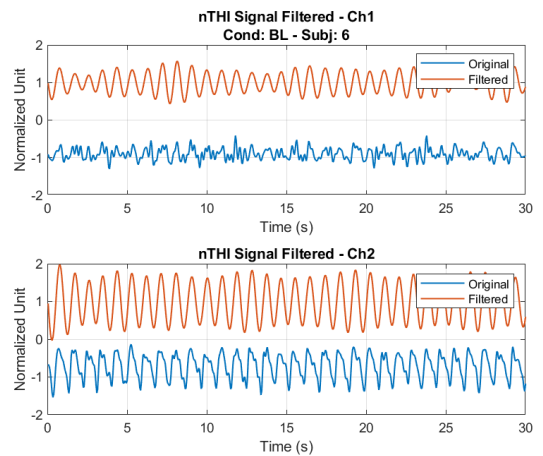
Figure E.1.41
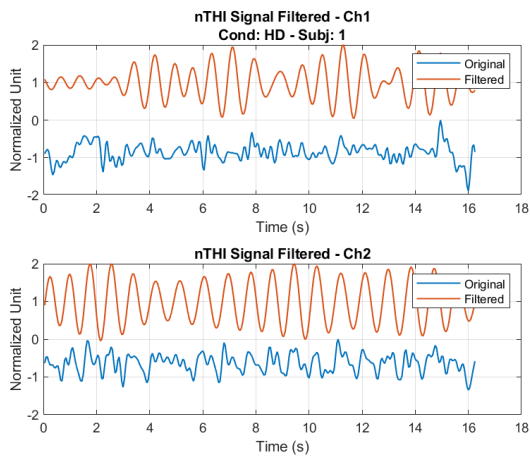
Figure E.1.42
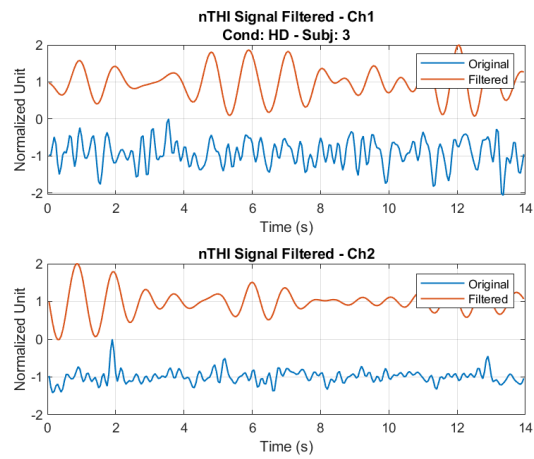
Figure E.1.43
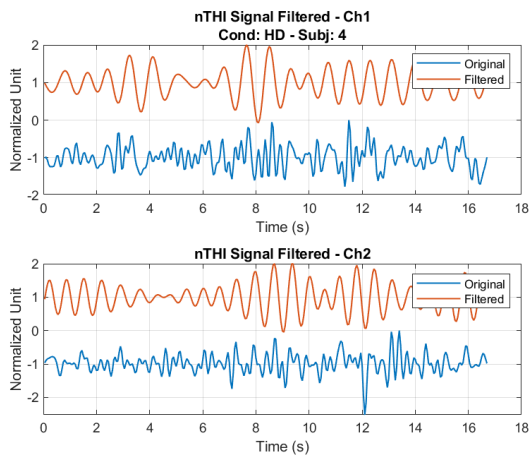
Figure E.1.44
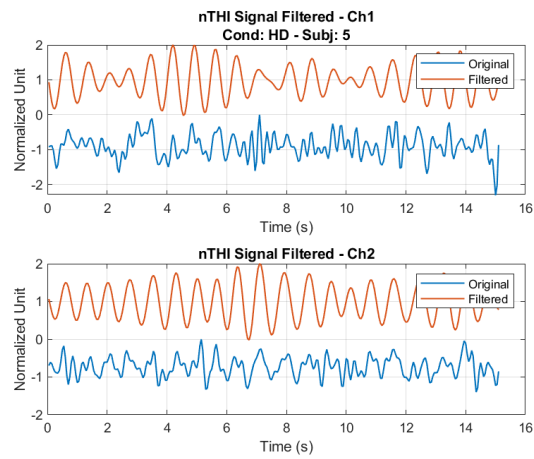
Figure E.1.45
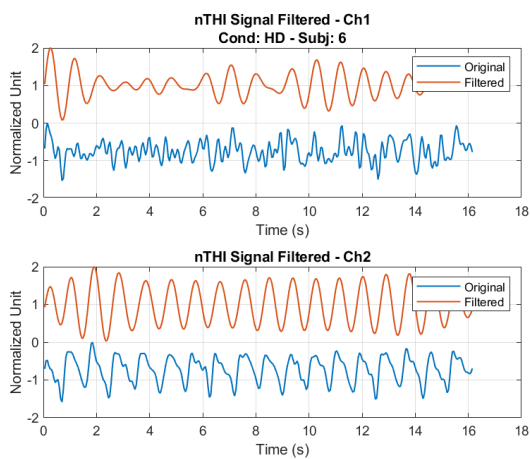
Figure E.1.46

Figure E.1.47

115
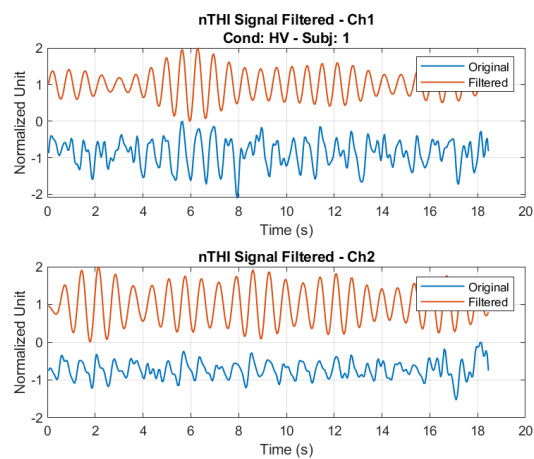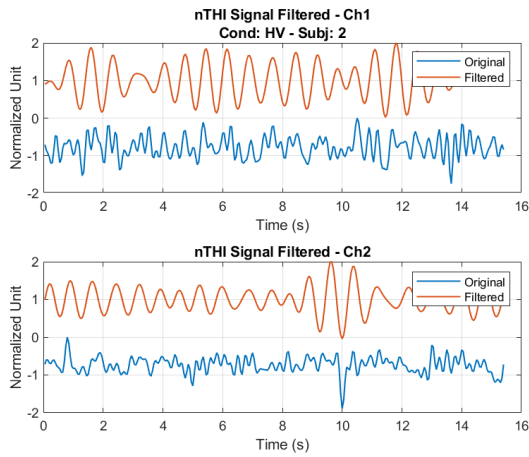
Figure E.1.48

Figure E.1.49

Figure E.1.50

Figure E.1.51

Figure E.1.52

Figure E.1.53

Figure E.1.54

Figure E.1.55

Figure E.1.56

Figure E.1.57

Figure E.1.58

117

E.2 SRS Signals Filtering - PT

Figures E.2.1 - E.2.12 show the original and filtered version of the TOI signals of the PT under every testing condition.

Figure E.2.1

Figure E.2.2

Figure E.2.3

Figure E.2.4

Figure E.2.5
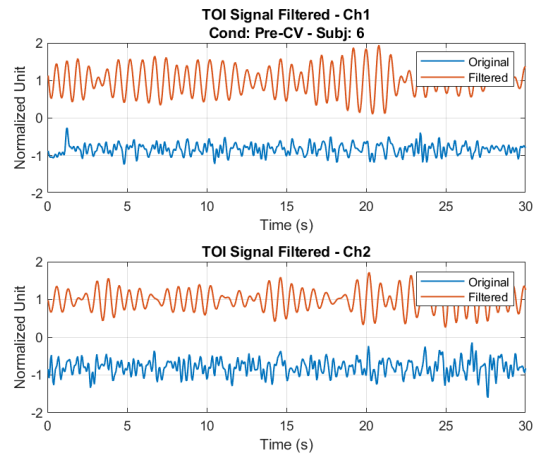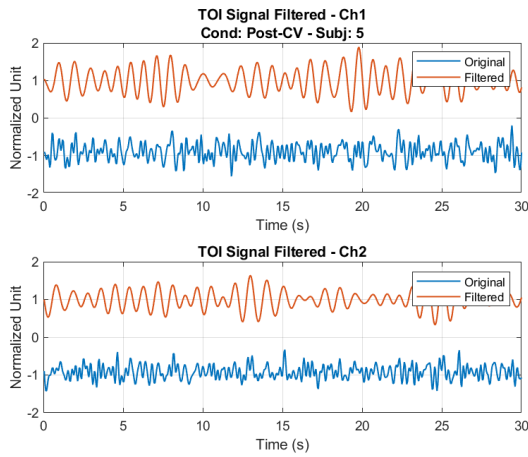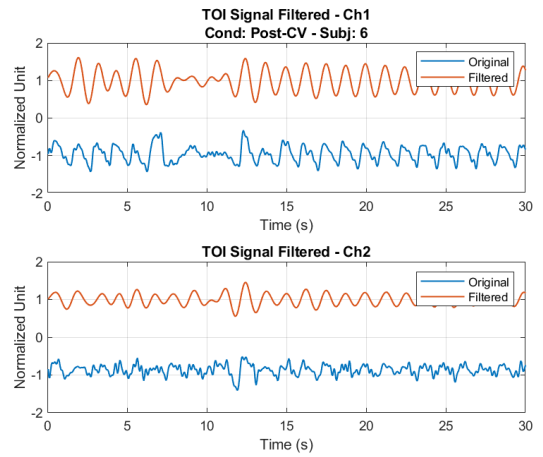

Figure E.2.6
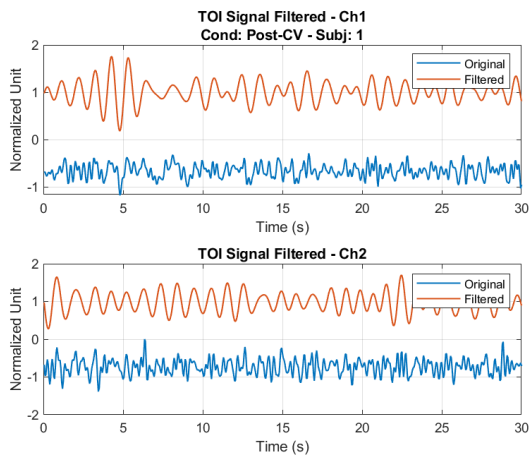
Figure E.2.7
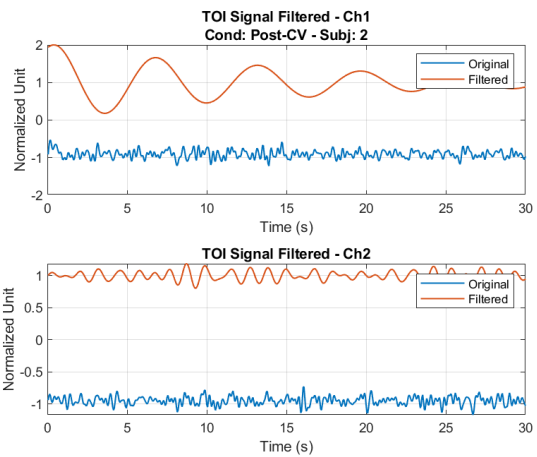
Figure E.2.8
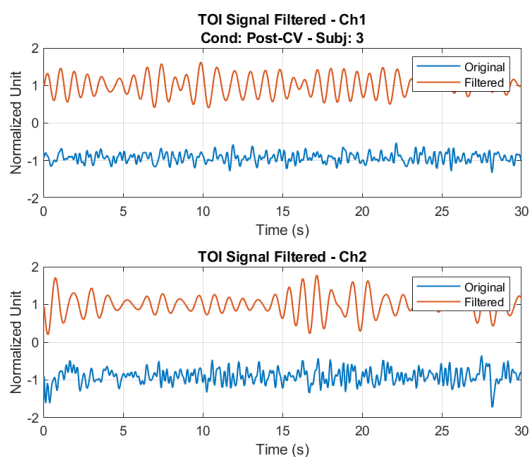
Figure E.2.9

Figure E.2.10

119
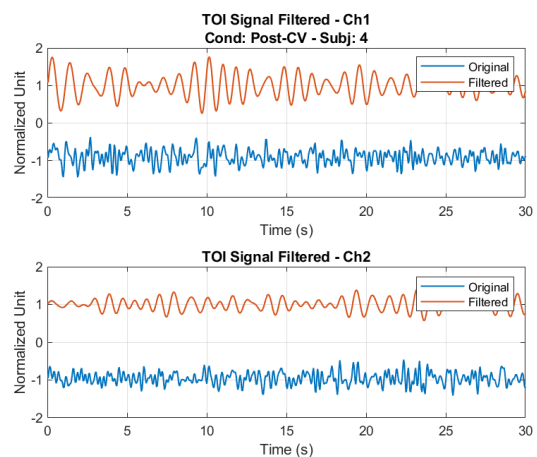
Figure E.2.11

Figure E.2.12

Figures E.2.13 - E.2.24 show the original and filtered version of the nTHI signals of the PT under every testing condition.
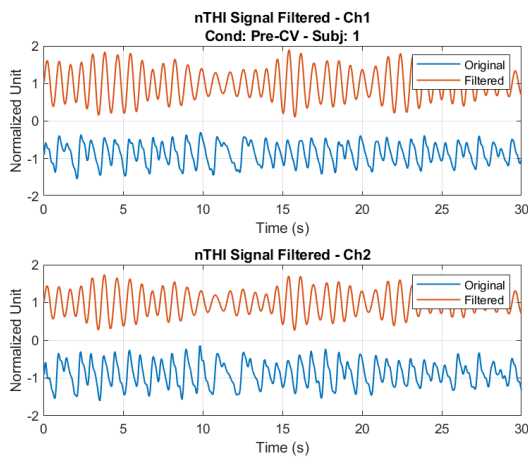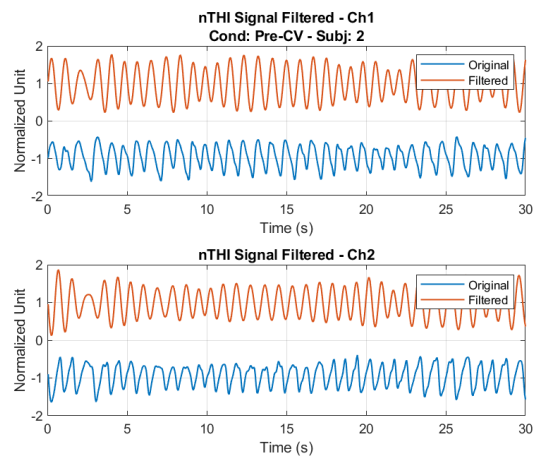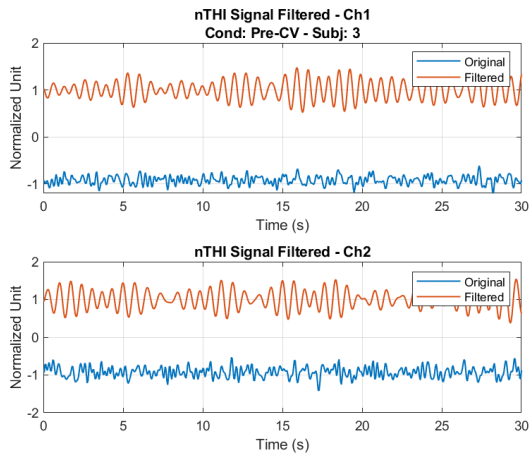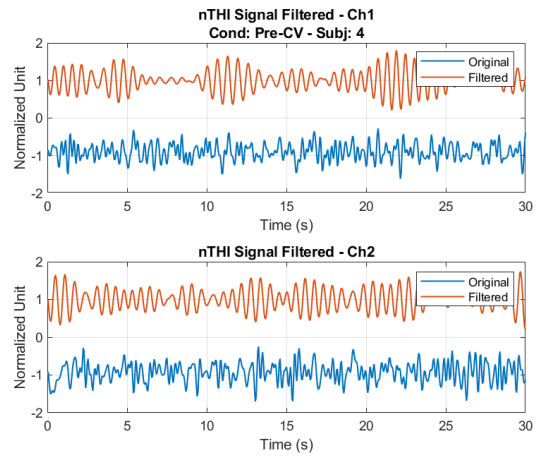

Figure E.2.13

Figure E.2.14

Figure E.2.15

Figure E.2.16
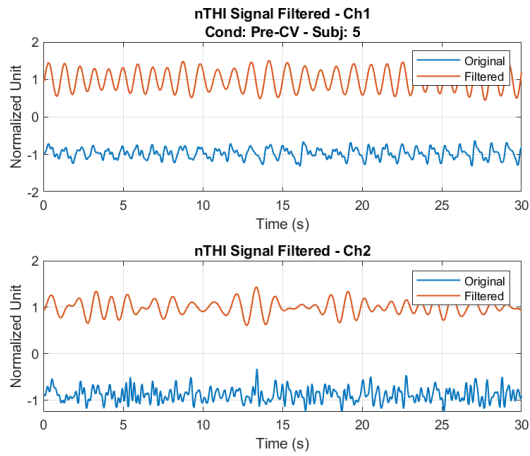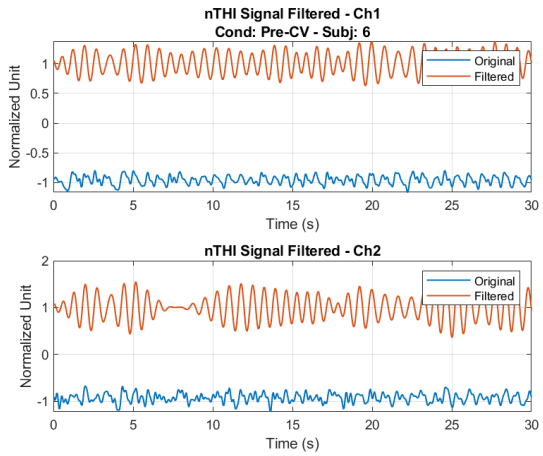

Figure E.2.17

Figure E.2.18

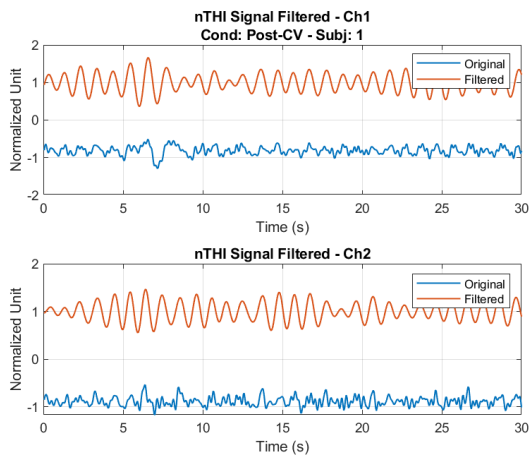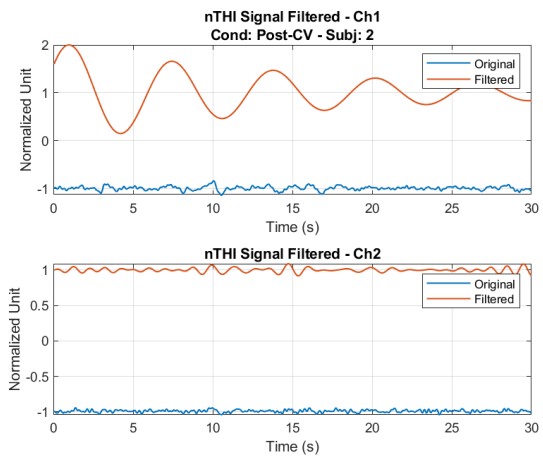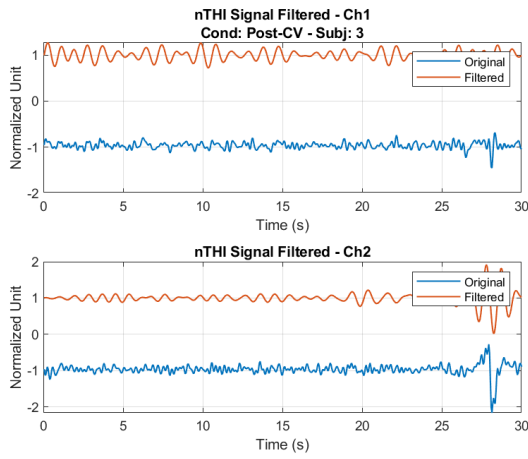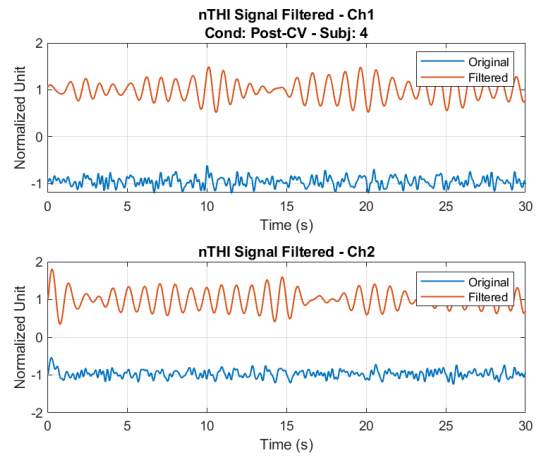
Figure E.2.19
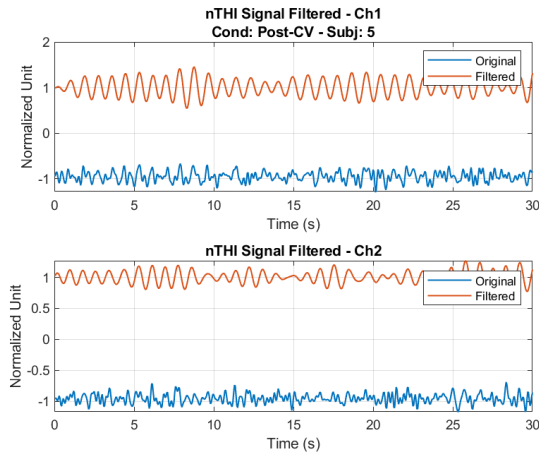

Figure E.2.20
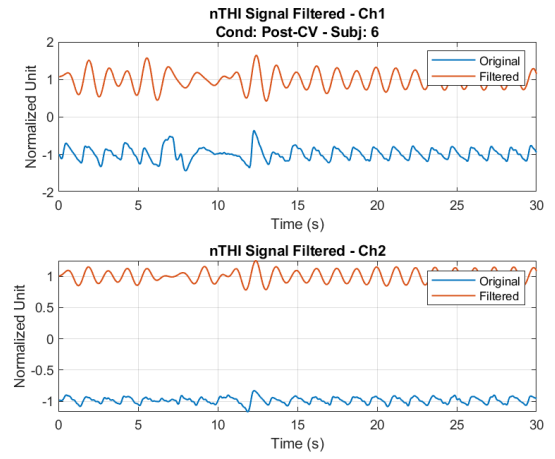
Figure E.2.21

Figure E.2.22

Figure E.2.23

Figure E.2.24

Bibliography

[1] January C. T., Wann L. S., Alpert J. S., Calkins H., Cigarroa J. E., Cleveland J. C., Conti J. B., Ellinor P. T., Ezekowitz M. D., Field M. E., Murray K. T., Sacco R. L., Stevenson W. G., Tchou P. J., Tracy C. M., and Yancy C. W. 2014 aha/acc/hrs guideline for the management of patients with atrial fibrillation: A report of the american college of cardiology/american heart association task force on practice guidelines and the heart rhythm society. *Journal of the American College of Cardiology*, 64(21):e1 – e76, 2014.

[2] Kalantarian S., Stern T. A., Mansour M, and Ruskin J. N. Cognitive impairment associated with atrial fibrillation: A meta-analysis. *Annals of Internal Medicine*, 158(501):338–346, 2013.

[3] Bunch T. J., Weiss J. P., Crandall B. G., May H. T., Bair T. L., Osborn J. S., Anderson J. L., Muhlestein J. B., Horne B. D., Lappe D. L., and Day J. D. Atrial fibrillation is independently associated with senile, vascular, and Alzheimer's dementia. *Heart Rhythm Society*, 7(4):433–437, 2010.

[4] Stefansdottir H., Arnar D. O., Aspelund T., Sigurdsson S., Jonsdottir M. K., Hjaltason H., Launer L. J., and Gudnason V. Atrial fibrillation is associated with reduced brain volume and cognitive function independent of cerebral infarcts. *Stroke*, 44(4):1020–1025, 2013.

[5] Scarsoglio S., Cazzato F., and Ridolfi L. From time-series to complex networks: Application to the cerebrovascular flow patterns in atrial fibrillation. *Chaos*, 27(9), 2017.

[6] Scarsoglio S., Saglietto A., Anselmino M., Gaita F., and Ridolfi L. Alteration of cerebrovascular haemodynamic patterns due to atrial fibrillation: an in silico investigation. *Journal of the Royal Society Interface*, 14, 2017.

[7] Anselmino M., Scarsoglio S., Saglietto A., Gaita F., and Ridolfi L. Transient cerebral hypoperfusion and hypertensive events during atrial fibrillation: a plausible mechanism for cognitive impairment. *Scientific Reports*, 6, 2016.

[8] Wutzler A., Nee J., Boldt L. H., Kuhnle Y., Graser S., Schroder T., Haverkamp W., and Storm C. Improvement of cerebral oxygen saturation after successful electrical cardioversion of atrial fibrillation. *Europace*, 16(2):189–194, 2014.

[9] Wutzler A., Otto N., Graser S., Boldt L. H., Huemer M., Parwani A., Haverkamp W., and Storm C. Acute decrease of cerebral oxygen saturation during rapid ventricular and supraventricular rhythm: A pilot study. *PACE*, 37(9):1159–1165, 2014.

[10] Hershenson J. A., Ro P. S., Miao Y., Tobias J. D., Olshove V., and Naguib A. N. Changes in hemodynamic parameters and cerebral saturation during supraventricular tachycardia. *Pediatric Cardiology*, 33(2):286–289, 2012.

[11] Davies T. The history of near infrared spectroscopic analysis: Past, present and future "from sleeping technique to the morning star of spectroscopy". *Analusis*, 26(4):17–19, 1998.

[12] Wahr J. A., Tremper K. K., Samra S., and Delpy D. T. Near-infrared spectroscopy: Theory and applications. *Journal of Cardiothoracic and Vascular Anaesthesia*, 10(3):406–418, 1996.

[13] Owen-Reece H., Smith M., Elwell C. E., and Goldstone J. C. Near infrared spectroscopy. *British Journal of Anaesthesia*, 82(3):418–426, 1999.

[14] Davies D. J., Su Z., Clancy M. T., Lucas S. J. E., Dehghani H., Logan A., and Belli A. Near-infrared spectroscopy in the monitoring of adult traumatic brain injury: A review. *Journal of Neurotrauma*, 32(13):933–941, 2015.

[15] Calderon-Arnulphi M., Alaraj A., and Slavin K. V. Near infrared technology in neuroscience: past, present and future. *Neurological Research*, 31(6):605–614, 2009.

[16] Cui W., Kumar C., and Chance B. Experimental study of migration depth for the photons measured at sample surface. *Proc.SPIE*, 1431:180–191, 1991.

[17] Delpy D. T., Cope M., Van der Zee P., Arridge S., Wray S., and Wray J. Estimation of optical pathlength through tissue from direct time of flight measurement. *Physics in Medicine & Biology*, 33(12):1433–1442, 1988.

[18] Scholkmann F., Kleiser S., Jaakko Metz A., Zimmermann R., Pavia J. M., Wolf U., and Wolf M. A review on continuous wave functional near-infrared spectroscopy and imaging instrumentation and methodology. *NeuroImage*, 85:6–27, 2014.

[19] Suzuki S., Takasaki S., Ozaki T., and Kobayashi Y. Tissue oxygenation monitor using nir spatially resolved spectroscopy. *Proc.SPIE*, 3597:582–592, 1999.

[20] Germon T. J., Evans P. D., Barnett N. J., Wall P., Manara A.R., and Nelson R. J. Cerebral near infrared spectroscopy: emitter-detector separation must be increased. *British Journal of Anaesthesia*, 82(6):831–837, 1999.

[21] Germon T. J., Kane N. M., Manara A. R., and Nelson R. J. Near-infrared spectroscopy in adults: effects of extracranial ischaemia and intracranial hypoxia on estimation of cerebral oxygenation. *British Journal of Anaesthesia*, 73:503–506, 1994.

[22] Germon T. J., Young A. E., Manara A. R., and Nelson R. J. Extracerebral absorption of near infrared light influences the detection of increased cerebral oxygenation monitored by near infrared spectroscopy. *Journal of Neurology, Neurosurgey and Psychiatry*, 58(4):477–479, 1995.

[23] Canova D., Roatta S., Bosone D., and Micieli G. Inconsistent detection of changes in cerebral blood volume by near infrared spectroscopy in standard clinical tests. *Journal of Applied Physiology*, 110:1646–1655, 2011.

[24] Brady K. M., Lee J. K., Kibler K. K., Smielewski P., Czosnyka M., Easley R. B., Koehler R. C., and Shaffner D. H. Continuous time-domain analysis of cerebrovascular autoregulation using near-infrared spectroscopy. *Stroke*, 38(10):2818–2825, 2007.

[25] Isasi I., Irusta U., Aramendi E., Peralta G., and Alonso E. Monitoring the heart rate in cerebral oximetry signals. *2016 Computing in Cardiology Conference (CinC)*, 43:1121–1124, 2016.

[26] J. Pan and W. J. Tompkins. A real-time qrs detection algorithm. *IEEE TRANSACTIONS ON BIOMEDICAL ENGINEERING*, BME-32(3):230–236, 1985.

[27] P. S. Hamilton. *Open Source ECG Analysis Software Documentation*. E. P. Limited, 2002.